

JAERI-M

8 6 2 1

IAEA INTOR WORKSHOP REPORT, GROUP I
—ENERGY AND PARTICLE CONFINEMENT—

January 1980

Fusion Research and Development Center

日 本 原 子 力 研 究 所
Japan Atomic Energy Research Institute

この報告書は、日本原子力研究所が JAERI-M レポートとして、不定期に刊行している研究報告書です。入手、複製などのお問い合わせは、日本原子力研究所技術情報部（茨城県那珂郡東海村）あて、お申しこしてください。

JAERI-M reports, issued irregularly, describe the results of research works carried out in JAERI. Inquiries about the availability of reports and their reproduction should be addressed to Division of Technical Information, Japan Atomic Energy Research Institute, Tokai-mura, Naka-gun, Ibaraki-ken, Japan.

IAEA INTOR Workshop Report, Group 1
- Energy and Particle Confinement -

Fusion Research and Development Center
Tokai Research Establishment, JAERI

(Received December 3, 1979)

Data base assessments of energy and particle confinement for INTOR plasma are made. They include assessment of empirical scaling laws, detailed studies on INTOR parameters by zero and one-dimensional model, heat and particle flux to the first wall and divertor plate, effects of impurities on plasma, effects of toroidal field ripple on plasma performance, confinement of alpha particles, level of synchrotron radiation, and consideration of INTOR parameters.

Key Words : INTOR Tokamak Reactor, Data Base Assessment, Energy Confinement, Particle Confinement, Scaling Laws, Impurity Effects, Synchrotron Radiation, Plasma Performance

Prepared by : Masayoshi Sugihara (Group leader), Toshio Hirayama,
Masao Kasai^{*1)}, Yoshitaka Kinoshita^{*2)}, Hiroshi Kishimoto,
Masayuki Nagami, Yukiharu Nakamura, Masami Ohnishi^{*2)},
Yasuo Shimomura, Tomonori Takizuka, Masatoshi Tanaka,
Keiji Tani, Teruhiko Tazima, Tatsuzo Tone, Takasi Tuda

*1) On leave from Mitsubishi Atomic Power Industries Inc.

*2) Institute of Atomic Energy, Kyoto University

IAEA INTOR ワークショップ検討報告書・グループ 1
— エネルギー・粒子閉じ込め —

日本原子力研究所東海研究所 核融合研究開発推進センター

(1979年12月3日受理)

INTORプラズマを検討するためのエネルギー・粒子閉じ込めに関するデータベースの評価を行った。これらの評価は、エネルギー閉じ込め経験則の検討、炉心プラズマの点モデルおよび一次元モデルによる検討、第一壁やダイバータ板への熱・粒子束、不純物の効果、トロイダル磁場リップルのプラズマ性能に及ぼす効果、アルファ粒子の閉じ込め、シンクロトロン放射損失の評価およびINTORパラメーターに関する考察等を含むものである。

作成者 杉原正芳 (グループリーダー), 平山俊雄, 笠井雅夫, 木下善貴^{*1)}, 岸本浩, 永見正幸^{*2)}, 中村幸治, 大西正視, 下村安夫, 滝塚知典, 田中正俊, 谷啓二, 田島輝彦, 東稔達三, 津田孝

*1) 三菱原子力工業, 外来研究員

*2) 京都大学, 原子エネルギー研究所

Contents

Introduction and Summary (M. Sugihara)	1
Data Base Assessment of Energy and Particle Confinement for INTOR	
1. Assessment of Empirical Scaling Law (M. Sugihara, T. Tazima) ..	3
2. Detailed Studies on INTOR Guiding Parameters by Zero- Dimensional Model (M. Sugihara, T. Tazima, M. Kasai*)	8
3. Detailed Studies on INTOR Guiding Parameters by One- Dimensional Simulation Code (M. Sugihara, M. Kasai*, T. Tone, T. Tazima)	21
4. Heat and Particle Flux to the First Wall and the Divertor Plate (M. Sugihara, T. Tone, T. Tazima)	36
5. Effects of Impurities on INTOR Plasma	40
5.1 Model of Impurity Transport (M. Nagami)	40
5.2 Impurity Effects on INTOR Plasma (T. Tazima, T. Hirayama, Y. Nakamura)	47
6. Estimation of Allowable Field Ripple	55
6.1 Effects of Field Ripple on Ion Thermal Conductivity and Loss of Reacting Tail (T. Tuda)	55
6.2 Effects of Field Ripple on NBI (H. Kishimoto)	62
6.3 Ripple Loss of Fast Ions During Slowing Down (K. Tani)	64
7. Confinement of Alpha Particles	72
7.1 Orbit Loss of 3.5 MeV Alpha Particles in an Axisymmetric Tokamak (T. Takizuka)	72
7.2 Alpha Heating Profile During Slowing Down Process (M. Ohnishi**, Y. Kinoshita**)	82
7.3 Loss of Alpha Particles by Field Ripple During Slowing Down (K. Tani)	85
8. Level of Synchrotron Radiation from INTOR Plasma (M. Tanaka)	87
Appendix Some Consideration of INTOR Parameters (Y. Shimomura)...	88

* Mitsubishi Atomic Power Industry Inc.

** Institute of Atomic Energy, Kyoto University

目 次

序 論	(杉原正芳)	1
INTOR のためのエネルギー・粒子閉じ込めのデータベース評価		
1. エネルギー閉じ込め経験則の評価	(杉原正芳, 田島輝彦)	3
2. 0次元モデルによるイントールパラメータの詳細検討 (杉原正芳, 田島輝彦, 笠井雅夫*)		8
3. 一次元シミュレーションコードによるイントールモデルの詳細検討 (杉原正芳, 笠井雅夫*, 東稔達三, 田島輝彦)		21
4. 第一壁およびダイバータ板への粒子・熱流束 (杉原正芳, 東稔達三, 田島輝彦)		36
5. イントールプラズマに対する不純物の影響		40
5.1 不純物輸送のモデル	(永見正幸)	40
5.2 イントールプラズマに対する不純物の影響 (田島輝彦, 平山俊雄, 中村幸治)		47
6. 許容磁場リップルの評価		55
6.1 イオン熱伝導およびテールの損失に対するリップルの効果 ... (津田 孝)		55
6.2 中性粒子入射に対するリップルの効果	(岸本 浩)	62
6.3 減速過程中の高速イオンのリップル損失	(谷 啓二)	64
7. アルファ粒子の閉じ込め		72
7.1 軸対称トカマク中の 3.5 MeV アルファ粒子の軌道損失	(滝塚知典)	72
7.2 減速過程中のアルファ粒子加熱分布	(大西正視**, 木下善貴**)	82
7.3 減速過程中のアルファ粒子のリップル損失	(谷 啓二)	85
8. イントールプラズマからのシンクロトロン放射	(田中正俊)	87
付録 イントールパラメータの考察	(下村安夫)	88

* 外来研究員 ; 三菱原子力

** 京都大学, 原子エネルギー研究所

INTRODUCTION & SUMMARY

INTOR guiding parameters are examined from various view points, such as point model studies, 1D simulation calculations, impurity effects and non-circularity. The results are summarized in the following. The attainability of the ignition in INTOR is very sensitive to the physical model and operation scenario.

In ideal case, in which density and temperature profile is parabolic-like and effects of helium particle accumulation and impurity contamination are neglected and ripple diffusion is very low, most of the guiding parameters are almost reasonable to achieve the ignition. However, present guiding parameters have no margin to the non-ideal effects i.e. flat density distribution, high beta value (due mainly to the helium particle accumulation and slightly poor energy confinement), impurity contamination and ripple diffusion. To overcome these non-ideal effects, it might be preferable to increase target density by strengthening toroidal field up to 5.5 T at the center or to increase minor radius by 20 ~ 30 cm for improvement of energy confinement time.

In determining the INTOR parameters, it might be risky to stick to particularly narrow range of design parameters. It is difficult to fix the INTOR parameters at this time because each parameter is not independent from the others and compatibility has not yet been investigated in detail. For instance, other reasonable design parameters are shown to be possible (see Appendix).

Radial diffusion of impurity is well described by a neoclassical diffusion superposed by an anomalous one for protons. Roughly 80 % of the impurity flux entering the plasma is shielded in the plasma outer edge region even in the discharge without divertor. For diverted discharges, the accumulation of impurities is reduced by a factor of 3 to 4 compared to non-diverted discharges.

When we can expect temperature-screening effect and have 1.0-1.5 % margin of β value, we can allow 5-10 % light impurity concentration and expect sufficient edge-cooling by light impurities without decrease of fusion power. However, when this effect is small or neglected, large minor radius of 1.4-1.5 m might be required to attain required τ_E for ignition.

Nearly uniform plasma heating is possible by neutral beam injection with 200 keV. Injection power of 70~80 MW is required to ignite the

plasma within 5 seconds.

The effect of toroidal field ripple on (i) ion thermal conductivity χ_i , (ii) transport of the reacting tail of the thermal ion distribution, can be suppressed sufficiently when the amplitude of the ripple is below 0.5 % in hot central region. Loss of fast ions due to toroidal field ripple during slowing down is about 15 % for injection angle of 75° .

Total orbit loss fraction of α -particle is 4.7 % for broad current density profile and 1.7 % for sharp one. Even when the effect of toroidal field ripple is taken into account, loss fraction of α -particle during slowing down is very small and can be neglected (below 2 % for 1 % ripple). Alpha particle heating profile is almost the same as the birth profile of alpha particles.

Synchrotron radiation loss can be suppressed within 5 % of alpha particle heating for the wall reflection coefficient of 0.4, when the population ratio of runaway electron is suppressed below 10^{-4} .

DATA BASE ASSESSMENT OF ENERGY AND PARTICLE CONFINEMENT FOR INTOR

1. Assessment of Empirical Scaling Law

A number of empirical scaling laws were proposed, which could be applied to the prediction of performances of the future tokamaks. However, it is uncertain that these scaling laws, which were obtained only in joule heating regime, can be extended to multi-keV region, since the exact temperature dependence on these scaling laws has not been made clear. This is only natural, since the temperature is not an independent variable but dependent one for plasma current, etc. in the joule-heated plasmas.

The $\bar{n}a^2$ scaling law was found to reproduce experimental results obtained in a number of currently operating tokamak devices. Moreover, recent experiments at PLT¹⁾, in which the temperature of several keV has been attained by NBI heating, show that $\bar{n}a^2$ scaling law is applicable even to the plasma in the regime of trapped particle instabilities. In these experiments, $P_h > P_j$ and $\nu_i^* < 0.1$ (P_h : NBI heating power, P_j : joule heating power, $\nu_i^* = \nu_{ii}^{eff} / \omega_{bi}$: ion's collisionality, where ν_{ii}^{eff} is the effective ion collision frequency and ω_{bi} is ion bounce frequency), and the trapped particle instabilities are not excited. Thus, $\bar{n}a^2$ scaling law may be applicable even to higher temperature plasma in the future large tokamaks.

There have been proposed several kinds of expressions for this scaling law. It is because the influence of impurities on these scaling laws have not yet been made clear. One of these scaling laws is given as

$$\tau_E = C_s \bar{n}_e a_\lambda^2 \quad (\text{s}), \quad (1)$$

where \bar{n}_e and a_λ are the average plasma density and limiter radius of the devices, respectively. In a plasma of low metallic impurity concentrations, proportional coefficient C_s is given as follows depending on light impurity concentration.

(1) For large light impurity concentration

$$C_s = 5 \times 10^{-21} \quad (\text{Fig. 1})^2, \quad (2)$$

$$\text{or } 2 \sqrt{q_a} \times 10^{-21} \quad (\text{Fig. 2})^3. \quad (3)$$

(2) For small light impurity concentration,

$$C_s = 5 \sqrt{q_a} \times 10^{-21} \quad (\text{Fig. 2})^{4),5)} \quad (4)$$

Here, q_a is the safety factor at the plasma surface. Another expression for $\bar{n}a^2$ scaling law is given as

$$\tau_E = (1.5) \sqrt{q_a} \times 10^{-20} \bar{n}_e a_{\text{half}}^2 \text{ (s)} \quad (\text{Fig. 3}) \quad (5)$$

where a_{half} is a plasma radius at which the electron temperature is a half of its center value. In this expression, the influence of impurities on τ_E is implicitly reflected in a_{half} (suggested by DIVA group).

The result shown in Eq. (4) is obtained in JFT-2 and DIVA/JFT-2a experiments in which light impurity concentration is reduced by employing the titanium gettering in the former and gold-plated first wall in the latter, while the electron temperatures are still sharply distributed. In general, low gas impurity concentration causes the increase of metallic impurity concentration associated with the increase of boundary temperatures because of reduced edge-cooling by light impurities. So metallic impurity concentration has to be suppressed by the edge-cooling with hydrogen gas puffing as in the JFT-2 experiment, and by the shielding effect of a poloidal magnetic limiter as in the DIVA experiment. The improvement of the coefficient C_s to a value much higher than $5 \sqrt{q_a} \times 10^{-21}$ appears rather difficult by further impurity control since the radiation losses due to impurities are already reduced to less than 30 % of joule heating power in the above experiments. However, if we can attain a flat distribution of the electron temperature maintaining low impurity concentration, the coefficient C_s can be improved to a value more than $5 \sqrt{q_a} \times 10^{-21}$.

Expression of Eq. (5) implies the above considerations. We cannot expect $a_{\text{half}} \sim a_l$, but will be able to expect $a_{\text{half}} \sim 0.8a_l$ at maximum in the future large tokamaks. In this case, C_s can be improved by 1.7 times at maximum from the relations,

$$C_s \bar{n} a_l^2 = 1.5 \times 10^{-20} \sqrt{q_a} \bar{n}_e (0.8 a_l)^2 .$$

Although $\tau_E \lesssim 2\tau_{Ee}$ in the present-day tokamaks, we can expect $\tau_E \geq 2\tau_{Ee}$ in the future large tokamaks since $\tau_{Ei} \gg \tau_{Ee}$, $\bar{T}_i \sim \bar{T}_e$ and $\tau_E = (\bar{T}_e + \bar{T}_i) \tau_{Ee} \tau_{Ei} / (\tau_{Ei} \bar{T}_e + \tau_{Ee} \bar{T}_i) \sim \tau_{Ee} (1 + \bar{T}_i / \bar{T}_e)$, where τ_{Ee} and τ_{Ei} are energy confinement times for electron and ion, respectively. Therefore Eqs. (4) and (5) approximately give τ_{Ee} in the large tokamaks. Assuming $\tau_E = 2\tau_{Ee}$, the required a_{half} in JT-60 and INTOR to attain their target is estimated

as follows,

$$\frac{a_{\text{half}}}{a_{\ell}} = 0.56 \sim 0.69 \text{ for JT-60 } (\bar{n} = 5 \times 10^{19}/\text{m}^3, a_{\ell} = 0.95\text{m}, \tau_E = 0.4 \sim 0.6\text{s})$$

and

$$\frac{a_{\text{half}}}{a_{\ell}} = 0.46 \sim 0.57 \text{ for INTOR } (\bar{n} = 1.2 \times 10^{20}/\text{m}^3, a_{\ell} = 1.2\text{m}, \tau_E = 1.7 \sim 2.7\text{s})$$

The parabolic distribution of the electron temperature is sufficient to satisfy the above requirements in JT-60 and INTOR.

References

- 1) H. Eubank, et al, 7th Int. Conf. Plasma Phys. and Controlled Nuclear Fusion Research, Innsbruck (1978) IAEA-CN-37-C-3.
- 2) T. Tazima, JAERI-M 7717 (1978, in Japanese).
- 3) E. Apgar, et al, Proc. 6th Int. Conf. Plasma Phys. and Controlled Nuclear Fusion Research, Berchtesgaden (1976) 1. IAEA, Vienna.
- 4) S. Konoshima, et al, J. Nuclear Materials 76 & 77 (1979) 581.
- 5) Y. Shimomura, H. Maeda, *ibid* (1979) 45.

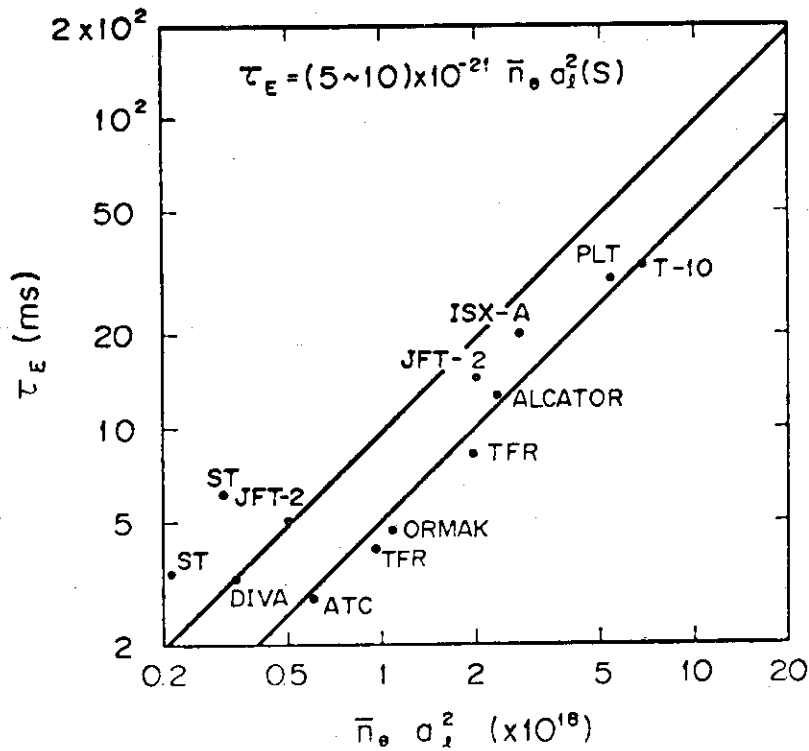


Fig. 1 Empirical $\bar{n}a^2$ scaling law of energy confinement time.

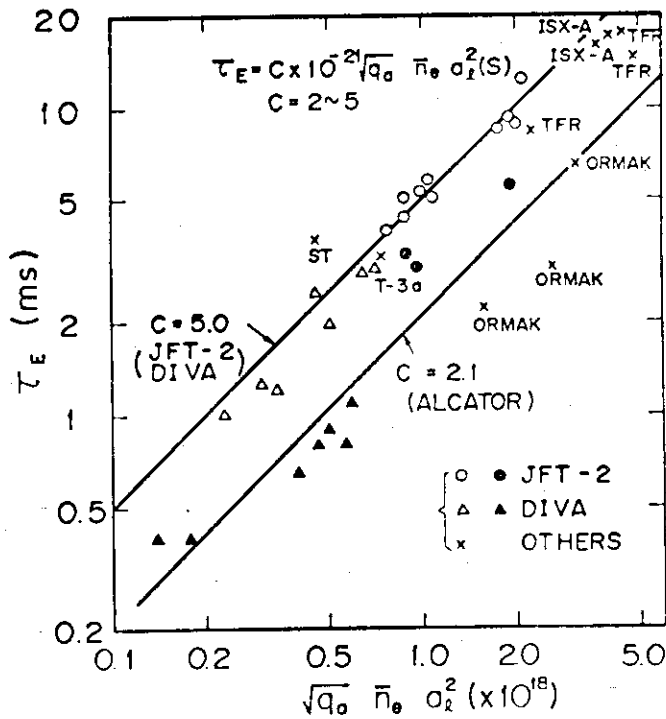


Fig. 2 Impurity effect on empirical $\sqrt{q_a} \bar{n} a^2$ scaling law of energy confinement time.

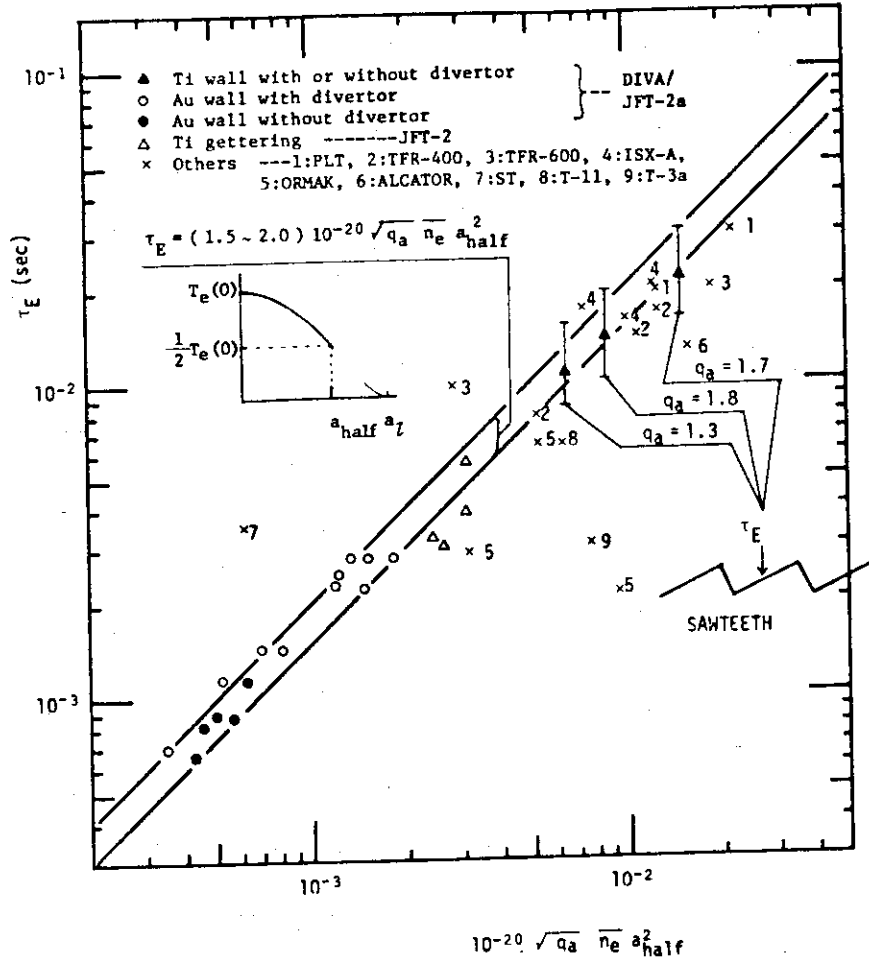


Fig. 3 Empirical $\sqrt{q_a} \bar{n}_e a_{\text{half}}^2$ scaling law of energy confinement time.

2. Detailed Studies on INTOR Guiding Parameters by Zero-Dimensional Model

INTOR Guiding Parameters are summarized in Table 1. The conditions, under which the plasma in the device of INTOR guiding parameters can reach the self-ignited state and concurrently 1 MW/m^2 neutron wall loading can be achieved, are investigated in terms of scaling law and also by using zero-dimensional simulation code.

1) The premises of the calculations

(1) Scaling law

We adopt $\bar{n}a^2$ scaling law for the energy confinement time τ_E . This scaling law is given as

$$\tau_E = (2 \sim 5) \times 10^{-21} \sqrt{q_a} \bar{n}a^2 \quad (\text{Fig. 1}) \quad (1)$$

This τ_E is almost attributed to the electron's anomalous transport, so that $\tau_E \sim \tau_{Ee}$ in the present day tokamaks (Fig. 2). There are several possibilities for the improvement of τ_E .

(a) Since ion's thermal conductivity is nearly neoclassical value, $\tau_{Ei} \gg \tau_{Ee}$ in future higher temperature plasma. In NBI or α -heating regime, $\bar{T}_i \sim \bar{T}_e$. Thus,

$$\tau_E = \frac{\tau_{Ee} \tau_{Ei} (\bar{T}_e + \bar{T}_i)}{\tau_{Ei} \bar{T}_e + \tau_{Ee} \bar{T}_i} \sim \tau_{Ee} \left(1 + \frac{\bar{T}_i}{\bar{T}_e}\right) \sim 2\tau_{Ee} \quad (2)$$

(b) Although the effect of noncircularity on τ_E has not been made clear, it could be expected that $\tau_E \propto \bar{n}ab$.

(c) Light impurity control improves the proportional coefficient up to $5 \times 10^{-21} \sqrt{q_a}$.

(2) Density and temperature profile

Parabolic spacial distribution is assumed both for density and temperature. In this case, total fusion power becomes larger by a factor of $1.5 \sim 2.5$ than in the case of using only their averaged values \bar{n} , \bar{T} ; e.g. when $\bar{T}_i = 10 \text{ keV}$,

$$\int dV n_i^2 \langle \sigma v \rangle = 1.8 \bar{n}^2 \langle \sigma v \rangle_{\bar{T}} V \quad (3)$$

Consequently, $\bar{n}\tau_E$ value required for ignition can be reduced than in the case using \bar{n} , \bar{T} (Fig. 3).

2) Target temperature and density

(1) Target temperature

Three major criteria must be considered to set the target temperature; (i) self-ignition, (ii) neutron wall loading, (iii) plasma beta value. Target temperature must be determined so that the plasma can reach the self-ignited state and concurrently 1 MW/m^2 neutron wall loading can be obtained within a critical β_t value for equilibrium and stability.

Figure 4 shows the required β_t value for the self-ignition and for various neutron wall loading as a function of \bar{T}_i (Toroidal field is 5 tesla). The condition for self-ignition has a certain ambiguity. Temperature of about 10 keV can achieve 1 MW/m^2 neutron wall loading and concurrently can achieve the self-ignited state within the ambiguity of the scaling law near the minimum value of β_t .

Thus, we set 10 keV as a target temperature.

(2) Target density

Since $\beta_t \sim 4\%$, the target density is $\bar{n} = 1.2 \times 10^{20} \text{ m}^{-3}$. When the safety factor q_a is set as $q_a = 2.5$, β_p becomes 2.6. These beta values might be rather severe for external and internal instability with low mode number. This difficulty could be avoided by low q_a discharge (Recent experiment of DIVA shows that very low q_a ($q_a < 2$) operation is possible by plasma profile control¹).

(3) Neutral beam injection heating

It is necessary to heat the plasma with this density uniformly by neutral beam injection. To avoid the surface heating of the plasma, P_{in}/nT must be nearly uniform over the whole magnetic surface. (P_{in} : input power). To avoid the ripple loss of the injected neutral ions, injection angle must be more than $10 \sim 15^\circ$ from the normal of the magnetic axis.

Figures 5 and 6 show heat deposition profile P_{NBI}/nT for deuterium injection with 150 keV and 200 keV. Injection angle is 15° . The model of calculation is: (i) instantaneous heat transfer to the field particles from the injected neutrals at the instant of their ionization or charge exchange, (ii) the density profile of field particles is parabolic, (iii) the effect of multi species of the injected particles is taken into account. Both in Figs. 5 and 6, the surface heating of the plasma becomes rather severe in

the latter period of NBI. If α -particle heating is taken into account, this situation is considerably mitigated (Figs. 7 and 8).

Thus, injection energy of 200 keV seems to be possible to heat the plasma nearly uniformly.

3) Relation between energy confinement time and Q value

1 MW/m² neutron wall loading can be achieved for $\bar{T} = 10$ keV, $\bar{n} = 1.2 \times 10^{20}$ m⁻³. It is not so definite, however, that the plasma with these parameters can reach the self-ignited state, since the scaling law has a certain ambiguity.

Figure 9 shows the relation between the total energy confinement time τ_E and Q ($\equiv P_f/P_{NBI}$) value (solid line). Dotted line in Fig. 9 shows a required improvement factor C to achieve a given τ_E , which is obtained by the following equations.

$$P_{\chi i} + P_{br} + \frac{3}{2} \frac{\bar{n} \bar{k} \bar{T}}{\tau_{Ee}} = \frac{3 \bar{n} \bar{k} \bar{T}}{\tau_E}, \quad (4)$$

$$\tau_{Ee} = C \times 5 \times 10^{-21} \bar{n} a^2, \quad (5)$$

where $P_{\chi i}$ and P_{br} are ion's heat conduction loss given by neoclassical theory and bremsstrahlung radiation loss respectively. Although $C \sim 1$ seems to be sufficient to achieve the self-ignited state, actually $C \sim 1.5$ will be required when other losses such as energy losses due to impurities, charge exchange loss, synchrotron radiation loss.

4) Detailed analysis by zero-dimensional simulation code

(1) Model of calculation

Density and temperature profiles are fixed to parabolic distribution are taken into account.

Transport model: (i) transport loss due to electron is given as $\frac{3}{2} \frac{\bar{n}_e \bar{k} \bar{T}_e}{\tau_{Ee}}$ (τ_{Ee} : given by $\bar{n} a^2$ scaling law), (ii) ion's heat conductivity is neoclassical value multiplied by a numerical factor.

Ignition approaches of following two cases are calculated.

$$\text{Case I: } \tau_{Ee} = 5 \times 10^{-21} \bar{n} a^2, \quad \chi_i = 3(\chi_i)_{\text{neoclassical}}$$

$$\text{Case II: } \tau_{Ee} = 5 \times 10^{-21} \sqrt{q_a} \bar{n} a^2, \quad \chi_i = (\chi_i)_{\text{neoclassical}}$$

(2) Results of calculations

Case I (Fig.10): The self-ignited state cannot be attained within β_t limitation (4 %), even when $\bar{T}_e = 10 \sim 12$ keV is reached by 80 MW injection heating.

Case II (Fig.11): The self-ignited state at $\bar{T} \sim 10$ keV can be attained by 50 MW injection for 4 seconds. It is required that scaling like that of Case II be held to achieve the ignition. It is not so difficult to obtain 50 MW injection power from machine design point of view.

(3) Permissible impurity level

Simplified expression for the related energy loss due to impurities is used²⁾;

$$P_r = 10 \left(\frac{\bar{n}_i}{10^{20}} \right)^2 \frac{N_z}{N_i} \times 10^2 M_z^3 \quad (\text{W/m}^3),$$

where \bar{n}_i , N_i , N_z and M_z are the mean ion density, the total number of ions and impurities and atomic mass number, respectively.

Figures 12 and 13 show that the self-ignited state can be attained even when the plasma is contaminated by 0.02 % molybdenum impurity for 50 MW injection and 0.03 % for 70 MW injection, if β_t could be more than 4 %.

When β_t value is restricted within 4 %, the self-ignited state can be attained when the plasma is contaminated by 0.01 % molybdenum impurities (Fig.14), while cannot be attained for 0.02 % contamination (Fig.15).

References

- 1) DIVA Group, JAERI-M 8205 (1979)
- 2) T. Tazima, Y. Nakamura, K. Inoue, Nuclear Fusion 17 (1977) 3.

Table 1 Plasma and device parameters which can achieve the self-ignition and 1 MW/m^2 neutron wall loading.

1. Device parameters	
(1) Major radius (R) ;	5 m
(2) Minor radius (a) ;	1.2 m
(3) Noncircularity (κ) ;	1.5 (b = 1.8 m)
(4) Plasma volume (V) ;	213 m^3
(5) Plasma surface area (S_p) ;	300 m^2
(6) Wall surface area (S_w) ;	350 m^2
(7) Magnetic field at plasma center (B_t) ;	5 T
(8) Plasma current (I_p) ;	4.7 MA (5.9 MA)
(9) Safety factor (q_a) ;	2.5 (2.0)
2. Plasma parameters	
(1) Average ion temperature (\bar{T}_i) ;	10 keV
(2) Average ion density (\bar{n}_i) ;	$1.2 \times 10^{20} \text{ m}^{-3}$
(3) Toroidal beta value (β_t) ;	4 %
(4) Poloidal beta value (β_p) ;	2.6 (1.6)
(5) Confinement time (τ_E) ;	$\geq 1.5 \text{ sec}$
(6) Effective charge (Z_{eff}) ;	1.5 ~ 2.0
(7) Total fusion power (P_f) ;	400 ~ 450 MW
(8) Neutron wall loading (P_{wn}) ;	1 MW/m^2
(9) Alpha heating power (P_α) ;	80 ~ 90 MW
(10) NBI heating power (P_{NBI}) ;	50 ~ 70 MW
(11) NBI injection energy (E_b) ;	200 keV
(12) NBI heating time (T_{NBI}) ;	$\sim 5 \text{ sec}$

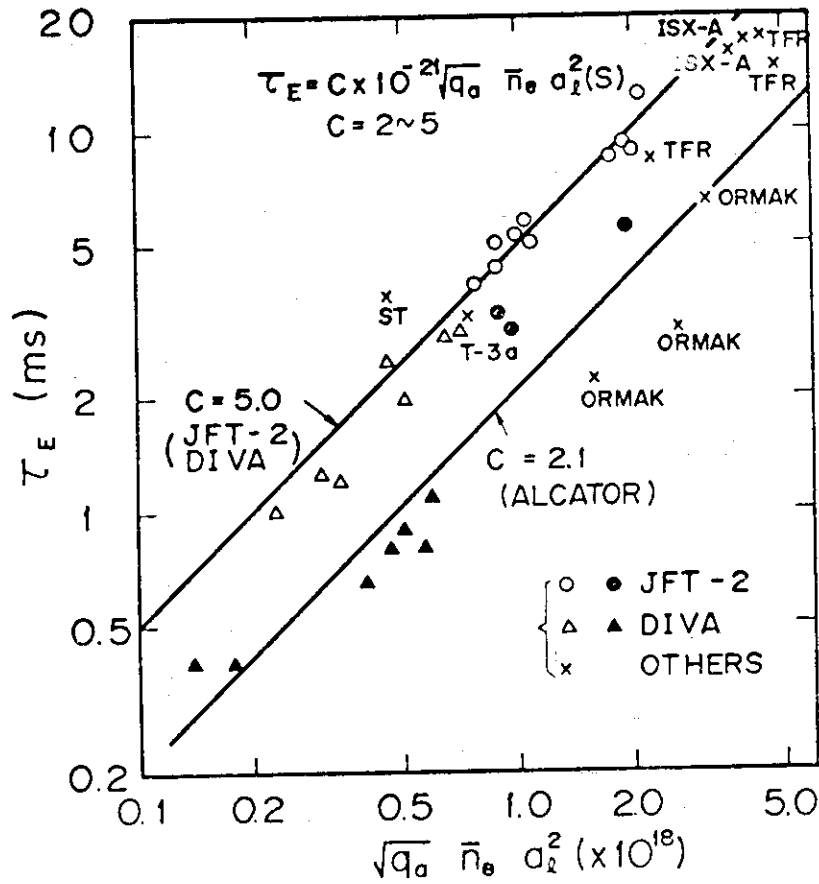


Fig. 1 Empirical $\bar{n}a^2$ scaling law of energy confinement time.

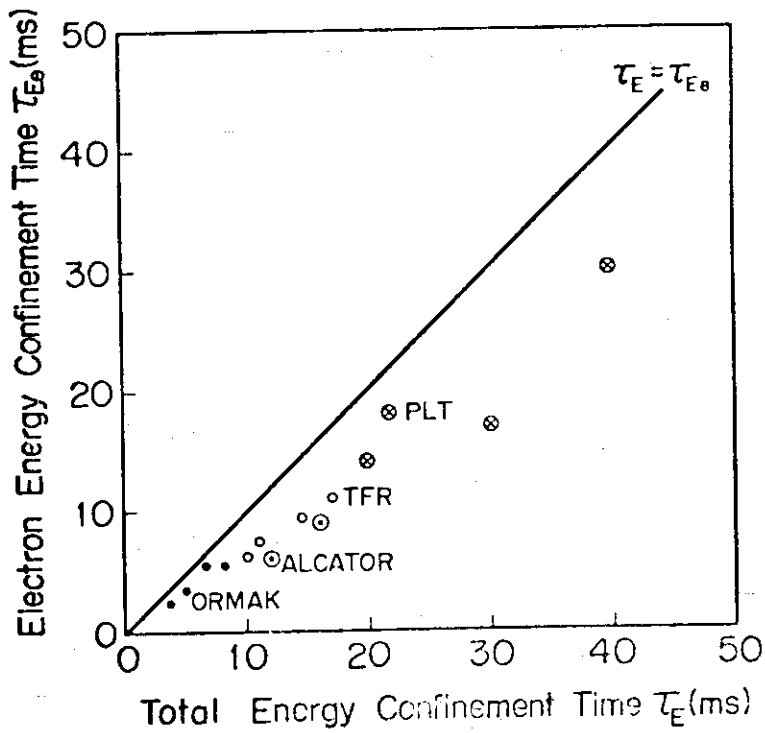


Fig. 2 Comparison of total energy confinement time τ_E and electron's energy confinement time τ_{Ee} in the present day tokamaks.

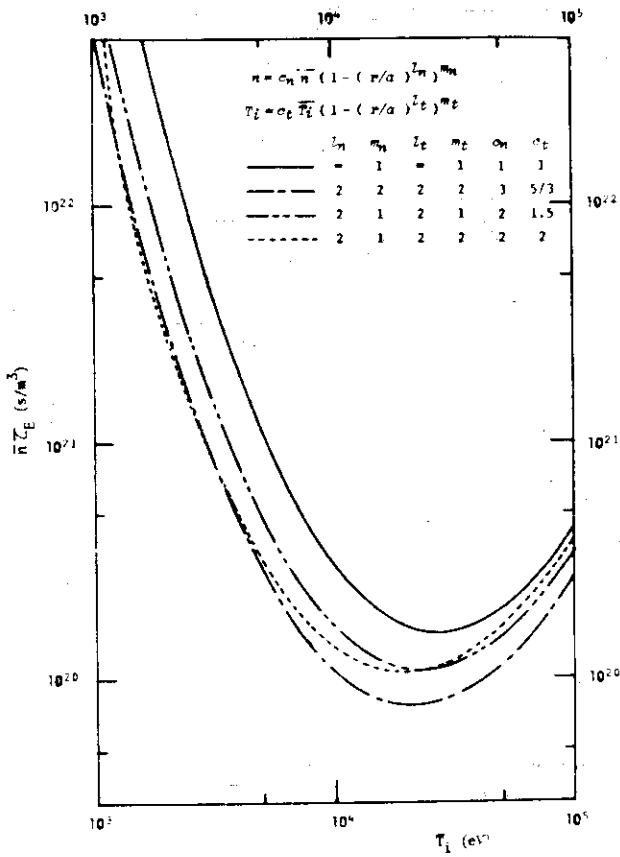


Fig. 3

Dependence of required \bar{n}_E value for self-ignition on the distributions of density and temperature.

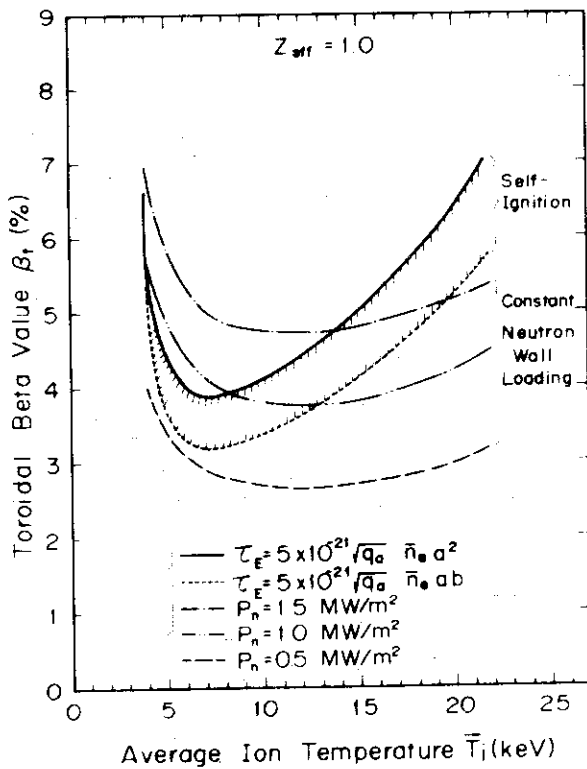


Fig. 4

Required toroidal beta value for self-ignition and for various neutron wall loading as a function of \bar{T}_i . Toroidal field is 5T. Two ignition lines represent the ambiguity of scaling law.

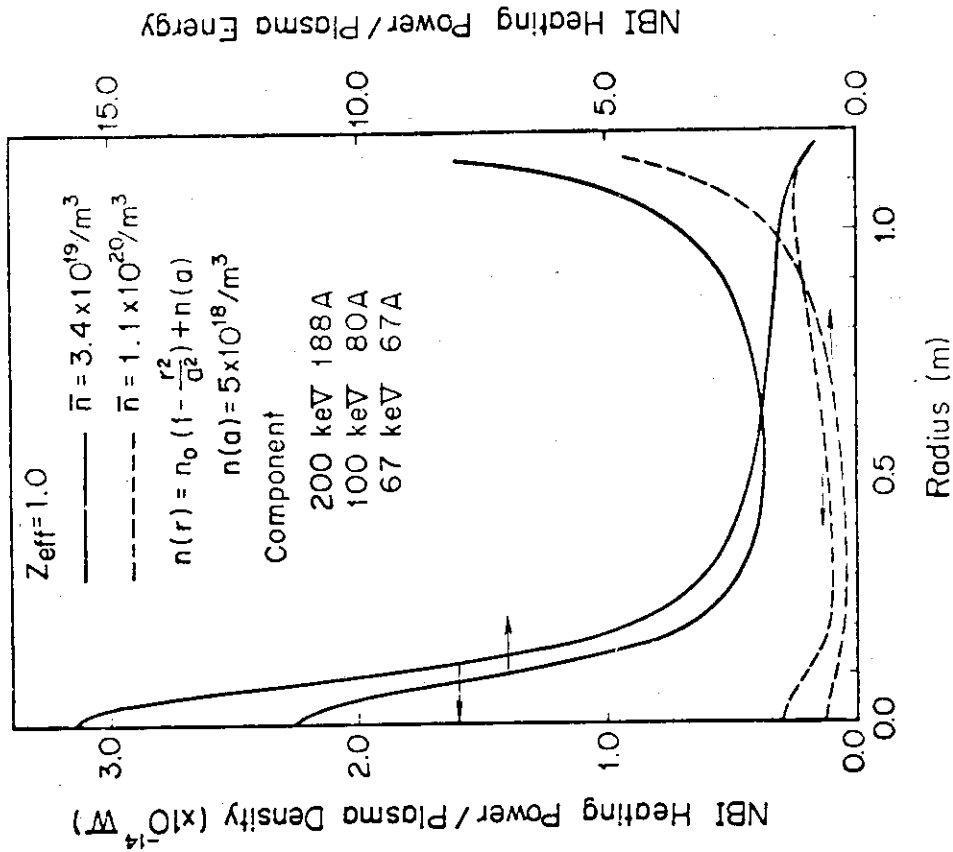


Fig. 6 Heat deposition profile by NBI heating of deuterium injection with 200 keV.

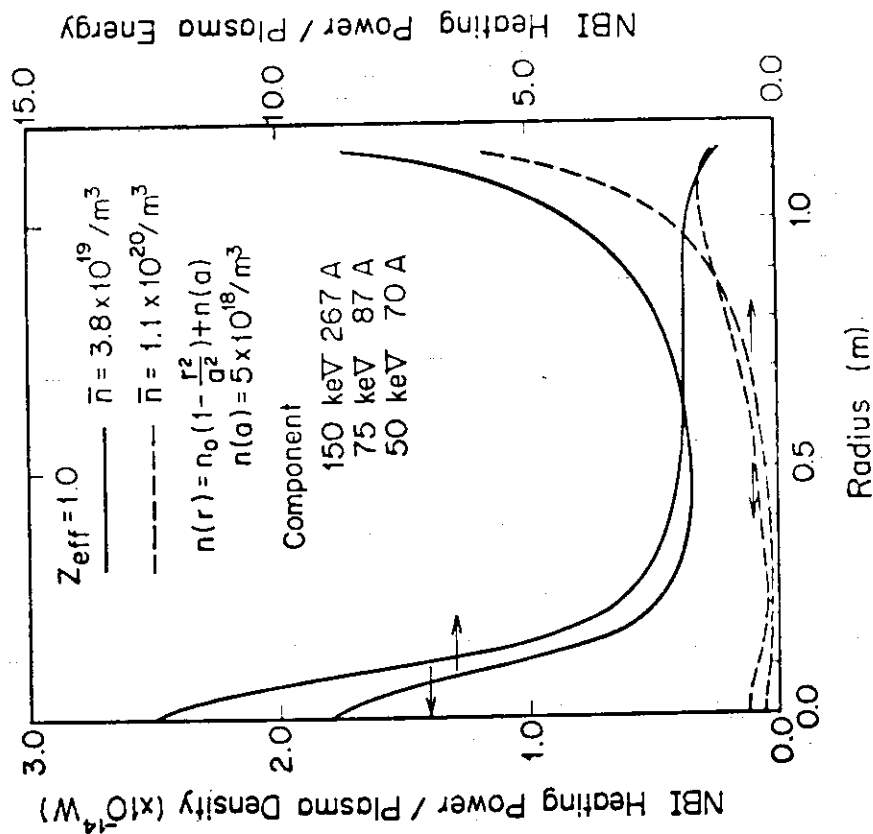


Fig. 5 Heat deposition profile by NBI heating of deuterium injection with 150 keV.

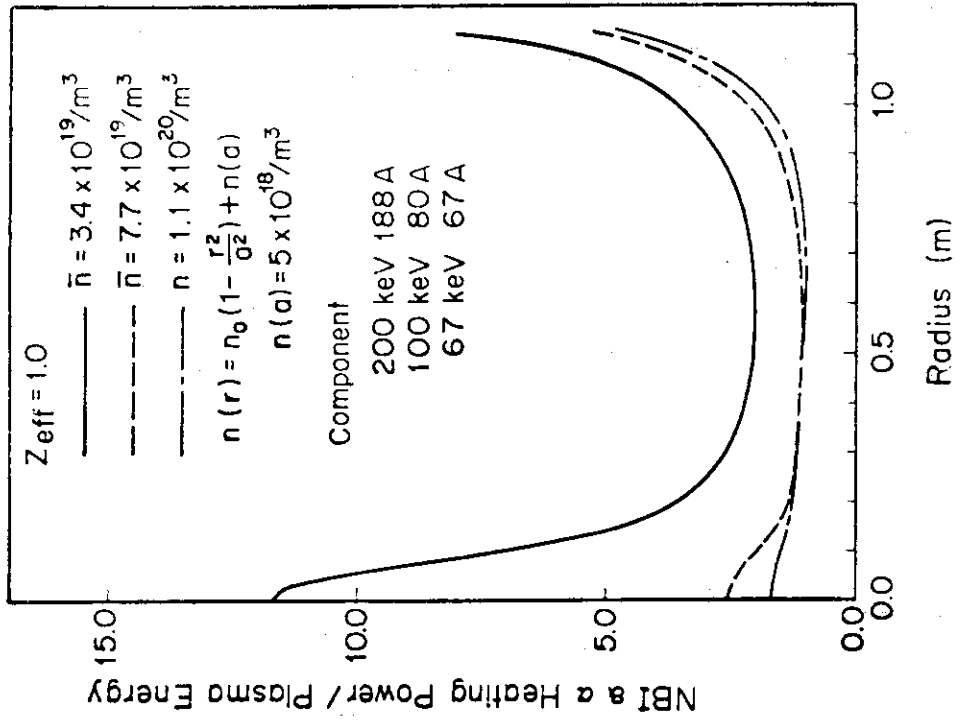


Fig. 8 Heat deposition profile both by α -particle heating and NBI heating of deuterium injection with 200 keV.

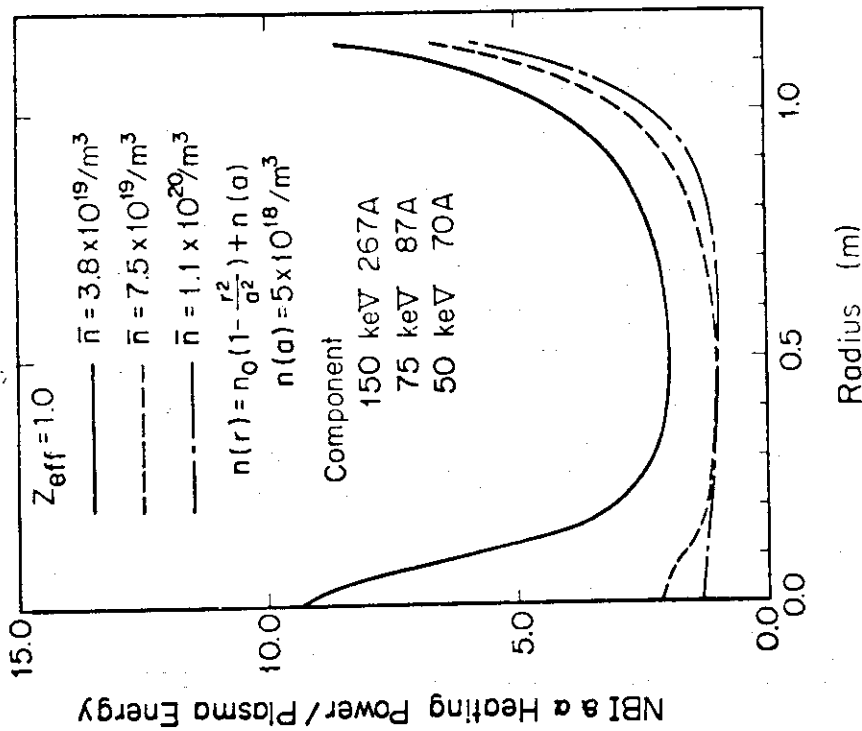


Fig. 7 Heat deposition profile both by α -particle heating and NBI heating of deuterium injection with 150 keV.

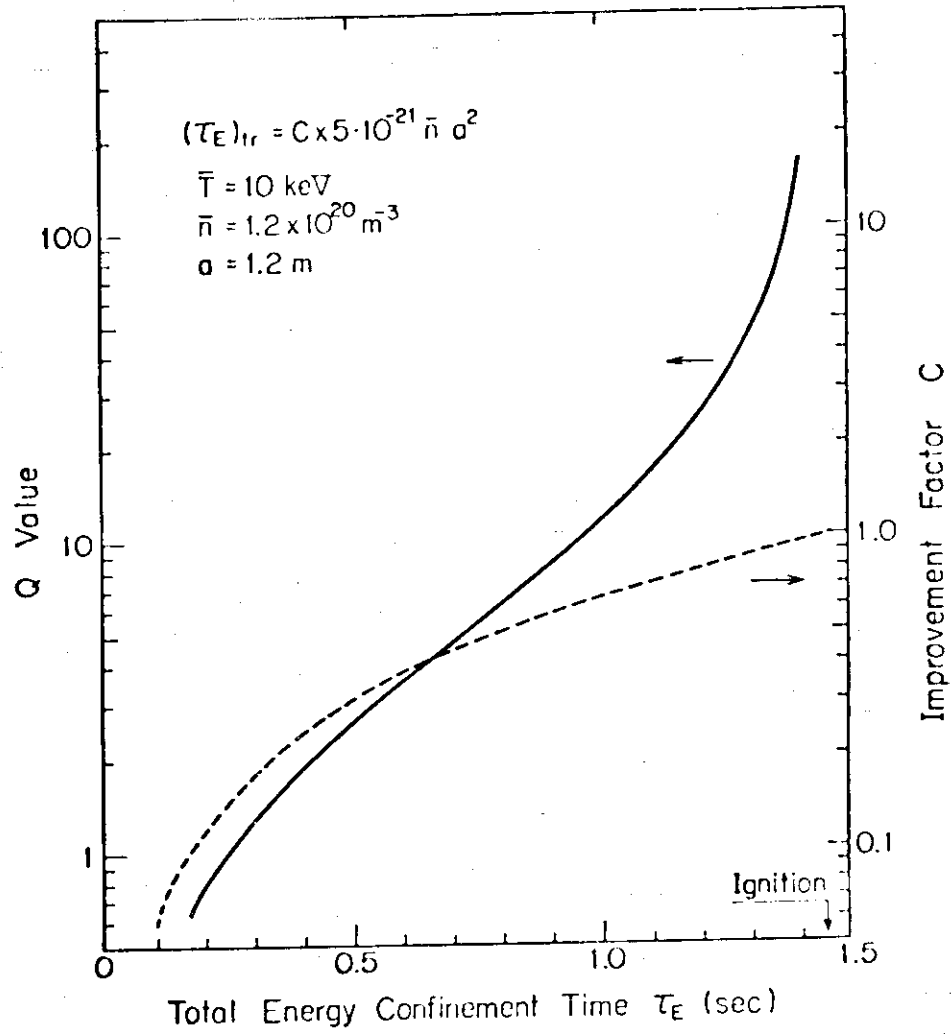


Fig. 9 Relation between total energy confinement time τ_E and Q value (solid line). Dotted line shows a required improvement factor to realize a given τ_E by $\tau_{Ee} = C \times 5 \times 10^{-21} n a^2$ scaling law.

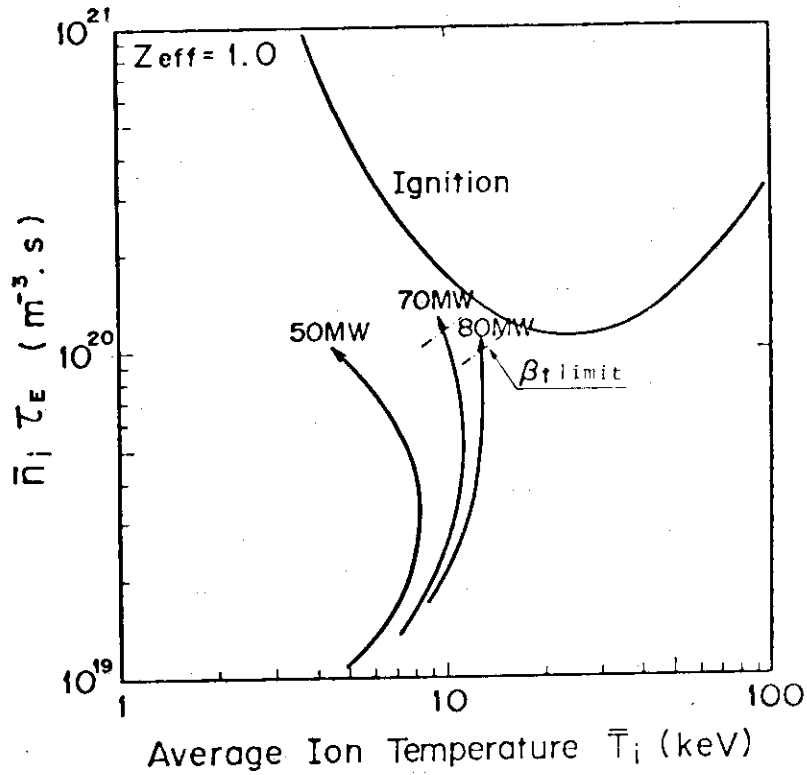


Fig. 10 Ignition approach of Case I with injection power of 50, 70 and 80 MW.

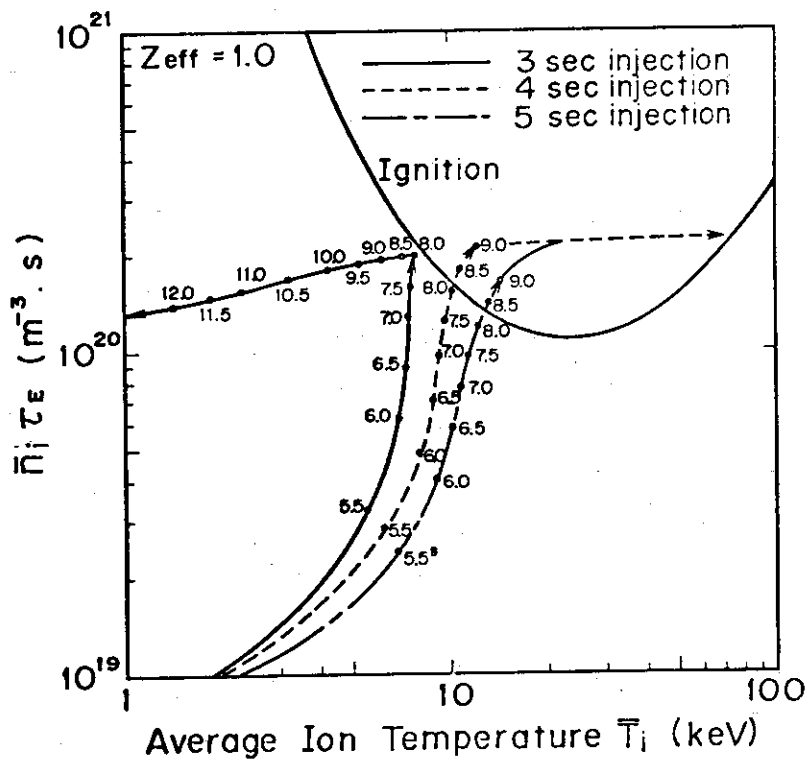


Fig. 11 Ignition approach of Case II with injection power of 50 MW.

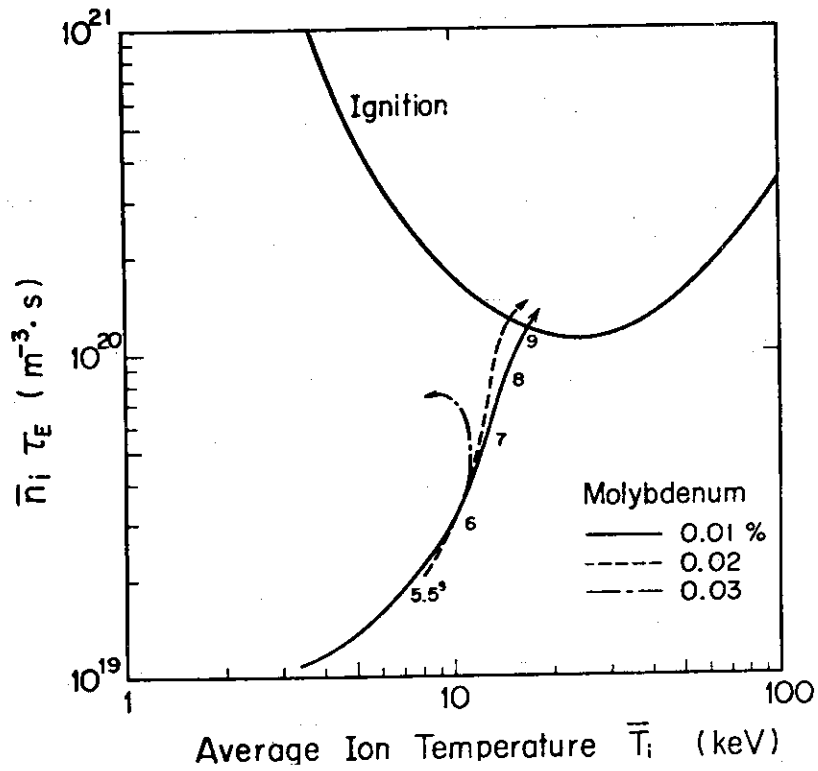


Fig. 12 Ignition approach when the plasma is contaminated by molybdenum impurities. 50 MW injection power is assumed.

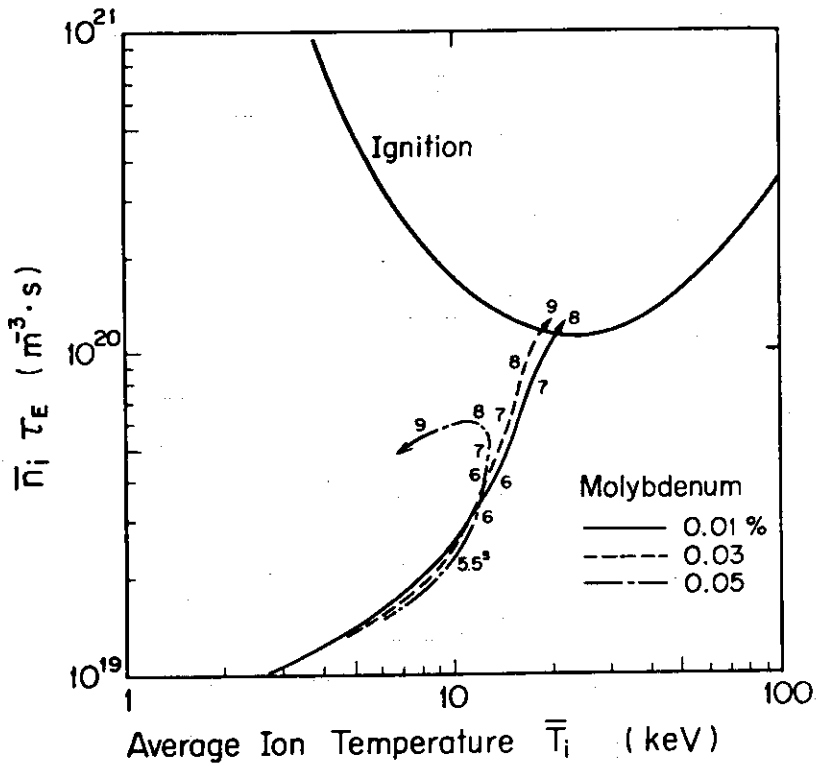


Fig. 13 Ignition approach when the plasma is contaminated by molybdenum impurities. 70 MW injection power is assumed.

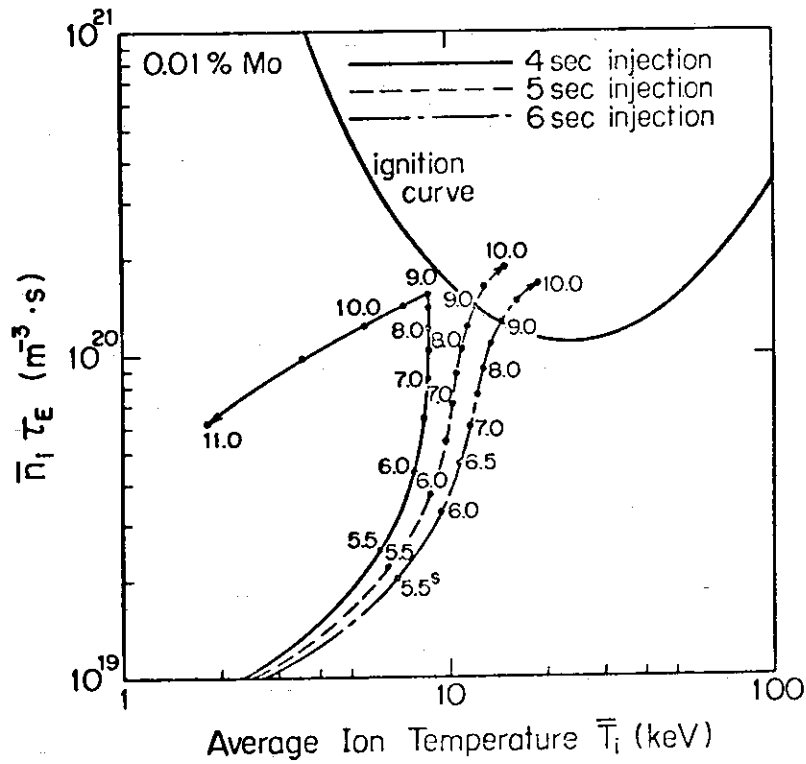


Fig. 14 Ignition approach when the plasma is contaminated by molybdenum impurities of 0.01 %. β_t is restricted within 4 %.

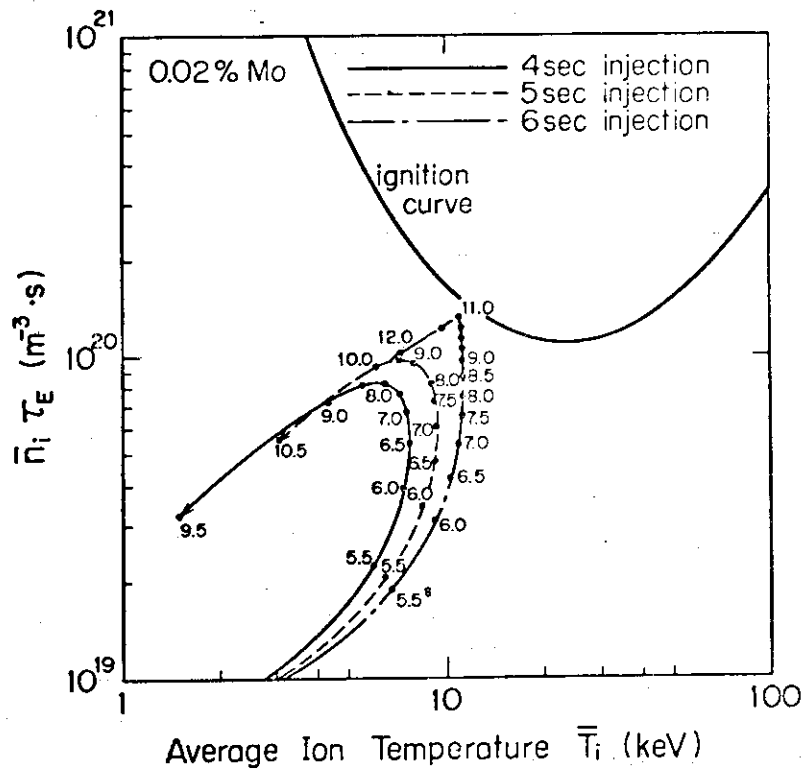


Fig. 15 Ignition approach when the plasma is contaminated by molybdenum impurities of 0.02 %. β_t is restricted within 4 %.

3. Detailed Studies on INTOR Guiding Parameter by One Dimensional Simulation Code

In this section, we examine the ignition approach in INTOR guiding parameters by using transport code, in which deuterium, tritium, α -particles and ash helium particles are treated separately. The models of the code are summarized in the following.

1) Transport model

We employ the following transport model to simulate the ignition approach and burning phase of INTOR.

$$\chi_e = \frac{5 \times 10^{19}}{n_e} \frac{1}{\kappa} \quad (\text{m}^2/\text{s}) \quad , \quad (1)$$

$$\chi_i = 3 \times (\chi_i)_{\text{neoclassical}} \times \frac{1}{\kappa} + \chi_{\text{ripple}} \quad , \quad (2)$$

$$D = \chi_e / 12 \quad . \quad (3)$$

The transport code only calculates circular cross section, whereas the cross section of INTOR is non-circular. Thus, instead of employing $a_{\text{eff}} = \sqrt{ab}$, we divide each transport coefficient by κ , so that we equate the energy and particle losses and gains per unit volume in transport equations to those of using a_{eff} . Thus, 50 MW of injection power in our calculations corresponds to 75 MW in that of using a_{eff} . Both will give completely the same results.

We also take account of ripple trap diffusion χ_{ripple} . The expression of χ_{ripple} is the one obtained by Connor and Hastie¹⁾. Radial dependence of toroidal field ripple is assumed to be $\delta(r) = \delta_a (r/a)^2$ for simplicity. In addition, we take account of inward particle flux due to Ware pinch effect to explain the density distribution in PLT experiments.

2) Heating model

Injected beams and α -particles are separated into three energy groups during their slowing down processes. Each group slows down in classical slowing down time. Only single energy component for the initial energy of the injected neutral beam is considered.

3) Recycling conditions and impurities

Both deuterium and tritium particles recycle with a given re-

cycling rate, while helium particle recycling is not taken into account. Impurity effects are neglected in all of the calculations.

4) Ignition scenario

The start up scenario is schematically shown in Fig. 1. We employ pellet injection for tritium density build-up in joule heating phase. By this method, the plasma density is increased beforehand suitably for NBI heating. The plasma current rise time is 5 seconds. Neutral beam injection heating is started at $t = 5$ sec. We employ deuterium injection with 200 keV energy. NBI is turned off at $t = 9 \sim 10$ s. Particle recycling and fueling method will have a great influence on the attainability of the ignition through the density distribution. In addition, particle flux to the first wall and limiter or the divertor plate is greatly affected by the density distribution. The characteristic properties of the scrape-off layer plasma are determined in large part by the particle flux, so that the design of ash exhaust and impurity control mechanisms will be altered by the estimation of particle flux. Thus, we employ puffing and pellet injection for the fueling method, and calculate for various recycling conditions.

5) Results of simulations

A typical example of the ignition approach by gas puffing and recycling for the fueling method is shown in Fig. 2.

The energy of neutral particles are assumed to be 500 eV. In poloidal divertor case, more than half of the fuel particles, which flow into the divertor chamber, will flow back to the main plasma by mainly charge exchange process. These backflow neutrals have the same energy as that of the scrape-off layer plasma. In addition, considerable fraction of charge exchange neutrals, which hit the first wall will reflect back into the main plasma without large loss of energy, so that 500 eV is reasonable for these neutrals. For the gas puffing neutrals, however, 500 eV is rather overestimated. In a realistic system, the number of neutrals with higher energy will be larger than that of cold neutrals.

The attainability of the ignition is marginal. In fact, the ignition is achieved for 0.5 % toroidal field ripple, while the ignition is failed to be achieved for 0.8 % ripple. In the latter case, the plasma once enters into the ignition region. However, as the

time elapses, the density profile becomes broad, so that the temperature gradually falls due to the increase of ripple diffusion and due to the decrease of α -heating power in the center, and finally it goes out of the ignition region. Time evolutions of various plasma parameters are shown in Fig. 3. Although \bar{T}_i is considerably high for 0.5 % field ripple, it can be lowered down to 12 ~ 13 keV if suitable field ripple is applied or NBI heating time and power are suitably adjusted. Density profile is always very broad and slightly hollow. For this reason, the plasma is very sensitive to the field ripple, and moreover, higher beta value ($> 4\%$) is required to attain the ignition.

Figure 4 shows the ignition approach by using pellet injection and 50 % recycling, which corresponds to the simple poloidal divertor case, for the fueling method. Energy of recycling neutrals is again assumed to be 500 eV. Injection power is 50 MW.

We have assumed that the particle source profile by pellet injection is linearly decreasing one as shown in Fig. 5²⁾. Since the density profile is greatly affected by the penetration depth ℓ of the injected pellet, we evaluate ℓ/a at each time step in accordance with the density and temperature profile by the following relation²⁾

$$U r_p^{5/3} = \frac{2.92 \times 10^{-6} a}{M^{1/3}} \int_{\ell/a}^1 L(E_{e\infty}/2)^{1/3} n_{e\infty}^{1/3} E_{e\infty}^{1/6} \{E_{e\infty} + 8.5 \times 10^{-4} E_{e\infty}^2 - \frac{850}{E_{e\infty}} + 75\} d(r/a) .$$

We have assumed that the injection velocity U and the radius r_p of the pellet are 10^4 m/s and 3 mm, respectively. These values seem to be the maximum expectable ones. Time dependence of ℓ/a in accordance with the time evolution of the density and temperature (Fig. 8) is shown in Fig. 6.

Toroidal field ripple is changed appropriately to control the plasma burning. In the early phase of the start up, the field ripple is rather large to prevent the excessive temperature rise. As the time elapses, penetration depth of the injected pellet becomes shallow, so that the density profile becomes broad as in the gas puffing case. And also helium ash accumulates gradually. As a result, the plasma temperature gradually falls unless the field

ripple is lowered. In Fig. 4, burning is sustained for more than 30 seconds by lowering the ripple with sustaining temperature being $\bar{T}_i = 12 \sim 14$ keV. However, the burning cannot be sustained with 0.5 % field ripple. Thus, the self-sustaining with \bar{T}_i below $12 \sim 14$ keV seems to be difficult with realistic toroidal field ripple. At higher temperature, the self-sustaining may be possible with realistic field ripple as in the case of gas puffing. Thus, for the case of broad density profile, the attainability of the ignition seems to be marginal. Favorable dependence of χ_e on T, if exists, or slightly larger device or higher density could attain the ignition rather safely.

When toroidal field ripple is not adjusted, the plasma temperature tends to rise excessively (Fig. 7). However, as the time elapses, the temperature again falls due to the ash accumulation and toroidal field ripple (0.8 %). Time evolutions of various plasma parameters are shown in Fig. 8.

If the density profile is sharp even in large device, the ignition can be attained much easily even when the toroidal field ripple is larger. In fact, when we employ the flat particle source distribution as shown in Fig. 9, the density and temperature profiles in nearly steady state become sharp as shown in Fig. 10. In this case, the ignition can be attained even for 1.5 % ripple (Fig. 11). In Fig. 11, solid line of T_i shows the case, where temperature rise is controlled by field ripple, so that the beta value is not exceeded the critical value too much. In actual case, NBI heating time and power and/or toroidal field ripple are adjusted to suppress the excessive rise of T_i . If no particular control is done, temperature rises up to 25 keV (dotted line of T_i shows the case of 0.5 % field ripple). The profiles of Fig. 10 could also be realized by choosing a suitable transport model in the simulation code, so that such profiles could be observed even for gas puffing or realistic pellet injection in large device by some transport mechanisms. Thus, the attainability of the ignition strongly depends on which density profile we expect.

As for the helium ash accumulation, Figs. 4 and 11 show that in steady state about 15 % ash accumulates for gas puffing case, about 8 % ash for shallow pellet injection case and about 17 % ash for

deep one. Although, in the first and third cases, ash accumulations seem to be rather high, this is due to the higher α -particle source (184 MW α -power in the first case and 175 MW in the third case). In fact, if the α -heating power were lowered down to 90 MW in these cases, the accumulation of ash would be lowered down to 7.3 % ($= 15 \times 90/184$) in the first case and 9 % in the third case. For almost all cases, the accumulations of ash are around 10 % (see Chapter 4 in this article). Note that, in these calculations, helium recycling is not taken into account, so that these are the cases with ideal helium pumping system, or can be considered to be confinement time of helium ash in hot core plasma. When helium particles recycle, the accumulation becomes necessarily large. From Fig. 11, the accumulation time (saturation time) of helium ash is about 20 seconds. Note that, in Fig. 11, the plasma is in self-sustaining state for a while by keeping the fuel amount constant, the temperature gradually falls and finally will go out of the ignition region due to the bremsstrahlung radiation loss by helium particle accumulation. If we reduce the toroidal field ripple somewhat, the self-sustaining state can be restored again (the arrows on \bar{T}_i curve show the time, at which field ripple is lowered.). When about 10 % helium ash accumulates for INTOR plasma, the ash accumulation problem in a commercial reactor will be very severe. The ash accumulation f is represented as $f = \bar{n}_{He} / \bar{n}_i = \tau_{He} P_n / \bar{n}_i a$ (P_n : neutron wall loading, a : plasma minor radius). If we assume $\tau_{He} \propto a^2$, then $f \propto a P_n / \bar{n}_i$. Thus, if $a P_n$ value of a commercial reactor becomes 3 ~ 4 times larger than INTOR value, $f = 30 \sim 40$ %.

6) Summary

Results of 1D simulation calculations are summarized as follows.

- ① The attainability of the ignition in INTOR is very sensitive to the physical model and operation scenario, especially to the density profile.
- ② Flat density distribution is most likely in INTOR even though strong inward particle flux such as Ware pinch effect is considered and realistic pellet injection is employed. In this case, ignition can be achieved in the guiding model only when toroidal field ripple is very small (≤ 0.5 %) and there is no impurity contamination.
- ③ Moreover, sufficient heating of central region by NBI of 200 keV

injection energy is difficult and ripple loss of fast ions becomes serious for such flat density profile.

- ④ Favourable dependence of χ_e on T_e as observed in PLT could make the achievement of ignition easier.
- ⑤ Higher density ($\bar{n}_i > 1.4 \times 10^{20} \text{ m}^{-3}$) could also enable us to achieve ignition.
- ⑥ For sharp density profile, if realized, the ignition can be achieved rather easily in the guiding model when serious impurity contamination can be prevented.

7) Non-Ideal Effects

Based on the results of 1D simulation calculation, the adequateness of INTOR guiding parameters is summarized as follows:

In ideal case, i.e. neglecting the non-ideal effects such as excessive helium particle accumulation, large ripple diffusion, impurity contamination etc, most of the guiding parameters, except for safety factor at the boundary, are almost reasonable to achieve a self-ignited plasma and 1 MW/m^2 neutron wall loading. It is desirable to set the safety factor at the boundary nearly equal to 2 in order to attain high toroidal beta value of $5 \sim 6 \%$, or toroidal field should be increased up to 5.5 T.

However, present guiding parameters have no margin as to the beta value and energy confinement time, and moreover it is not clear whether we can control impurities sufficiently even in a case with the divertor. Therefore, it might be preferable to increase target density by high toroidal field of 5.5 T at the center or to increase minor radius by $20 \sim 30 \text{ cm}$ for improvement of energy confinement time.

At present we have not yet found the optimized solution of INTOR parameters, which is a major task of the next year. It might be risky to stick to particularly narrow range of design parameters, since workshop of this year is just zero phase of INTOR project.

References

- 1) J.W. Connor, R.J. Hastie, Nuclear Fusion 13 (1973) 221.
- 2) S.L. Milora, C.A. Foster, "ORNL Neutral Gas Shielding Model for Pellet-Plasma Interactions," ORNL/TM-5776, Oak Ridge National Laboratory, Oak Ridge, Tennessee (May 1977).

A.T. Mense, W.A. Houlberg, S.E. Attenberger and S.L. Milora, "Effects of Fueling Profiles on Plasma Transport," ORNL/TM-6026, Oak Ridge National Laboratory, Oak Ridge, Tennessee (April 1978).

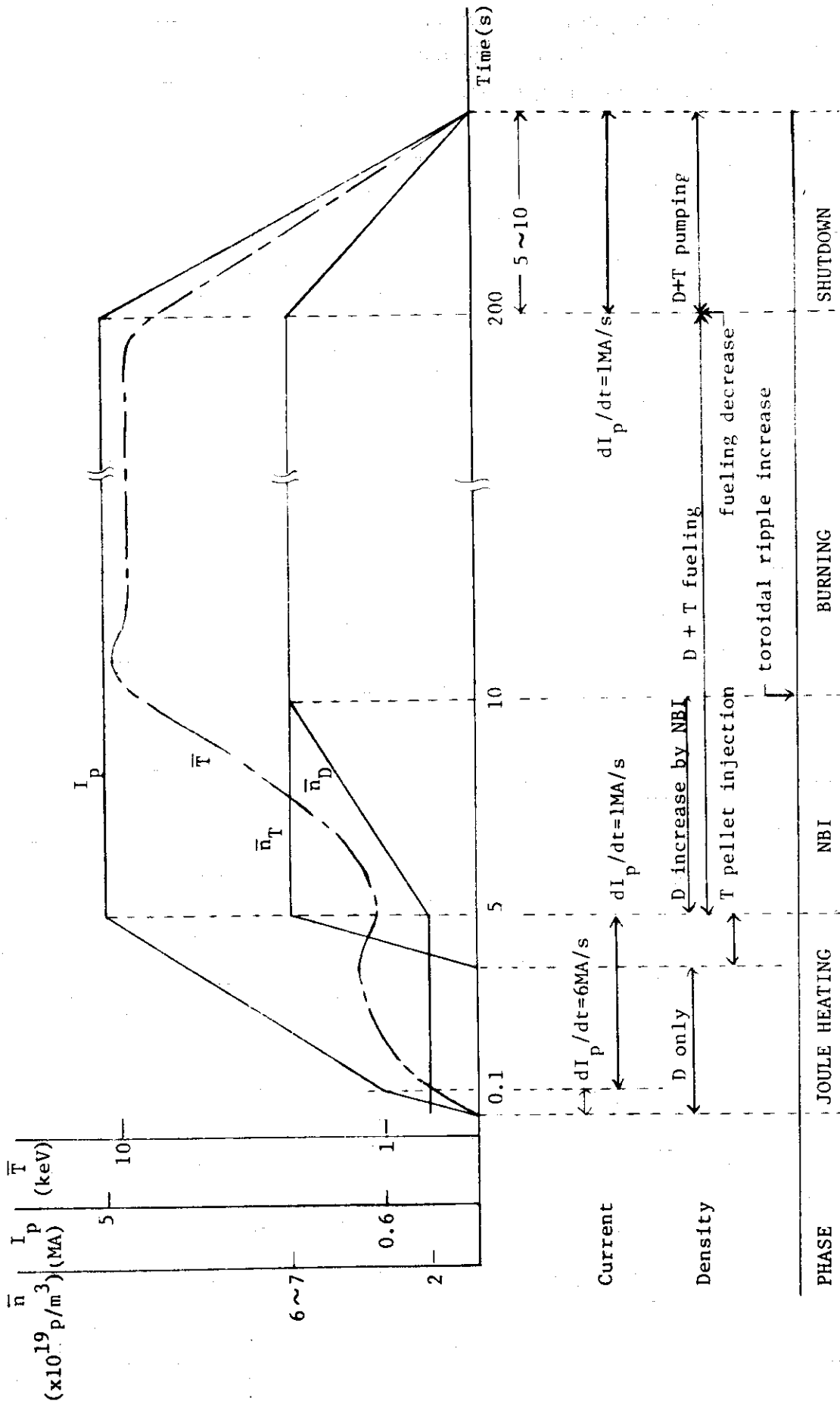


Fig. 1 Schematic drawing of the start up, burn and shut down scenario.

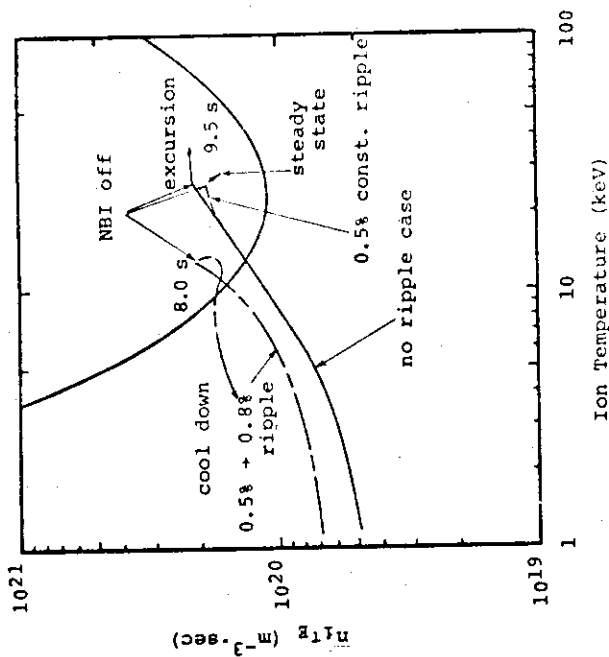


Fig. 2 Ignition approach by gas puffing for the fueling method. NBI heating power is 60 MW and is started at $t=5.0s$ and stopped at $t=9.5s$ in no ripple and 0.5% constant ripple case, and at $t=8.0s$ in case of 0.5% \rightarrow 0.8% ripple. 0.5% \rightarrow 0.8% ripple means that the toroidal ripple is raised at $t=7.5s$ from 0.5% to 0.8% with time constant of 2 sec.

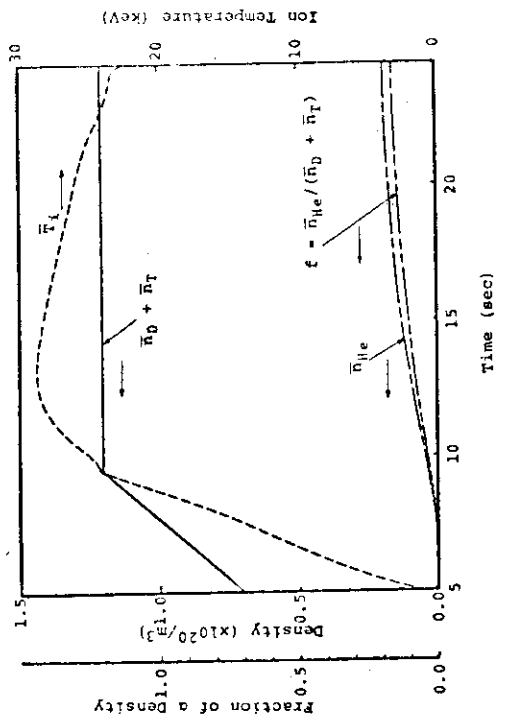


Fig. 3(a) Time evolutions of average fuel density ($\bar{n}_D + \bar{n}_T$), ion temperature \bar{T}_i , helium ash density \bar{n}_{He} and fraction of ash f in gas puffing case. Toroidal field ripple is 0.5%. Because He ash accumulates and Bremsstrahlung increases, \bar{T}_i gradually decreases after about 13 sec. \bar{T}_i can be controlled at ~ 15 keV by NBI heating time and power, and toroidal ripple.

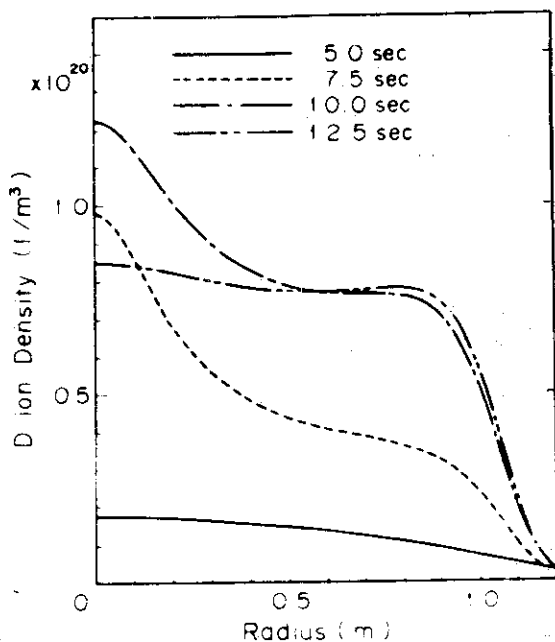


Fig. 3(b)

Time evolution of deuterium density profile of gas puffing and 100% recycling case. NBI is started at $t=5.0s$ and stopped at $t=9.5s$.

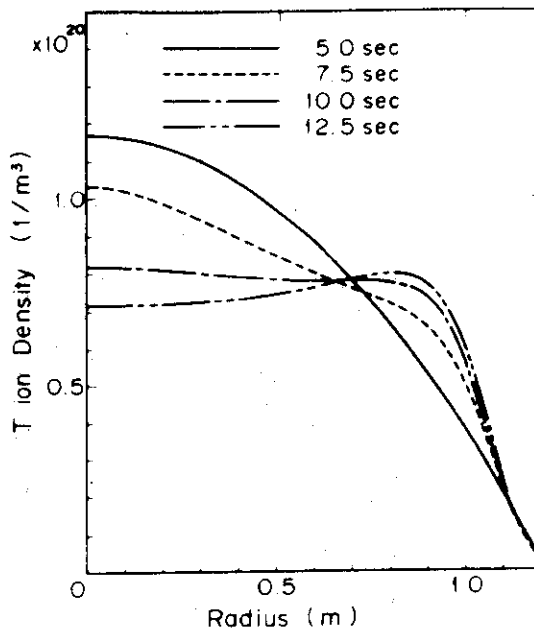


Fig. 3(c)

Time evolution of tritium density profile of gas puffing and 100% recycling case. NBI is started at $t=5.0s$ and stopped at $t=9.5s$.

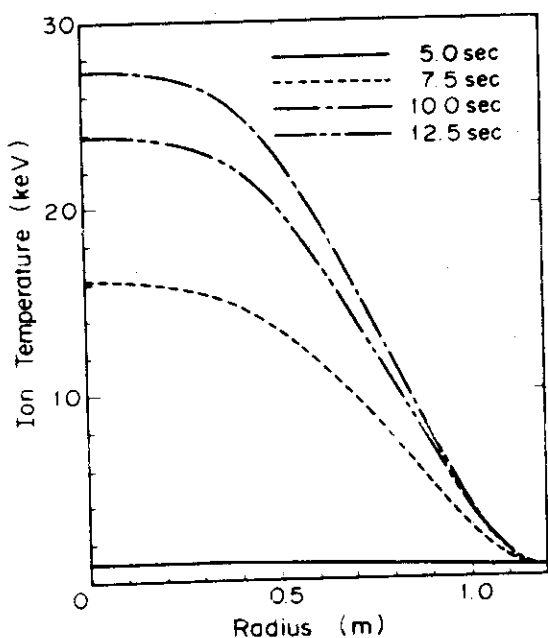


Fig. 3(d)

Time evolution of ion temperature profile of gas puffing and 100% recycling case. NBI is started at $t=5.0s$ and stopped at $t=9.5s$.

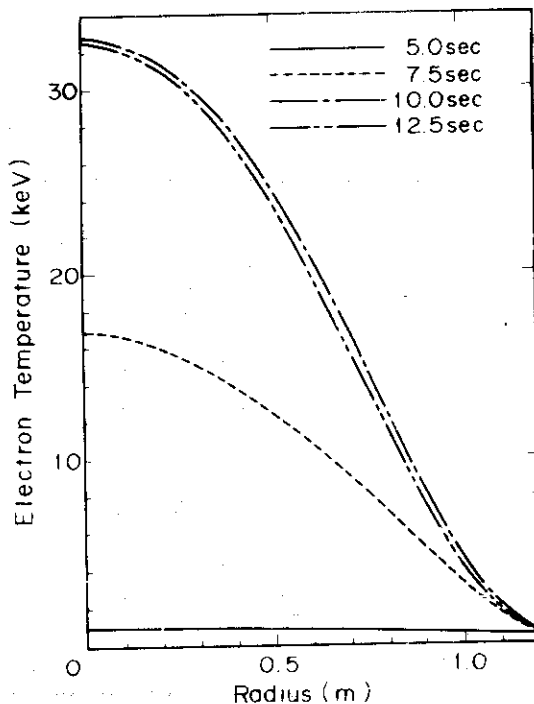


Fig. 3(e)

Time evolution of electron temperature profile of gas puffing and 100% recycling case. NBI is started at $t=5.0s$ and stopped at $t=9.5s$.

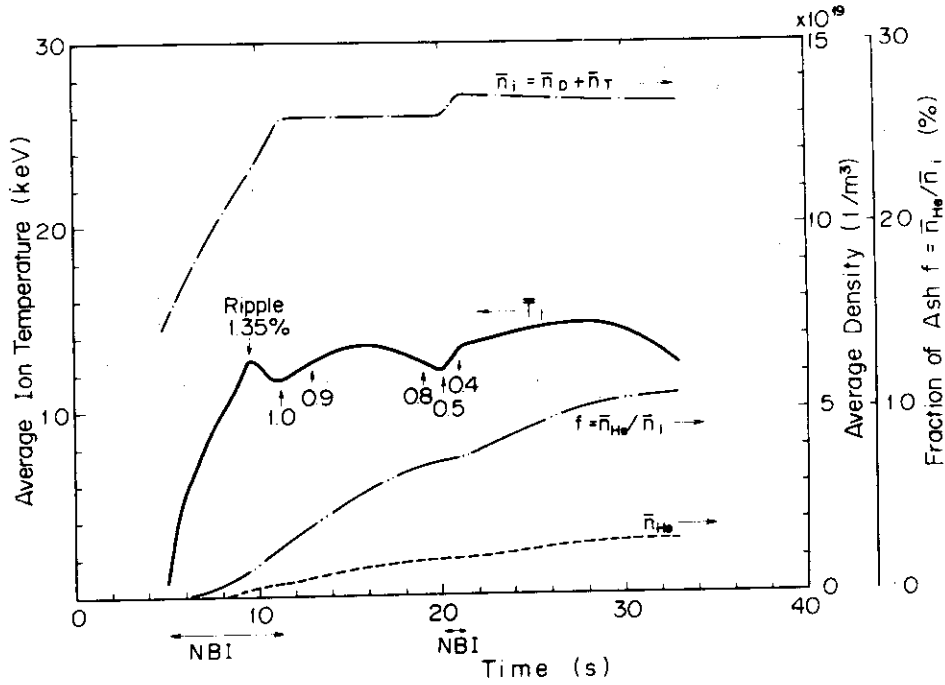


Fig. 4 Time evolutions of average ion density \bar{n}_i , average ion temperature \bar{T}_i , helium ash \bar{n}_{He} and fraction of ash f . Toroidal field ripple is adjusted to maintain \bar{T}_i at 12~14 keV. NBI is restarted at 20s for 0.5s.

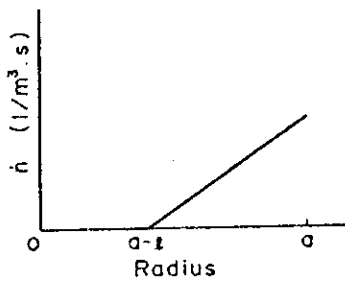


Fig. 5 Model of particle source profile by realistic pellet injection

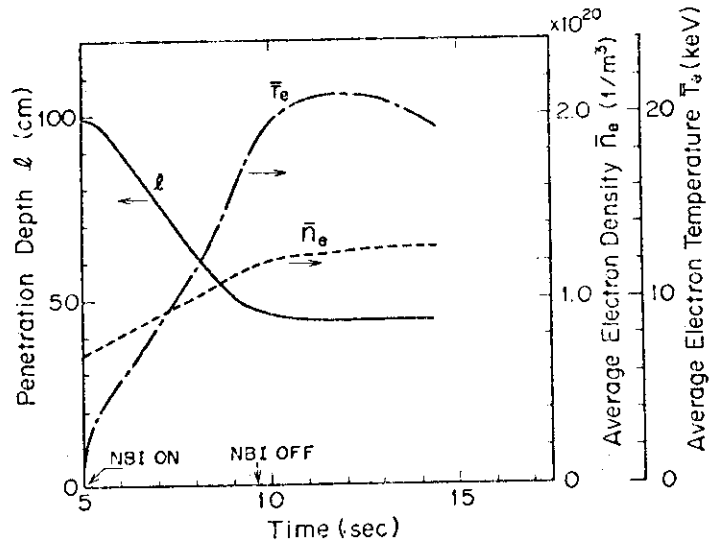


Fig. 6 Time dependence of the penetration depth l in accordance with the time evolution of the density and temperature (Fig. 5). Injection velocity and radius of pellet are assumed to be 10^4 m/s and 3 mm, respectively.

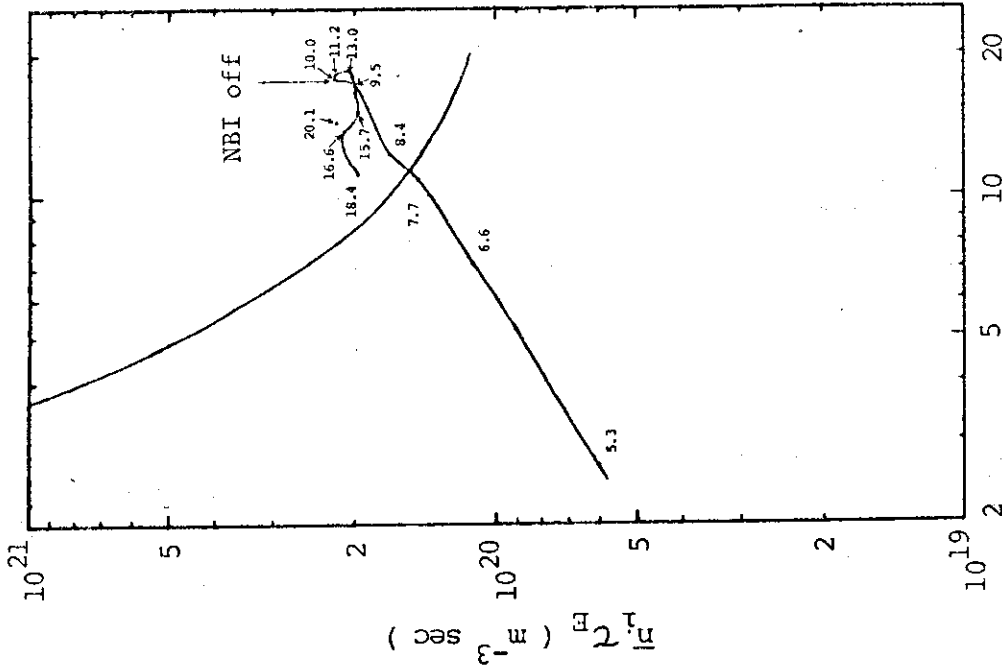


Fig. 8(a) Ignition approach by pellet injection and 50% recycling for the fueling method. NBI heating power is 50 MW with 200 keV and is started at $t=5.0s$ and stopped at $t=9.6s$. Toroidal field ripple is 0.8%.

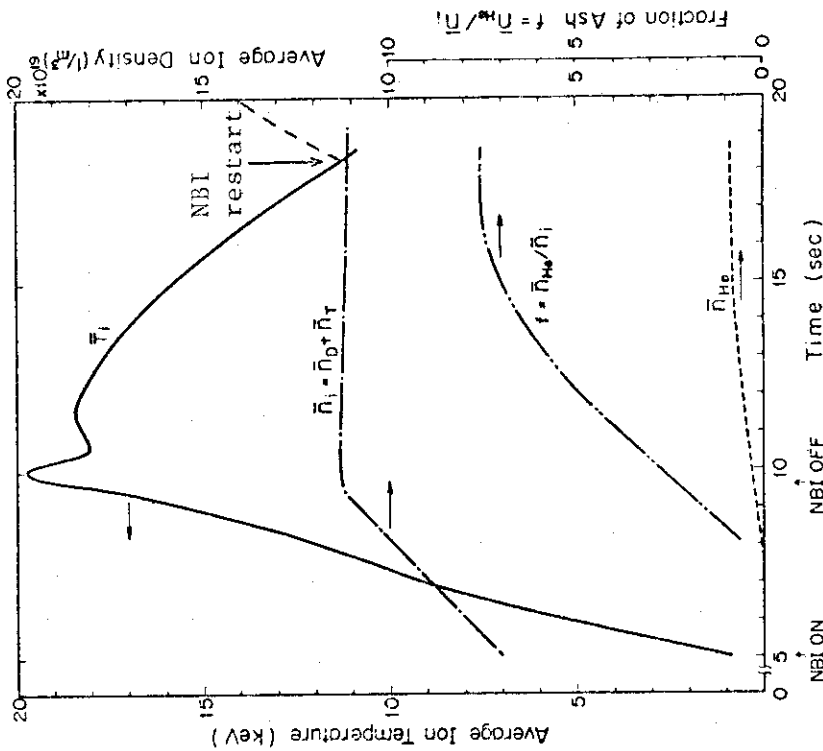


Fig. 7 Time evolutions of average ion density \bar{n}_i , ion temperature \bar{T}_i , helium ash \bar{n}_{He} and fraction of ash f . Toroidal field ripple is 0.8%. Although \bar{T}_i excessively rises up to 20 keV, this can be lowered (down to 12 ~ 13 keV) by the control of NBI heating time and power or adjusting the toroidal field ripple.

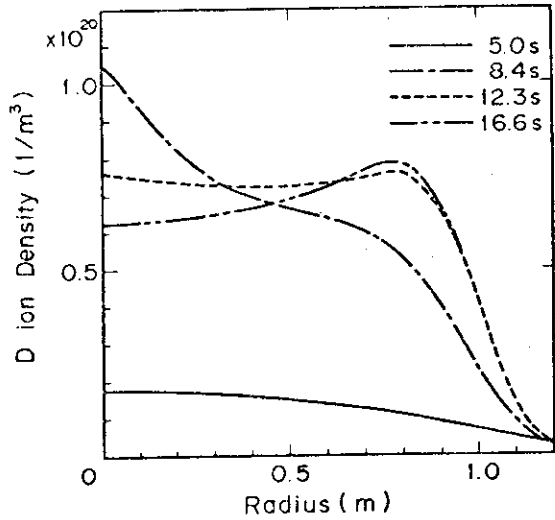


Fig. 8(b) Time evolution of deuterium density profile of pellet injection and 50% recycling case. NBI is started at $t=5.0s$ and stopped at $t=9.6s$.

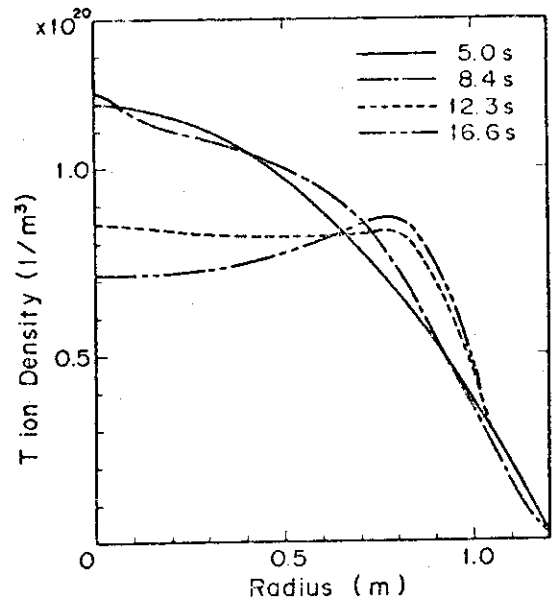


Fig. 8(c) Time evolution of tritium density profile of pellet injection and 50% recycling case. NBI is started at $t=5.0s$ and stopped at $t=9.6s$.

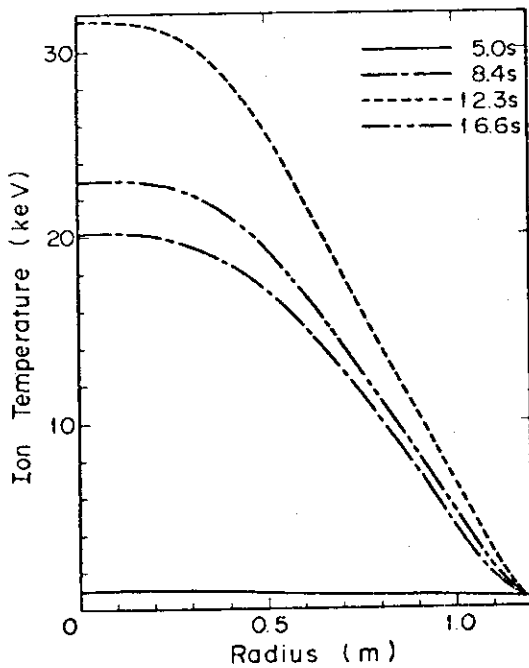


Fig. 8(d) Time evolution of ion temperature profile of pellet injection and 50% recycling case. NBI is started at $t=5.0s$ and stopped at $t=9.6s$. Toroidal field ripple is 0.8%.

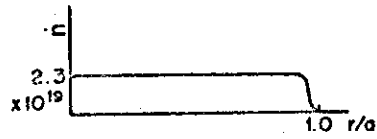


Fig. 9 Model of particle source profile by pellet injection. This source profile is employed to obtain a sharp density profile.

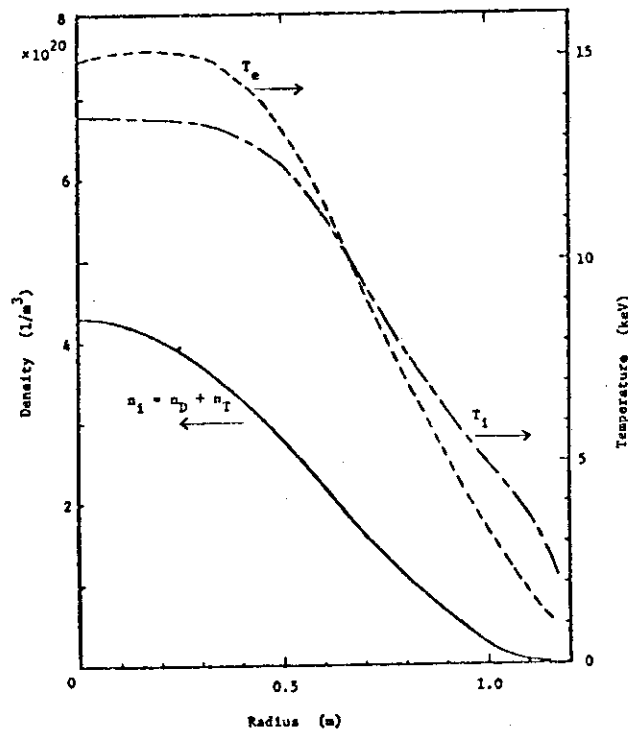


Fig. 10 Density and temperature profile in nearly steady state at $t=33s$ by pellet injection, of which source profile is given as in Fig. 8. Recycling rate is 50%. Toroidal field ripple is 1.7%.

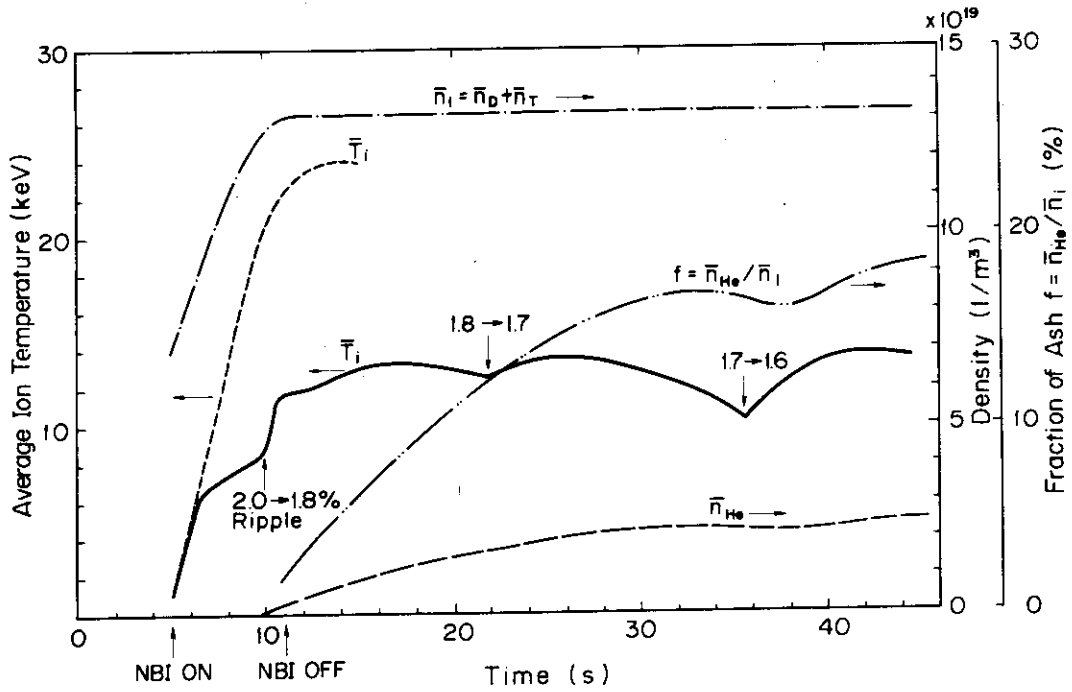


Fig. 11 Time evolutions of average ion density \bar{n}_i , ion temperature \bar{T}_i , helium ash \bar{n}_{He} and fraction of ash f in the case of sharp density profile shown in Fig. 9. The arrows on \bar{T}_i curve show that toroidal field ripple is lowered to control the plasma temperature at that moment. The accumulation time (saturation time) of helium ash is about 20 seconds. When no particular control is done, \bar{T}_i rised up to 25 keV (dotted line).

4. Heat and Particle Flux to the First Wall and the Divertor Plate

Heat and particle flux to the first wall and the divertor plate is calculated for various cases both by time dependent 1D simulation code and by steady state calculation of density profile. We include the inward flow by Ware pinch effect in particle flow and others are same as guiding model, i.e. electron thermal conductivity $\chi_e = 5 \times 10^{19}/n_e$, ion thermal conductivity $\chi_i = 3(\chi_i)_{\text{neoclas.}}$, and diffusion coefficient $D = \chi_e/12$.

The following profile of the temperature has been employed in the steady state calculation;

$$T_e(r) = T_i(r) = [T(0) - T(a)] \left[1 - \left(\frac{r}{a}\right)^4 \right]^{2.5} + T(a) .$$

Actually, however, we found that the results of the calculations are insensitive to the temperature profile. Changing the amount of the fuel source (gas puffing and/or pellet), we searched steady state solutions of density profile, which give neutron wall loading of about 1 MW/m^2 . In 1D simulation code, recycling of helium is not considered, while steady state code calculates both recycling and no recycling cases of helium. Both codes take account of the recycling of fuel particles (D,T). However, only mono-energetic neutrals are considered, so that recycling hot neutrals and cold neutrals of gas puffing cannot be treated simultaneously. Since steady state calculations do not solve energy balance equations, the solved state is not necessarily consistent with self-sustaining state from the view point of power balance.

The results are summarized in Table 1 for 1D simulation calculations, and in Table 2 for steady state calculations. Cases I-5 and I-6 give results of sharp density profile by a deep pellet injection which, however, may be unrealistic. The cases with 50 % recycling of fuel particles correspond to a simple poloidal divertor case (e.g. I-2, II-4). Gas puffing case corresponds to "Wall Lapping Plasma" (e.g. I-1, II-1-3). The case with no-recycling of both fuel particles and helium particles corresponds to an ideal divertor case (e.g. I-3, II-5).

Overall helium particle confinement time τ_{He} obtained in no helium recycling cases (e.g. I, II-2) represents the confinement time of helium ash in bulk plasma, so that the concentration of helium should be determined by this τ_{He} (i.e. $N_{\text{He}} = \tau_{\text{He}} \times S_{\alpha}$, where S_{α} is source of helium

particles). Although in most cases of 1D simulation calculations, the ash accumulation f is considerably large, this is due to excessively large source of α -particles (i.e. excessively large α -particle power P_α). In fact, when we reset P_α to the target value of 90 MW, the accumulation f^* ($f^* = f \times 90/P_\alpha$) is below 10 % in most cases. The accumulation of ash is determined by $f = N_{\text{He}}/N_i = \tau_{\text{He}} P/n_i a$ (P : neutron wall loading, a : plasma minor radius). If we assume $\tau_{\text{He}} \propto a^2$, then $f \propto a P/n_i$. Thus, if $a P$ value of a commercial reactor becomes 3 ~ 4 times larger than INTOR value, $f = 30 \sim 40$ % even though all of the helium particles diffusing from the bulk plasma are completely exhausted, so that the ash accumulation will become a serious problem unless we have margin of beta value.

Notations

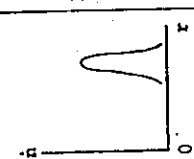
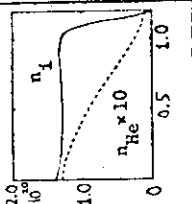
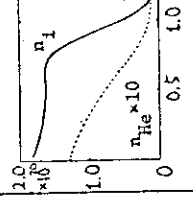
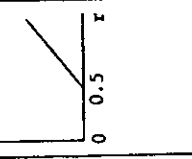
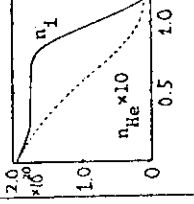
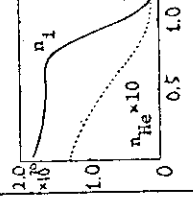
- τ_p : Over all fuel particle confinement time.
- τ_{He} : Over all helium ash confinement time.
- Γ_p : Out flux of fuel ions.
- Γ_{He} : Out flux of helium ash.
- Γ_{cx} : Out flux of neutral particles (mainly by charge exchange).
- \bar{E}_{cx} : Average energy of outflux neutral particles.
- T_{no} : Energy of neutrals entering into plasma.
- P_{cx} : Total power loss by charge exchange.
- P_r : Total power loss by radiation (including bremsstrahlung, synchrotron).
- P_α : Total α -heating power.
- P_{tr} : Total power loss by transport.
- f : Fraction of helium ash ($f = \bar{n}_{\text{He}}/\bar{n}_i$).
- f^* : Fraction of helium ash with P_α being normalized to 90 MW (i.e. $f^* = f \times 90/P_\alpha$).
- * 1 : This value cannot be obtained, since energy balance equations are not solved in steady-state calculations.
- * 2 : Not converged for helium.

Note : Power loss P_{cx} , P_r , P_α , P_{tr} are calculated for noncircular plasma (i.e., $V_p = 213 \text{ m}^3$, $S_p = 302 \text{ m}^2$).

Table 1 Particle balance calculated by 10 simulation code

	Particle source profile	Recycling of fuel particles	Density profile in nearly steady-state	Plasma parameters	Recycling of He	τ_p (sec)	τ_{He} (sec)	Γ_p ($1/m^2 s$)	Γ_{He} ($1/m^2 s$)	Γ_{CX} ($1/m^2 s$)	\bar{E}_{cx} (keV)	P_{cx} (MW)	P_x (MW)	P_a (MW)	P_{tr} (MW)	Case	
Recycling case		100 % $T_n = 500 eV$		$\bar{T}_i = 24.7$ (keV) $\bar{n}_i = 1.2 \times 10^{20}$ ($1/m^3$) $\bar{n}_{He} = 1.84 \times 10^{19}$ ($1/m^3$) $f = 15\%$ ($f^* = 7\%$) ($t = 22.6s$)	0 %	0.9	10	8.2×10^{19}	1.1×10^{18}	6.2×10^{19}	6.0	14.2	17.5	184	167	(I-1)	
				$T_i = 11.1$ $\bar{n}_i = 1.1 \times 10^{20}$ $\bar{n}_{He} = 8.3 \times 10^{18}$ $f = 7.5\%$ ($f^* = 8$) ($t = 18s$)	0 %	1.0	12	6.5×10^{19}	4.1×10^{17}	1.5×10^{19}	1.5	2.0	10.5	84	73.5	(I-2)	
				0 %	2.0×10^{20}	$T_i = 13.9$ $\bar{n}_i = 1.3 \times 10^{20}$ $\bar{n}_{He} = 1.8 \times 10^{19}$ $f = 14\%$ ($f^* = 8.5$) ($t = 23s$)	0 %	1.1	12	6.7×10^{19}	9.0×10^{17}	-	-	21	149	150	(I-3)
				50 %	4×10^{20}	$T_i = 11.7$ $\bar{n}_i = 1.3 \times 10^{20}$ $\bar{n}_{He} = 2.2 \times 10^{19}$ $f = 17\%$ ($f^* = 9$) ($t = 33s$)	0 %	2.4	15	3.4×10^{19}	8.8×10^{17}	1.0×10^{19}	3.1	2.3	38	175	133
Pellet injection case		0 %		$T_i = 11.8$ $\bar{n}_i = 1.4 \times 10^{20}$ $\bar{n}_{He} = 2.5 \times 10^{19}$ $f = 18\%$ ($f^* = 7$) ($t = 35s$)	0 %	3.8	16	2.2×10^{19}	9.4×10^{17}	-	-	53	237	178.5	(I-5)		
				$T_i = 11.8$ $\bar{n}_i = 1.4 \times 10^{20}$ $\bar{n}_{He} = 5.0 \times 10^{19}$ $f = 36\%$ ($f^* = 6.2$) ($t = 21s$)	0 %	10.0	21	8.1×10^{18}	1.4×10^{18}	-	-	-	234	520	273	(I-6)	

Table 2 Particle balance calculate by steady state calculation code

Particle source profile	Recycling of fuel particles	Density profile in nearly steady-state	Plasma parameters	Recycling of He	τ_p (sec)	τ_{He} (sec)	Γ_p ($1/m^2 s$)	Γ_{He} ($1/m^2 s$)	Γ_{CX} ($1/m^2 s$)	\bar{E}_{CX} (keV)	P_{CX} (MW)	P_r (MW)	P_α (MW)	P_{tr} (MW)	Case
 <p>Recycling case</p>	100 %		$\bar{T}_i = 10.3$ (keV) $\bar{n}_i = 1.15 \times 10^{20}$ ($1/m^3$) $\bar{n}_{He} = 5.1 \times 10^{18}$ ($1/m^3$) $f = 4.4\%$ ($f^* = 4.6$)	0.89	0.31	1.25	2.3×10^{20}	2.5×10^{18}	7.9×10^{19}	0.7	4.1	6.9	87	-	(II-1)
	50 %	similar to above profile	$\bar{T}_i = 9.9$ $\bar{n}_i = 1.19 \times 10^{20}$ $\bar{n}_{He} = 5.01 \times 10^{18}$ $f = 4.2$ ($f^* = 4.4$)	0	0.24	8.8	3.0×10^{20}	3.4×10^{17}	8.2×10^{19}	0.3	1.9	7.1	80	-	(II-2)
	0 %		$\bar{T}_i = 9.8$ $\bar{n}_i = 1.27 \times 10^{20}$ $f = 6.9$ ($f^* = 6.6$)	0.63	0.21	∅	3.7×10^{20}		1.43×10^{20}	0.1	1.0	9.2	93	-	(II-3)
 <p>Pellet injection case</p>	50 %		$\bar{T}_i = 10.2$ $\bar{n}_i = 1.2 \times 10^{20}$ $\bar{n}_{He} = 5.9 \times 10^{18}$ $f = 4.9$ ($f^* = 4.1$)	0.55	0.65	3.7	1.12×10^{20}	9.6×10^{20}	8.2×10^{20}	1.0	1.8	9	108	-	(II-4)
	0 %		$\bar{T}_i = 9.9$ $\bar{n}_i = 1.05 \times 10^{20}$ $\bar{n}_{He} = 4.0 \times 10^{18}$ $f = 3.8$ ($f^* = 4.3$)	0.58	0.76	3.2	8.22×10^{19}	7.6×10^{17}	-	-	-	6.9	80	-	(II-5)

5. Effects of Impurities on INTOR Plasma

5.1 Model of Impurity Transport

(1) Impurity transport model

Radial diffusion of impurity ions across the minor radius, observed in today's experiment, seems to be well described by a neoclassical diffusion superposed by the anomalous diffusion for protons. In particular this transport model explains the following experimental results.

1) Impurity transport

The confinement time for low-Z impurity ions is the order of that for protons¹⁾.

Comparison of experimental results and the computational results of the radial diffusion of carbon ions have been made for the DIVA plasma. Figure 1(a) shows the steady state and Fig. 2(a) (b) show the increment with the methane injection of CIII and CV line emissions in low-density discharge ($\bar{n}_e = 1 \times 10^{13} \text{ cm}^{-3}$). In this discharge, intensity of CV 2271A line corresponds the amount of carbon accumulation in the plasma center, and CIII 2297A line the intensity of recycling flux in the plasma outer edge region. The transient and steady state of radial profiles of these line emissions were compared with calculations by using a transient code which includes diffusion, ionization, recombination and recycling processes (Fig. 1(b) and Fig. 2(b), (c)). The radial diffusion of the carbon ions across the whole minor radius is well described by assuming perfect recycling at the gold-plated shell surface and by using neoclassical diffusion superposed by anomalous proton diffusion.

2) Shielding of impurity

Roughly 80 % of the impurity flux entering the plasma is shielded in the plasma outer edge region even in the discharge without divertor²⁾. Figure 3(a) shows the time evolution of the line integral (across the minor diameter) of proton signals of AlXI 550A with an aluminum injection of the same amount by using laser blow-off technique for discharges with and without divertor. Figure 3(b) shows the radial profiles of the corresponding volume

emission 3 msec after injection. Solid lines indicate a discharge with and dotted ones a discharge without divertor.

For diverted discharges, the accumulation of injected aluminum is reduced by a factor of 3 to 4 compared to non-diverted discharges. Furthermore it appears that 80 % of the injected aluminum is shielded even in the non-diverted discharge, i.e. only 20 % of the injected aluminum accumulates in the discharge. We have investigated the trapping rate of the injected impurity by employing the present impurity transport model. In the present calculation, we use average Z calculated for coronal equilibrium state.

Figure 4 shows the time development of total aluminum ions trapped in the discharge for the neutral aluminum injection with 1.5 msec duration. Case (a) shows the computational result. It indicates the maximum trapping rate of 35 % at the time just after the injection. The rest of the injected impurity ions is lost towards the wall due to anomalous diffusion process which spreads the radial profile of aluminum ions. This effect is clarified by the similar calculation with the increased anomalous diffusion coefficient. The case (b) presents the impurity accumulation when the anomalous diffusion coefficient is doubled. In this case the outward flux towards the wall due to anomalous diffusion is increased, thereby the accumulation is reduced to 18 %.

(2) Expected impurity density profiles in INTOR

The present transport model predicts that the increase of energy and particle confinement time with increasing the electron density, the lifetime of metal impurity ions in the plasma increases, because the outward diffusion due to anomalous process is weakened and the inward diffusion due to collisional process is strengthened. As a result, in this situation, more severe control of metal impurity flux will be needed in a future tokamak device operating with long energy confinement time. Therefore, although there are many uncertainties especially for the transport process in trapped ion regime and the effects by the presence of injected fast ions or MHD activity in high temperature plasmas, it seems that the impurity ions will have peaked profile in high plasma density operation planned in INTOR.

(3) Useful additional experiment in this area

The following experimental research will be useful for the assessment for impurity accumulation and impurity control in INTOR:

- 1) impurity transport study in high density and/or high temperature discharges obtained with high power neutral beam heating; JTF-2, JT-60.
- 2) edge plasma control with high power heating,
 - a) edge cooling with gas puffing or low-Z impurity to reduce wall sputtering^{3),4)}; DIVA with carbon wall (without auxiliary heating), JFT-2, JT-60 (low-Z impurity injection),
 - b) magnetic limiter; JT-60.

References

- 1) M. Nagami et al, Nucl. Fusion 18 (1978) 1217.
- 2) M. Nagami et al, Nucl. Fusion 18 (1978) 1347.
- 3) Y. Shimomura et al, Nucl. Fusion 17 (1977) 626.
- 4) K. Ohasa et al, Nucl. Fusion 18 (1978) 872.

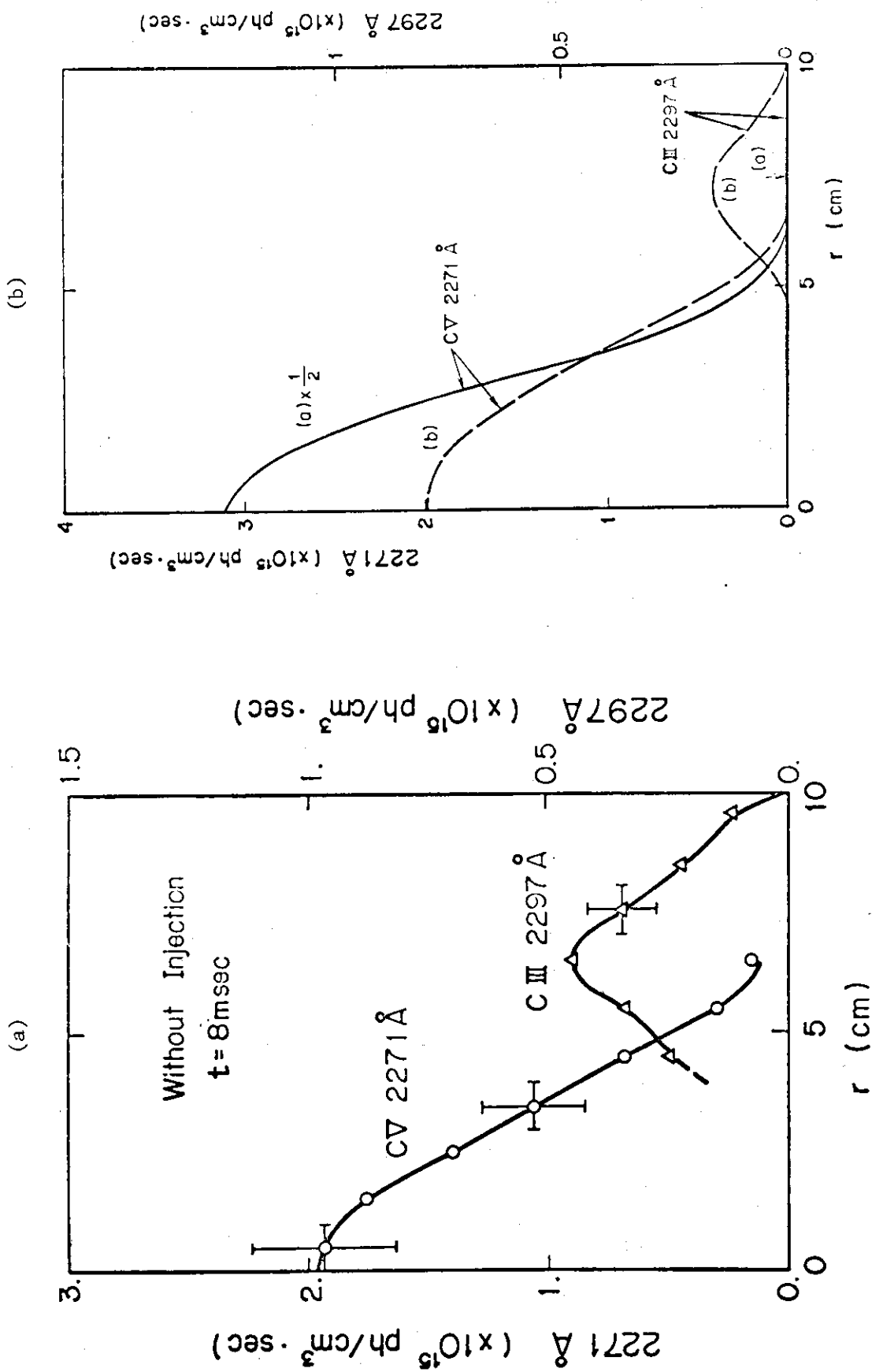


Fig. 1(a) Abel-inverted volume emissions of CIII 2297 Å and CV 2271 Å in the stationary state. Fig. 1(b) Computational results (a); neoclassical, (b); neoclassical + anomalous.

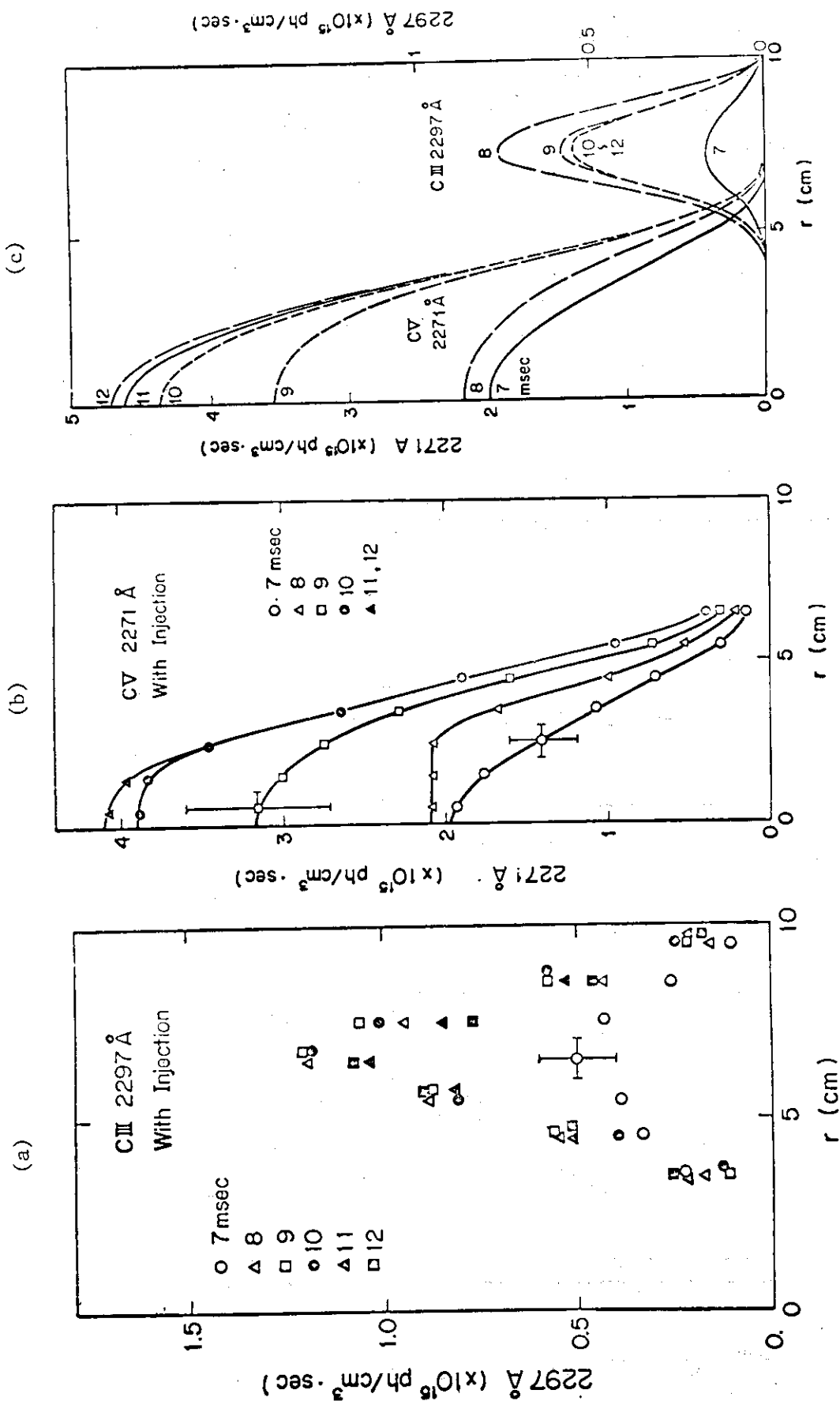


Fig. 2(a) Transient radial diffusion of carbon ions after the pulsed methane injection
 (b), (c) Computational results for the present transport model.

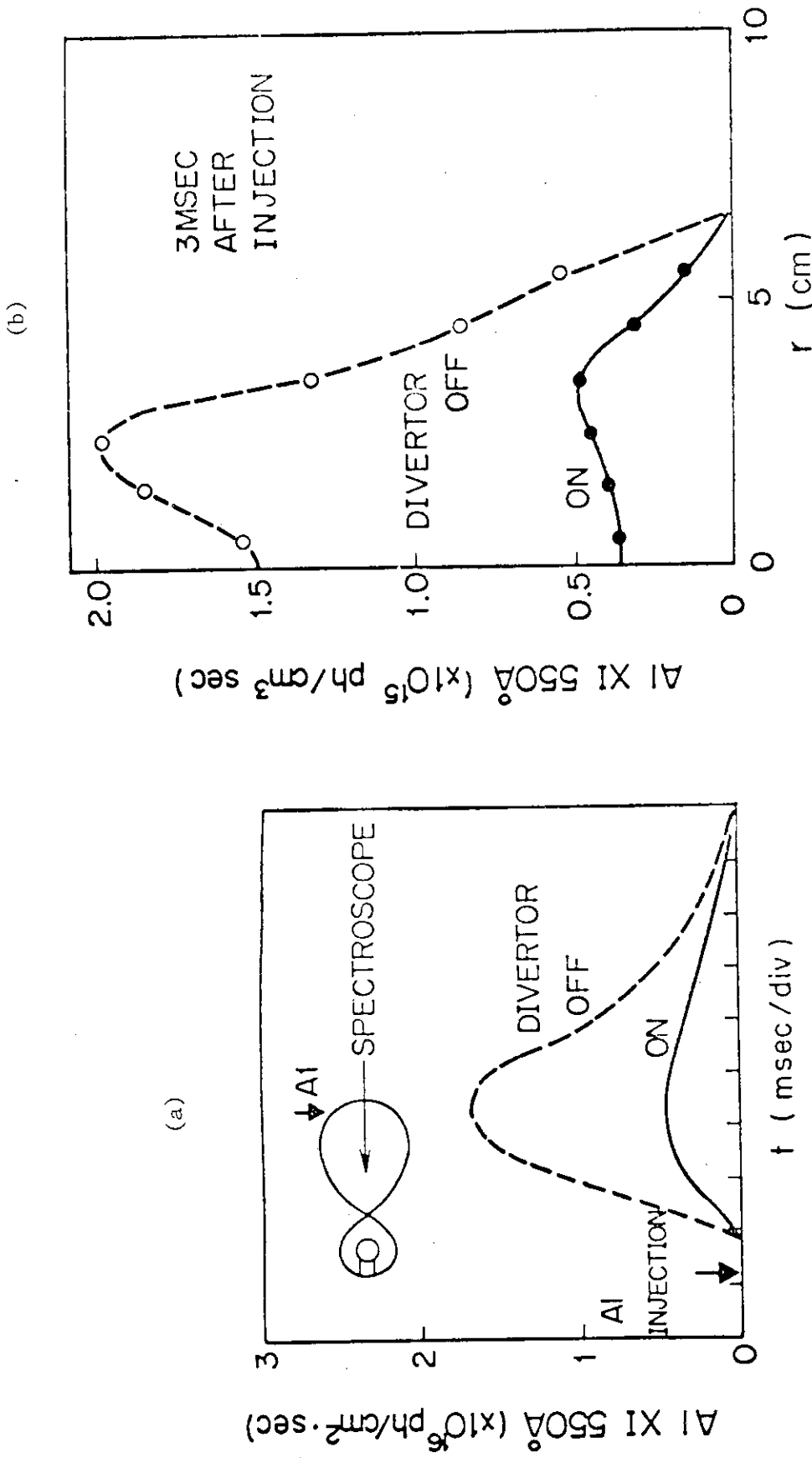


Fig. 3(a) Time development of the line integrated emissivity of Al XI 550 Å with aluminum injection.

(b) Abel-inverted volume emission of Al XI 550 Å 3 msec after the injection. Accumulation of injected aluminum ions in the central plasma region is reduced by a factor of 3 to 4 by the divertor. Roughly 80 % of the injected aluminum is shielded even in non-diverted discharge.

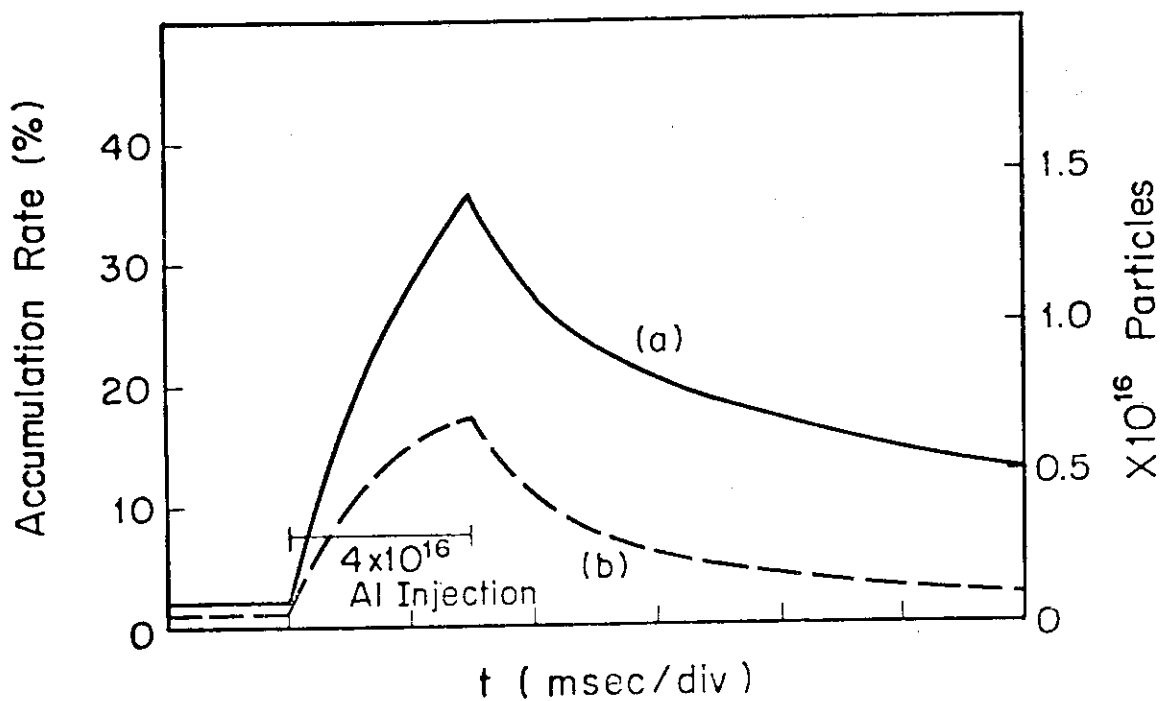


Fig. 4 Computational result of the time developments of trapped aluminum ions in the discharge for a neutral aluminum injection of 4×10^{16} particles; (a) present transport model, (b) anomalous diffusion coefficient used in case (a) is doubled.

5.2 Impurity Effect on INTOR Plasma

Undoubtedly heavy metallic impurities such as Mo, W, Ta, etc. will deteriorate the plasma by center-cooling due to large excitation losses, and their permissible concentration might be the order of 0.01 % of the plasma density. It is not so obvious, however, whether we have similar conclusion in the cases of light metallic impurities such as Fe and Ti. On the other hand in current tokamak plasmas, light impurities such as C and O have played a role of edge-cooling and strong interaction of the plasma with the limiter has been suppressed. Therefore electron temperature distribution is sharp due to edge-cooling by light impurities and consequently the energy confinement time τ_E is short, but fatal contamination due to metallic impurities has been avoided. This effect on τ_E is shown in Fig. 1 where the influence of light impurities is implicitly reflected on a_{half} as $\tau_E = (1.5 - 2)\sqrt{q_a} \times 10^{-20} \bar{n}_e a_{\text{half}}^2$ (s). Above empirical τ_E gives electron energy confinement time τ_{Ee} approximately. In large tokamak plasma with the temperature of above multi-keV, $\tau_E \approx \tau_{Ee} (1 + \bar{T}_i/\bar{T}_e) \approx 2\tau_{Ee}$, since $\bar{T}_i \approx \bar{T}_e$. Therefore for INTOR, a_{half} should be larger than 0.6a (i.e. parabolic-like distribution) to achieve a required τ_E of above 1.5 s for ignition. However, it has not been made clear what a role light impurities and light metallic impurities will play in large tokamaks, i.e. center-cooling or edge-cooling.

We calculate C, O and Fe radiation including impurity diffusion. Results show that the impurity diffusion affects the total impurity radiation. The much reduction of charge state from that in coronal equilibrium due to impurity increases the impurity radiation from tokamak plasmas. This effect is conspicuous near the plasma edge, where the impurity charge state is under the ionizing phase balanced by the impurity diffusion. In the estimation of impurity radiation from a given plasma parameter, total impurity radiation is influenced significantly by the radial distribution of the electron temperature and density. In Case A (where temperature and its gradient are low and moderate in the boundary region, but high and steep in the central region), significant amount of partially ionized impurity ions is distributed in the boundary region and excitation loss in this region due to those ions is much larger than bremsstrahlung loss from the center region (see Table 1, and Fig. 2-(a) as the case of O). On the other hand in Case B (parabolic distribution case), most of impurity ions, which are highly-

ionized, are distributed in the central region, and consequently bremsstrahlung loss becomes large and excitation loss in the boundary region becomes extremely small (see Table 1, and Figs. 2-(b), 3, as the case of O and Fe, respectively).

Guiding parameters of INTOR give mean ionic charge of the plasma $Z_{\text{eff}} = 1.5$. However, results calculated show it is possible that in Case A, considerable amount of light impurities (e.g. 6 ~ 8 % of carbon) heavily deteriorate the hot core plasma. Although $Z_{\text{eff}} = 1.7 \sim 1.8$ in this case, most of impurity ions distribute in the cold region surrounding the hot core so that ion density $n_i \sim 0.9n_e$ in the hot core, and bremsstrahlung loss increases to 17 ~ 21 MW at most but excitation and ionization losses in the boundary region extremely increases to 29 ~ 45 MW. In such plasma most of energy losses carried by plasma particles from the hot core is converted into radiation in the boundary region and consequently edge temperature should be considerably low.

Above results are derived from temperature-screening effect, i.e. strong inward diffusion of impurities is suppressed by temperature gradient of plasma ions. However, when temperature-screening effect is neglected, strong edge-cooling by C impurity cannot be expected even in Case A, as shown in Fig. 4. In this case, large minor radius of 1.4 - 1.5 m might be required to meet required τ_E for ignition.

Therefore, when we can expect temperature-screening effect and have 1.0 - 1.5 % margin of β value, we can allow 5 - 10 % light impurity concentration and expect sufficient edge-cooling by light impurities without decrease of fusion power. In such plasmas, requirement for impurity control will be extremely mitigated. However, these conclusions strongly depend on density and temperature distributions of the plasma, as well as impurity diffusion. Therefore, it is necessary to further investigate about the transport models for the plasma and impurities.

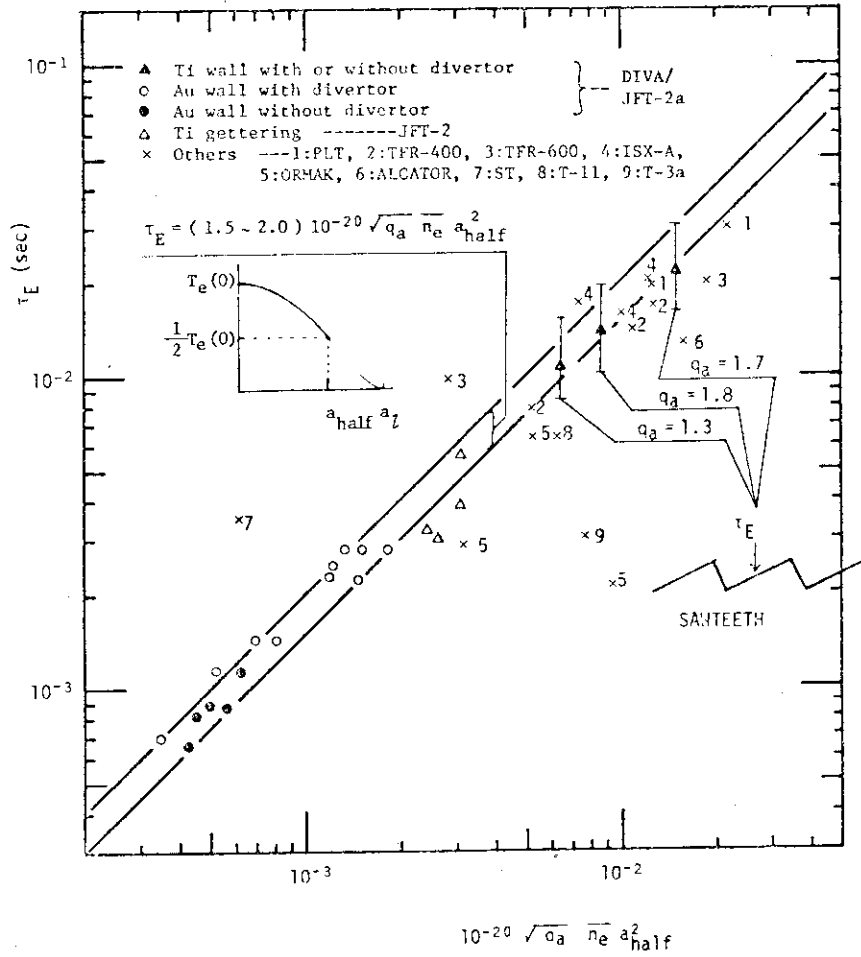


Fig. 1 Empirical $\sqrt{q_a} \bar{n}_e a_{half}^2$ scaling law of energy confinement time.

Table 1. Energy losses caused by impurities from the given deuterium plasma, where C_z : mean effective ionic charge, \bar{n}_e : mean electron density, P_{br} : total bremsstrahlung loss, P_{ex} : total excitation loss, P_i : total ionization loss. These losses are calculated in the circular plasma with 1.2 m minor radius, 5 m major radius and 242 m³ volume, and are multiplied by 1.5 to estimate those in the elongated plasma with 1.5 elongation ratio and 300 m³ volume.

Impurities	Carbon				Oxygen			Iron
	2	4	6	8	1	2	3	
C_z (%)	2	4	6	8	1	2	3	0.1
Z_{eff}	1.3	1.5	1.7 [2.2]	1.8	1.2 (1.4)#	1.4	1.6	(1.3)#
n_e ($\times 10^{20}/m^3$)	1.3	1.5	1.5 [1.6]	1.7	1.3 (1.3)#	1.3	1.4	(1.2)#
P_{br} (MW)	10.0	13.7	17.4 [29.7]	21.3	9.4 (11.1)#	11.7	14.1	(9.2)#
P_{ex} (MW)	4.2	10.9	20.2 [3.7]	31.8	13.0 (0.3)#	34.4	63.3	(3.7)#
P_i (MW)	2.4	5.4	9.0 [8.9]	13.3	2.5 (2.9)#	5.7	9.3	(7.0)#

Plasma parameters are;

ion density $n(r) = 2\bar{n}_i \{ (1 - (r/r_p)^2) \} + 5 \times 10^{18}$

electron and ion temperature $T_e(r) = T_i(r)$

Case A: $T_e(r) = 2.4\bar{T} \{ 1 - (r/r_p)^4 \}^{2.5}$ at $0 \leq r \leq 1.1$ m
 $= 50$ eV at $1.1 \leq r \leq 1.2$ m

Case B: $T_e(r) = 2\bar{T} \{ 1 - (r/r_p)^2 \}$ at $0 \leq r < 1.2$ m
 $()\# = 50$ eV at $r = 1.2$ m

where $\bar{T}_e = \bar{T}_i = 10$ keV, $\bar{n}_i = 1.2 \times 10^{20}$ 1/m³. We assume that outward diffusion is anomalous (an anomalous factor of 10 for classical diffusion coefficient is employed) and inward diffusion is classical. The case without temperature-screening effect, i.e. where ion temperature gradient effect is neglected in the term of impurity inward diffusion, is also shown in this Table with a brace for 6 % carbon impurities of Case A.

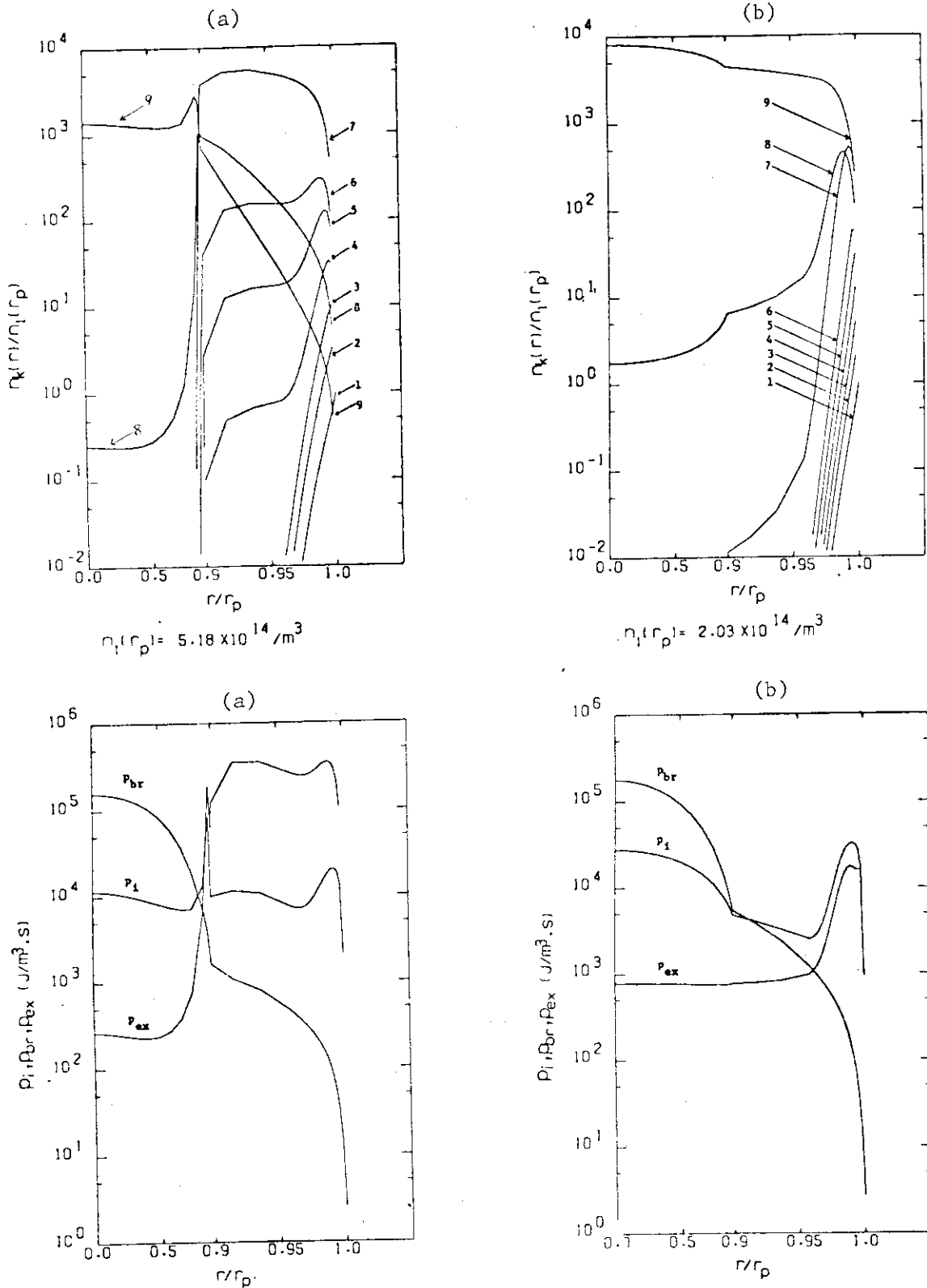


Fig. 2 Radial density distribution of 1 % of oxygen impurities normalized by the boundary value of neutral oxygen density and related energy losses, in (a): Case A, and (b): Case B. Note that the scale of the normalized radius shown in the abscissa is changed at 0.9.

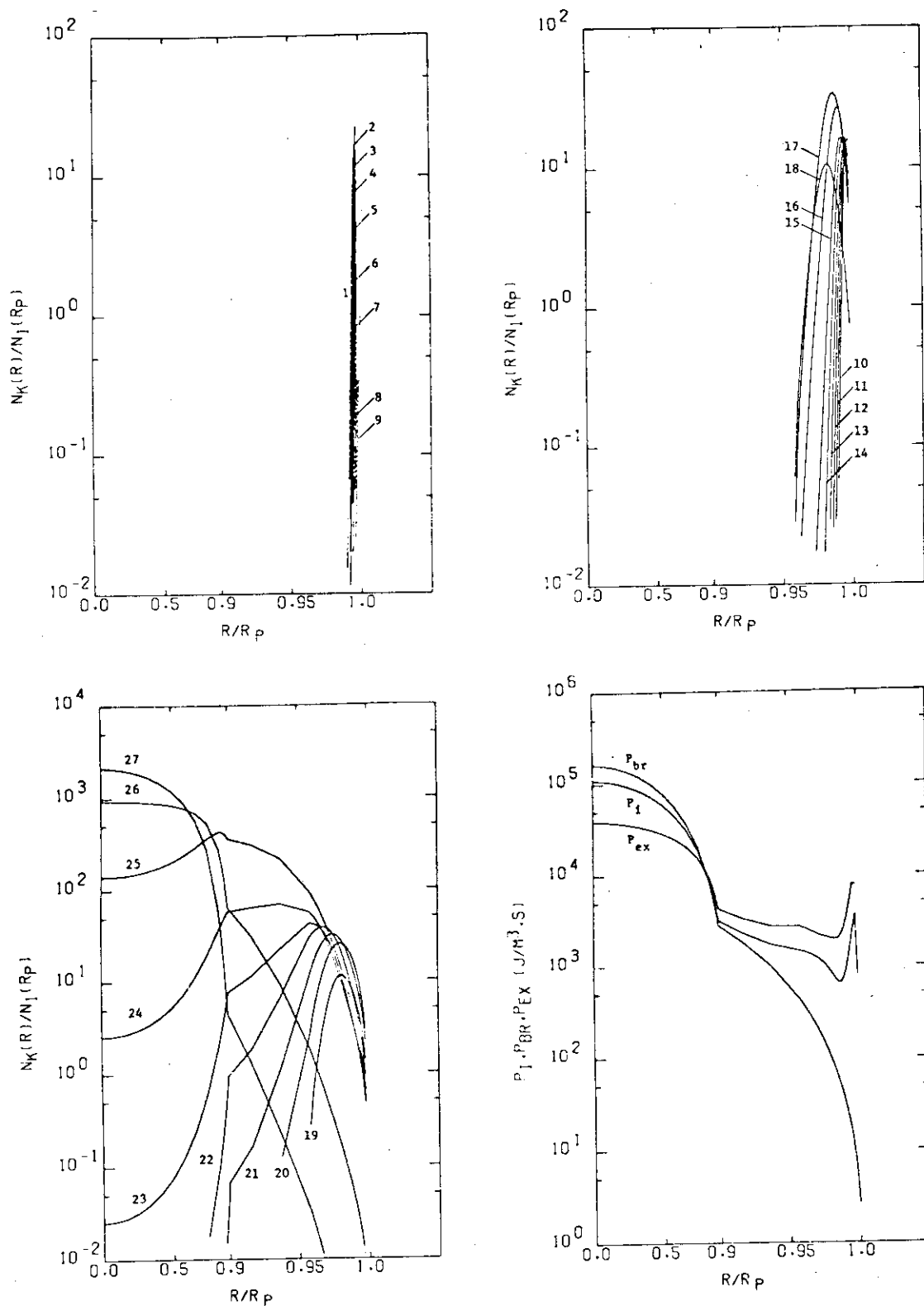


Fig. 3 Radial density distribution of 0.1 % of Fe impurities normalized by the boundary value of neutral Fe density and related energy losses in Case B. Note that the scale of the normalized radius shown in the abscissa is changed at 0.9.

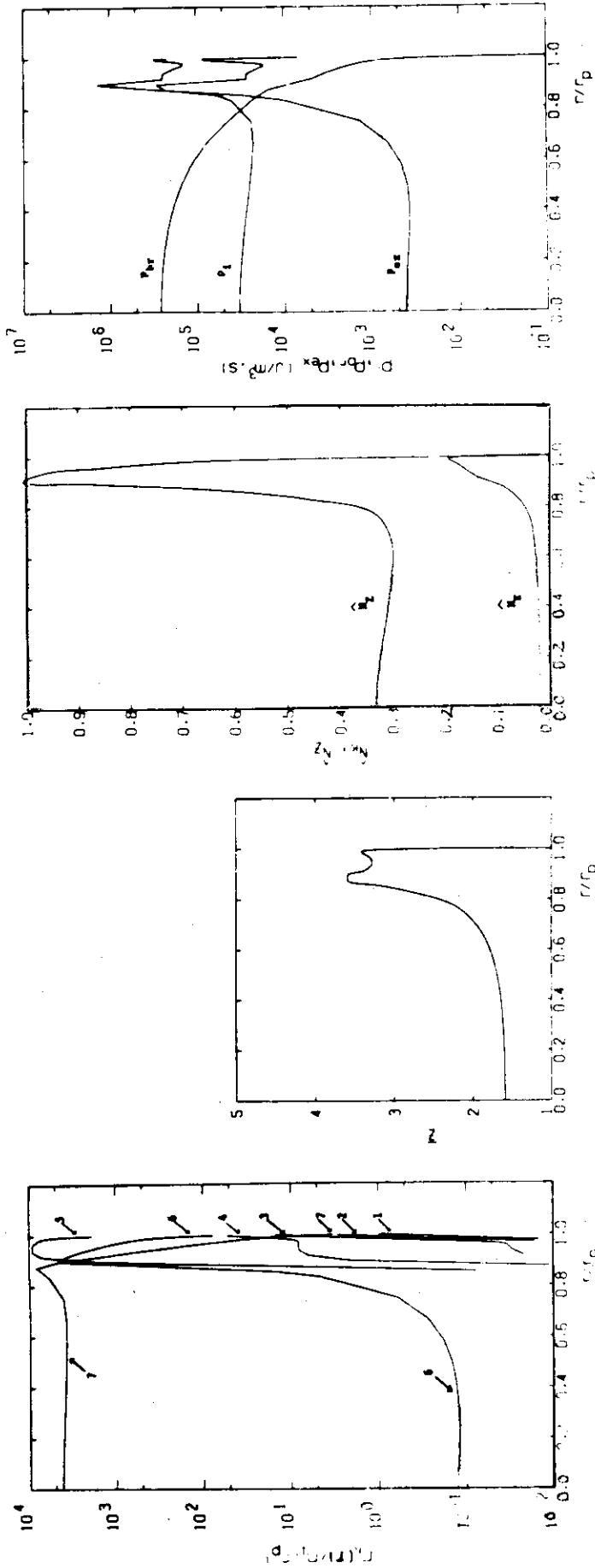


Fig. 4-(a) Calculation for 6 % carbon impurities of Case A with temperature-screening effect.

1): radial density distribution of carbon impurities normalized by the boundary value of neutral carbon density; 2): mean effective ionic charge profile;

3): normalized total impurity density profiles, $N_k = \sum_{k=2}^7 n_k(r)/n_e(r)$,

$N_z = \sum_{k=2}^7 n_k(r) / \max_{k=2}^7 n_k(r)$; 4): radial distribution of related energy losses,

P_{br} : bremsstrahlung loss, P_{ex} : excitation loss, P_i : ionization loss.

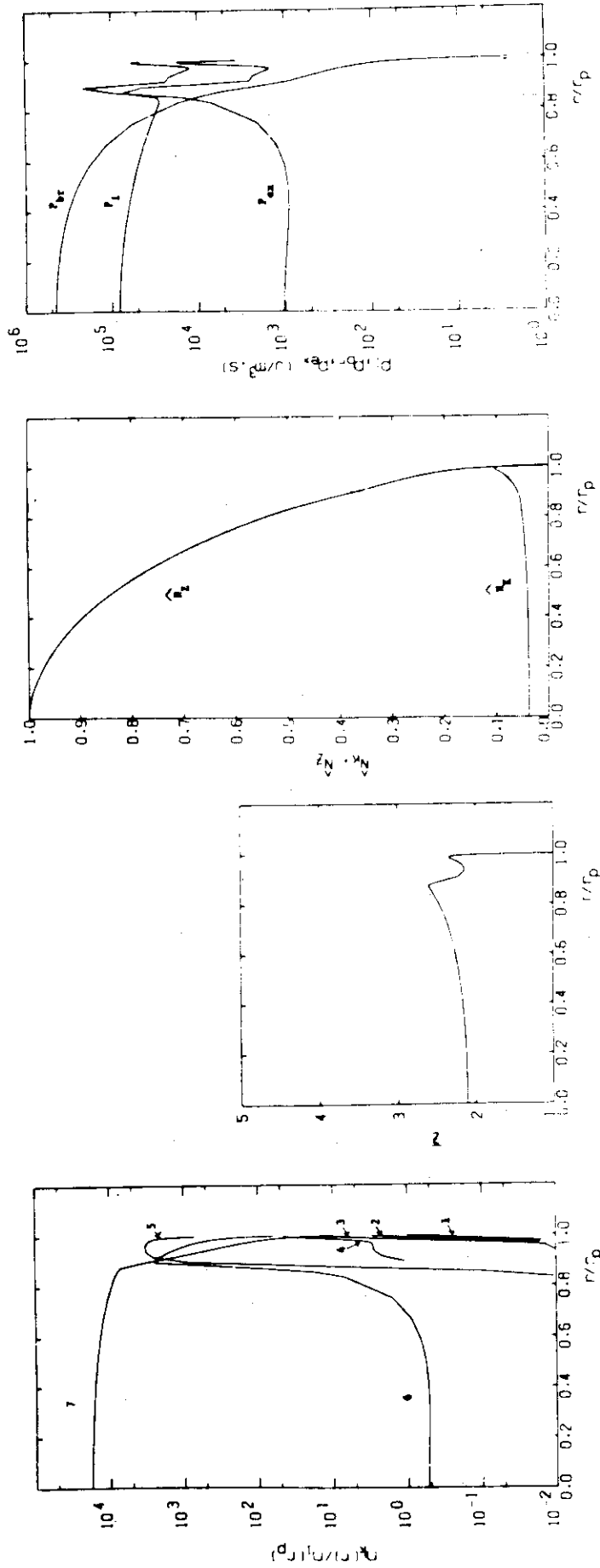


Fig. 4-(b) Calculation for 6 % carbon impurities of Case A without temperature-screening effect. Otherwise similar to Fig. 4-(a).

6. Estimation of Allowable Field Ripple

6.1 Effects of Field Ripple on Ion Thermal Conductivity and Loss of Reacting Tail

(1) Conclusion and summary

- (1) Amplitude of field ripple must be less than 0.005 in the hot core plasma region to avoid a substantial reduction of the thermonuclear fusion reaction and alpha particle heating.
- (2) The effect of field ripple on ion thermal conductivity χ_i is not so crucial, when the ripple is suppressed below 0.5 % in the hot core plasma region.
- (3) The effect of field ripple on the ripple loss of energetic particles from NBI can be suppressed by inclining the beam path by $10^\circ \sim 15^\circ$ against the normal of the magnetic field line.

Detailed discussions are presented in the followings.

(2) Effect of field ripple on ion thermal conductivity χ_i

(1) Introduction

The magnetic field ripple due to the discrete nature of the toroidal field coils in a Tokamak leads to additional diffusion flux of particle and heat such as ripple diffusion^{1),2)} and banana drift diffusion^{3),4)}.

(2) Model and ripple diffusion

For hot-ion energies such that

$$v_{Ti} \ll v_\alpha \ll v_e, \quad (1)$$

the linearized collision term becomes⁵⁾

$$C^\alpha \approx \frac{1}{\tau_s} \left[\frac{1}{v^2} \frac{\partial}{\partial v} \{ (v_c^3 + v^3) f_\alpha \} + \frac{m_i}{2m_\alpha} \frac{v_c^3}{v^3} \frac{\partial}{\partial \eta} \{ (1-\eta^2) \frac{\partial f_\alpha}{\partial \eta} \} \right] + \frac{1}{2\tau_s} \frac{m_i}{m_\alpha} \left(\frac{2T_i}{m_i} \right)^2 \frac{1}{v^2} \left[\left\{ \frac{v_c^3}{v^3} + \frac{m_i}{m_e} \left(\frac{T_e}{T_i} \right)^2 \right\} \frac{\partial f_\alpha}{\partial v} \right] \quad (2)$$

where

$$v_c^3 \equiv \frac{3\sqrt{\pi}}{4} \frac{m_e}{m_i} \left(\frac{2T_e}{m_e} \right)^{3/2},$$

$$\tau_s \equiv \frac{3T_e^{3/2} \sqrt{m_e}}{4\sqrt{2\pi} e_\alpha^2 e^2 n \ln \Lambda} \frac{m_\alpha}{m_e},$$

and

$$\eta = \frac{v_{//}}{v}$$

and we assume $e_i = -e_e = e$. The last term of Eq. (2) is usually small and can be neglected.

Magnetic field strength of a tokamak with field ripple is approximately

$$B \approx B_0 \{1 - \epsilon \cos \theta - \delta(r) \cos N\psi\}. \quad (3)$$

Diffusion coefficient D^r and ion thermal conductivity coefficient χ_i^r in this ripple field is given, by^{1),2)}

$$D^r \sim 4.8 \frac{G(\alpha) \delta^{3/2}}{v_e} \left(\frac{T}{eBR}\right)^2 \quad (4)$$

and

$$\chi_i^r \sim 46.5 \frac{G(\alpha) \delta^{3/2}}{v_{ii}} \left(\frac{T}{eBR}\right)^2 n, \quad (5)$$

where $G(\alpha)$ is a numerical factor due to a toroidal effect and its asymptotic value ($\alpha > 1$) is given by Connor and Hastie²⁾ as

$$G(\alpha) \approx \frac{0.02}{\alpha^3}$$

where

$$\alpha \equiv \frac{\epsilon}{Nq\delta}$$

and N is the number of the toroidal field coil.

For energy range

$$v_1 < v < v_2, \quad (6)$$

where

$$v_1 = \left\{ \frac{R v_c^3}{\delta N \tau_s} \right\}^{1/4}$$

and

$$v_2 = \left\{ \frac{R^2 a^2 \omega_{ci}^2 v_c^6}{G(\alpha) \delta^{3/2} \tau_s^2} \right\}^{1/10}$$

we estimate the loss rate of energetic ion by the ripple diffusion process from Eq. (2) and Eq. (3) as

$$\tau_{\text{loss}} = \frac{a^2}{2\tau_s \left(\frac{v}{v_c}\right)^3 G(\alpha) \delta^{3/2} \left(\frac{v^2}{eBR}\right)}, \quad (7)$$

here a is the characteristic scale length of the hot core of the Tokamak plasma.

The value χ_i^r and power loss due to χ_i^r in the INTOR parameters are shown in Figs. (1) and (2).

(3) Loss of reacting tail

The field ripple also induces the orbit loss of high energy particles, α particles produced in fusion reaction and high energy ions from NBI heating. Energetic members of the bulk-ion population, which mainly contribute to thermonuclear fusion rate, can diffuse more rapidly away from the hot central region by ripple diffusion process, and then this phenomena may reduce the fusion reaction rate substantially⁶⁾. In this section, we examine the loss process of the tail of Maxwellian ions by field ripple, and evaluate an allowable ripple in INTOR.

In the energy range of Eq. (6), we can approximate the distribution function by $\partial/\partial\eta \approx 0$. Then, we determine the distribution function of tail from an averaged form of Eq. (2), i.e.

$$\frac{1}{\tau_s} \frac{1}{v^2} \frac{\partial}{\partial v} \left\{ (v_c^3 + v^3) f \right\} - \frac{f_M}{\tau_{\text{loss}}} = 0, \quad (8)$$

where f_M is Maxwell distribution function

$$f_M = \frac{n}{(2\pi)^{3/2} v_T^3} e^{-\frac{v^2}{v_T^2}}$$

For $v_1 < v_T \ll v < v_c \sim v_2$, f becomes

$$f \approx - \frac{\tau_s^2 G(\alpha) \delta^{3/2} v_T^2}{v_c^6 \omega_{ci}^2 R^2 a^2} v^8 f_M. \quad (9)$$

We define the cut off velocity, v_{cut} , above which the distribution function of ion deviated from Maxwell distribution seriously,

$$v_{\text{cut}} \sim \left\{ \frac{v_c^6 \omega_{ci}^2 R^2 a^2}{\tau_s^2 \delta^{3/2} G(\alpha) v_T^2} \right\}^{1/8} \quad (10)$$

For $q_a = 2.5$, $\bar{T} \approx 10$ keV, $\bar{n} = 10^{20}$, $B = 5T$, $\epsilon = 0.2$, the cut off velocity is given as

δ	Cut off energy (v/v_T)
0.005	2.4
0.002	4.0
0.001	5.8

Thus, δ must be less than 0.005 for 20 % reduction of the thermonuclear reaction⁷⁾.

(4) Loss cone by ripple field

For energy range

$$v > v_3 \quad , \quad (11)$$

where

$$v_3 \equiv \left(\frac{v_c^3 eBaR}{\delta \tau_s m} \right)^{1/5} \quad ,$$

such as α particles produced in thermonuclear reactions or fast ions from NBI, ripple trapped particles can escape from plasma column before they diffuse out from ripple well by Coulomb collision. Then, in the energy range of Eq. (11), a sort of loss cone distribution is formed by the ripple field. In this section, we estimate the width of this loss cone.

The variation in field strength along a field line is

$$\frac{\partial B}{\partial S} = \frac{B_0}{R} \left(\frac{\epsilon}{q} \sin\theta + \delta N \sin N\psi \right) \quad , \quad (12)$$

The condition for a ripple well to occur, given by $\partial B/\partial S = 0$, is

$$\delta > \frac{\epsilon}{qN} |\sin\theta| \quad . \quad (13)$$

and a field minimum occurs at

$$N\psi = 2m\pi - \sin^{-1}(\alpha \sin\theta)$$

where $\alpha = \epsilon/Nq\delta$ and $m = 0, 1, 2, \dots, N-1$.

The separation width of ripple is

$$\Delta\psi \sim \frac{2\pi}{N} \quad \text{or} \quad \Delta\theta \sim \frac{2\pi}{Nq} .$$

Or, equivalently in velocity space,

$$\Delta v \sim \frac{\pi\sqrt{\epsilon}}{Nq} , \quad (14)$$

For deeply trapped particles whose banana orbits are limited in a region

$$\sin\theta < \frac{1}{\alpha} , \quad (15)$$

or

$$\frac{v_{\parallel}^2}{v^2} \Big|_{\theta=0} < \frac{\epsilon}{1+\epsilon} \left(1 - \sqrt{1 - \frac{1}{\alpha^2}} \right) ,$$

the characteristic loss time to loss cone is given by

$$\tau_3 \sim \tau_s \frac{2m_{\alpha}}{m_i} \frac{v_c^3}{v^3} \left(\frac{Nq}{\pi} \right)^2 \frac{1}{\epsilon} . \quad (16)$$

Then, for deeply trapped particles, loss to ripple loss-cone is much faster than their slowing down time. Otherwise, for transit particles, their characteristic loss time is order of their energy transfer time,

$$\tau_{\text{loss}} \sim \tau_s \frac{2m_{\alpha}}{m_i} \frac{v_c^3}{v^3} . \quad (17)$$

Therefore, a magnitude of effective loss cone is not $\sqrt{\delta}$ but order of $\sqrt{\epsilon}$ for fairly high ripple machine ($\alpha \sim 1$).

(5) Conclusion

The magnetic field ripple due to the discrete nature of coils in a Tokamak leads to reduction of fusion reaction rate and formation of loss cone distribution of high energy particle. It is desirable for INTOR to keep field ripple value δ below 0.005 in a hot core region.

References

- 1) T.E. Stringer, Nuclear Fusion 12 (1972) 689.
- 2) J.W. Connor and R.J. Hastie, Nuclear Fusion 13 (1973) 221.

- 3) J.N. Davidson, Nuclear Fusion 16 (1976) 731.
- 4) K.T. Tsang, Nuclear Fusion 17 (1977) 557.
- 5) D.L. Jassby et al, Nuclear Fusion 18 (1978) 825.
- 6) J.G. Gordey and M.J. Houghton, Nuclear Fusion 13 (1973) 215.
- 7) T.J. Dolan, Nuclear Fusion 13 (1973) 960.

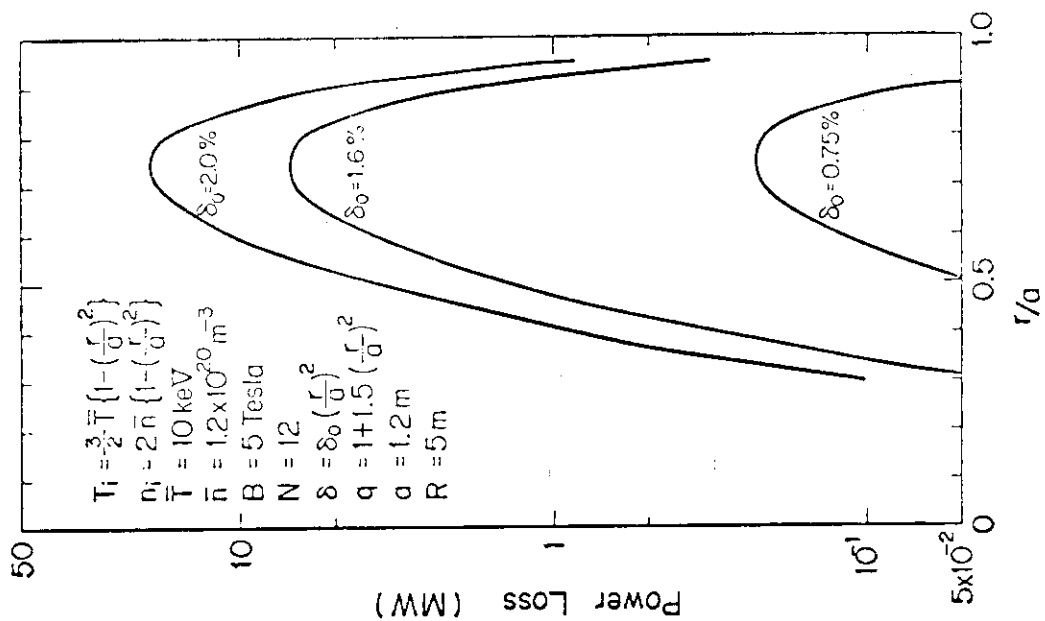


Fig. 2 Power loss due to toroidal field ripple in INTOR parameters.

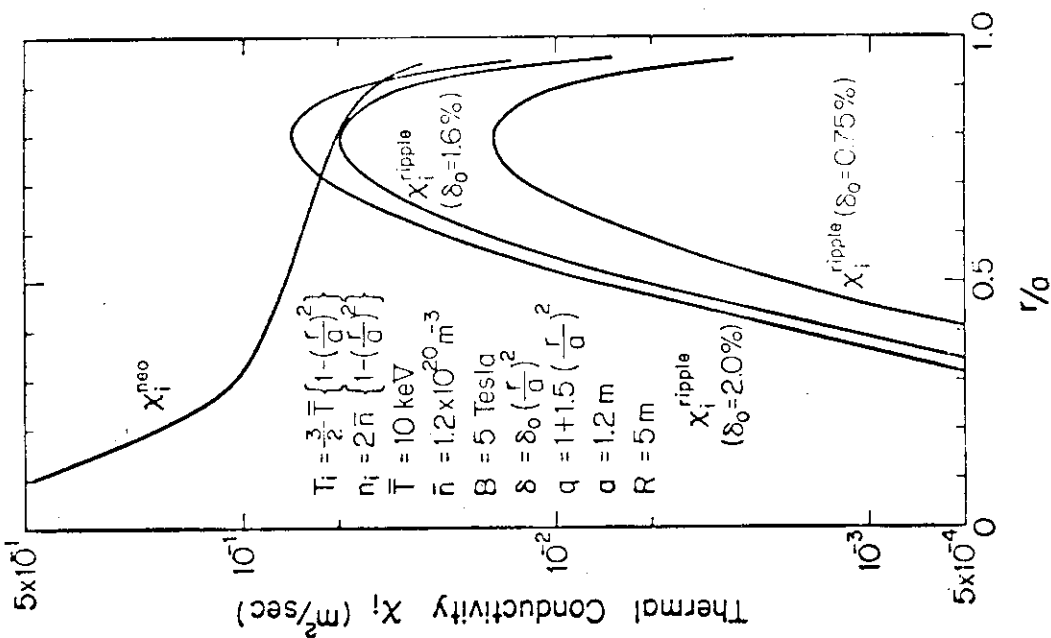


Fig. 1 Thermal conductivity due to toroidal field ripple in INTOR parameters. Neoclassical value is also shown for comparison.

6.2 Effects of Field Ripple on NBI

A quasi-perpendicular injection is preferable to attain sufficient beam penetration. Then the ripple loss of fast ions becomes significant and an appropriate injection geometry is required. Provided that α_0 is the angle between the beam line and the normal to the magnetic-axis and θ_0 is the beam angle with the midplane, the fast ion pitch-angle α on the midplane is given by

$$\sin \alpha = \left\{ \frac{1 + \varepsilon_0 \cos \theta_0}{1 + \varepsilon_0} \right\}^{1/2} \sin \alpha_0 \quad ,$$

where ε_0 is the inverse aspect ratio of the magnetic surface on which fast ions are born. We can define a pitch angle α_c at which the fast ions are critically trapped in the toroidal field ripple. When the distribution of the toroidal field ripple is given by

$$\delta(r, \theta, \psi) = \delta_0 \left(\frac{r}{a} \right)^2 \cos \theta \cos N\psi \quad ,$$

the relations between the critical pitch-angle α_c and the ripple field amplitude δ_0 are given in Fig. 1. Essential requirement for the injection geometry is $\alpha > \alpha_c$ and it becomes apparent from slowing-down calculations that $\alpha - \alpha_c = 5^\circ \sim 10^\circ$ will be a reasonable choice for the reduction of the fast ion ripple loss. When we design the toroidal coil system so that $\delta_0 \approx 0.5\%$, α_c becomes about 10° and α must be $15^\circ \sim 20^\circ$. Contours of $\alpha = \alpha_c + 5^\circ$ are plotted on the $\alpha_0 - \theta_0$ plane in Fig. 2. Then we have $\alpha_0 = 15^\circ$ and $\theta_0 = 7^\circ$ in accordance with $\alpha \geq 15^\circ$.

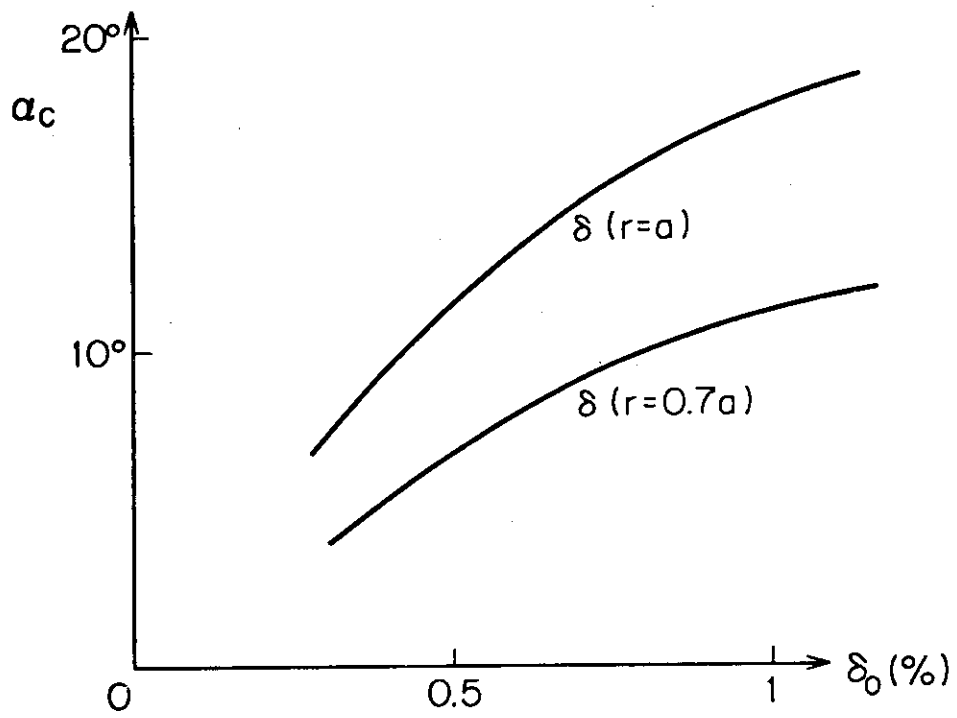


Fig. 1 Critical pitch angle for ripple trapping versus toroidal field ripple.

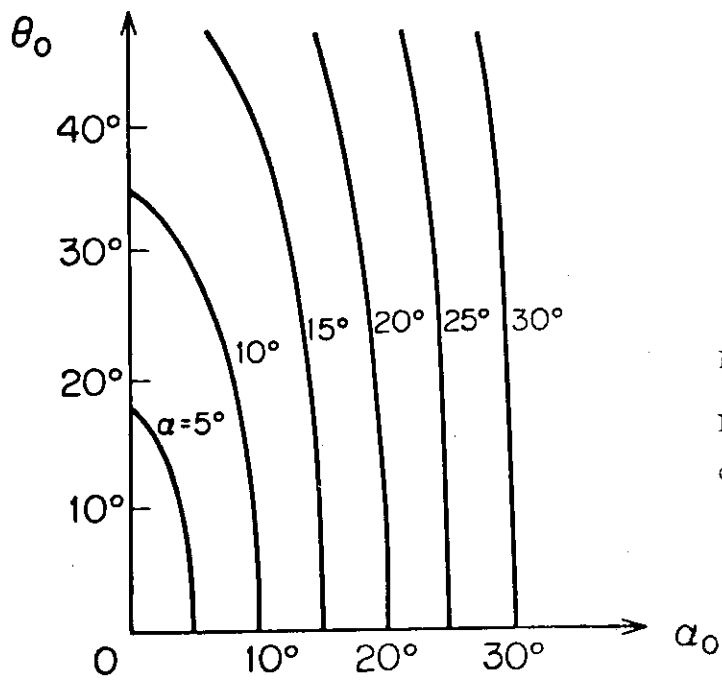


Fig. 2
Fast ion pitch angle on the midplane.

6.3 Ripple Loss of Fast Ions During Slowing Down

Model

In order to study the detailed behaviours of fast ions during slowing down process in a non-axisymmetric magnetic field, we have employed a Monte-Carlo simulation techniques. The Monte-Carlo techniques were adopted to simulate the following collisional processes;

- i) Coulomb collision of fast ions with plasma ions and electrons with the Maxwellian velocity distributions.
- ii) Coulomb collision of fast ions with impurity ions.

Charge-exchange reactions are excluded in the present calculation.

Calculations of these collisional processes have been carried out for every test particles drifting along their guiding center orbits, which are described by

$$\frac{dv_{g\parallel}}{dt} = -\frac{\mu}{m} \frac{\partial B}{\partial \ell}, \quad \vec{v}_{g\perp} = -\frac{v_{\parallel}^2 + v_{\perp}^2/2}{\Omega} \vec{b} \times \frac{\partial \vec{b}}{\partial \ell}$$

where μ is the magnetic moment, $\vec{b} = \vec{B}/|B|$ and $\Omega = -qB/m$.

The magnetic field B is given by

$$\begin{aligned} \vec{B} &= \vec{B}_{\psi}(r, \theta, \psi) + \vec{B}_{\theta}(r, \theta), \\ B_{\psi} &= B_t (R_0/R) (1 + \delta \cos N_t \psi) \quad (\text{toroidal magnetic field}), \\ B_{\theta} &= (R_0/R) B_p(r) \quad (\text{poloidal magnetic field}), \\ B_t &: \text{toroidal field on the magnetic axis } (R_0), \\ B_p &: \text{poloidal field defined by the plasma current,} \\ N_t &: \text{number of the toroidal field coils,} \\ \delta &: \text{amplitude of the toroidal field ripple.} \end{aligned}$$

Results

Calculations have been performed for the INTOR parameters. They are summarized in Table 1.

Two kinds of fast ion loss processes are found in our simulation study; (1) ripple-trapped drift loss and (2) banana drift loss. The energy fractions lost to the wall are shown in Fig. 1 as functions of injection angle for co-injection + counter injection, where G_{rt} is the energy loss due to ripple-trapped drift motion, G_{r0} is that due to banana drift motion. The sum of G_{rt} and G_{r0} is denoted by G_t . The energy loss G_{s0} is also plotted in case of axisymmetric toroidal field. The difference ($G_{r0} - G_{s0}$) comes from the ripple-enhanced banana drift and the

detrapping from the ripple well. The toroidal field ripple causes the significant enhancement of fast ion loss, and the 15 % ($\sim 3 G_{s0}$) of the injected beam energy is lost to the wall even for the injection angle of 75° . The ripple trapped loss G_{rt} is much smaller than the banana drift loss G_{r0} when the injection angle is set at less than 85° .

Figure 2 shows G_{rt} , G_{r0} and G_t for co-injection only. The ripple enhanced banana drift loss G_{r0} shows only a slight dependence on the sign of the critical pitch angle as compared with G_{r0} for co-injection + counter injection in Fig. 1.

The ripple trapping region is mapped in Fig. 3(a) and (b) in the space of the pitch-angle and the initial toroidal angle ($\psi/(2\pi/N_t)$) of fast ions on the mid-plane for both positive and negative pitch angles respectively. The central region is the ripple trapping region. Side bands appear owing to the finite banana effect coupled with inhomogeneity of the ripple well. The size of the respective side band is proportional to the toroidal drift velocity ($v_d \sim mv^2/(2qB_t R)$).

The radial drift of banana orbits can appear even though the effect of B_r is not taken into account. Figures 4(a) and (b) show the banana size as functions of the initial pitch angle for $\psi/(2\pi/N_t) = 0.1, 0.3, 0.5, 0.7$ and 0.9 . The banana drift becomes discrete for the pitch angle when the fast ions fall onto the peak of a ripple.

Table 1 Plasma and neutral beam parameters

major radius	$R = 5.0$ (m)
minor radius	$a = 1.2$ (m)
toroidal field	$B_t = 5.0$ (T)
temperatures	$T_e(r) = T_i(r) = 1.5 \times 10^4 (1 - (r/a)^2)$ (eV) $(T_D(r) = T_T(r) = T_i(r))$
plasma density	$n_e(r) = 2.0 \times 10^{20} (1 - (r/a)^2)$ (m ⁻³) $(n_D(r) = n_T(r) = n_i(r))$
plasma current	$j_p(r) = j_0 (1 - (r/a)^2)$
safety factor	$q_a = 2.5$
effective Z	$Z_{eff} = 1.5$ (uniform)
charge number of impurity ion	$Z_{imp} = 8.0$ (oxygen)
beam energy	$E_b = 200.0$ (keV)
energy components of the neutral beam	$E_b : E_b/2 : E_b/3 = 1.0 : 0.2 : 0.1$
toroidal field ripple	$\delta = \delta_0 \delta_1(r) \exp(-\beta \theta^2)$ $\delta_0 = 0.75 \%$, $\delta_1(r) = (r/a)^2$, $\beta = 0.5$,
number of toroidal coils	$N_t = 12$

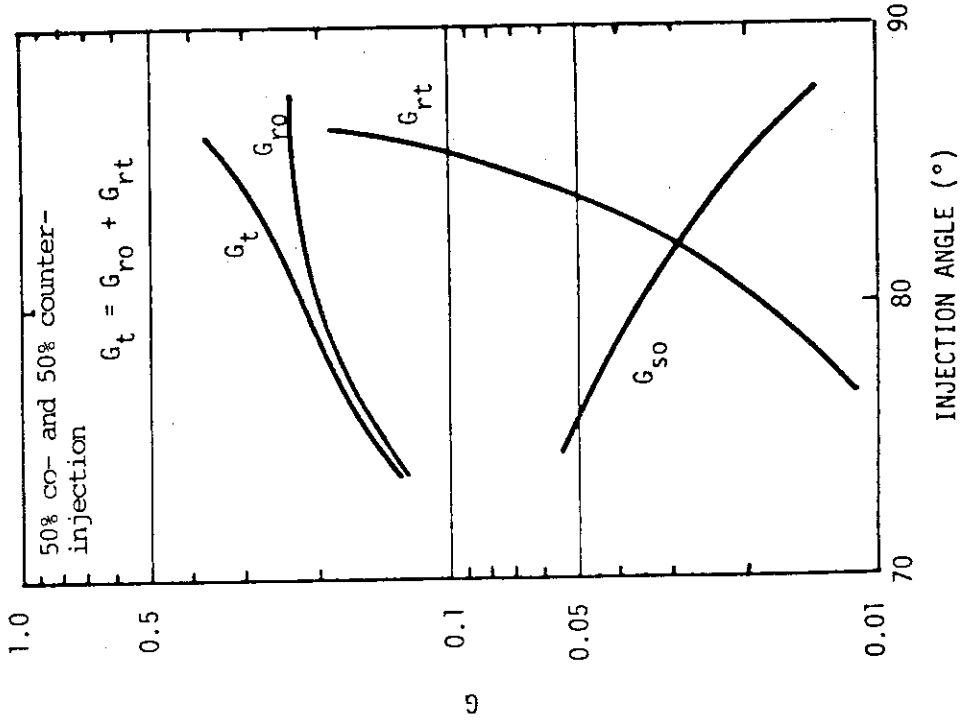


Fig. 2 Beam energy loss during the slowing down process of fast ions in a non-axisymmetric toroidal field for $\delta_0 = 0.75\%$.

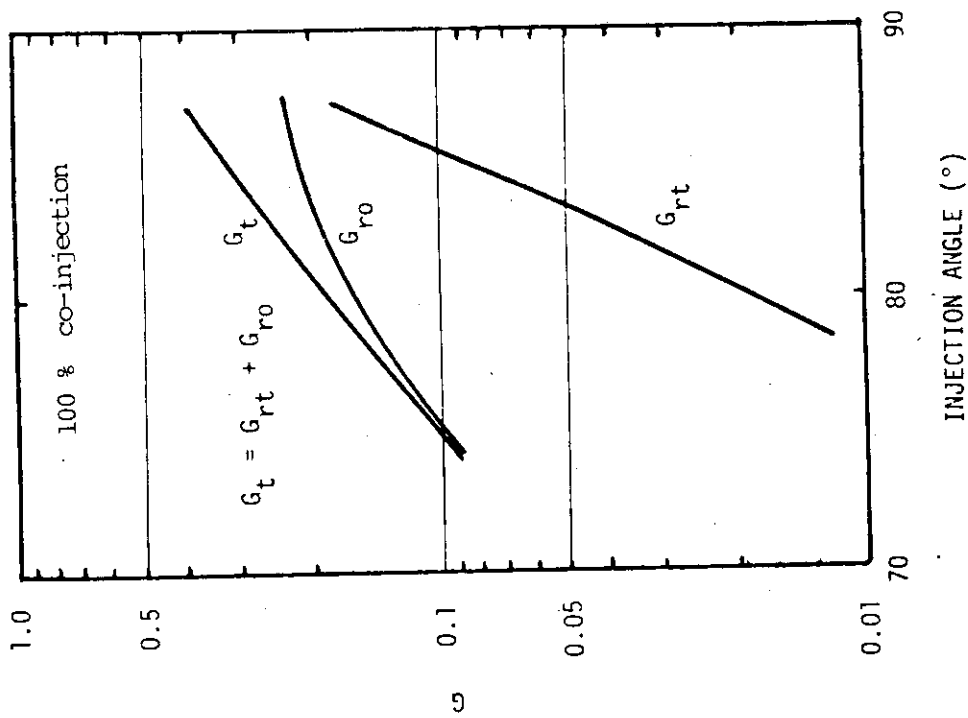


Fig. 1 Beam energy loss during the slowing down process of fast ions in a non-axisymmetric toroidal field for $\delta_0 = 0.75\%$ and co-injection only.

$\delta = 0.75\%$, NT=12.
 RT=5.00M, R=1.20M, BT=5.00T, QA=2.50
 R/A=0.90, Z/A=0.00, EB=200.0KEV

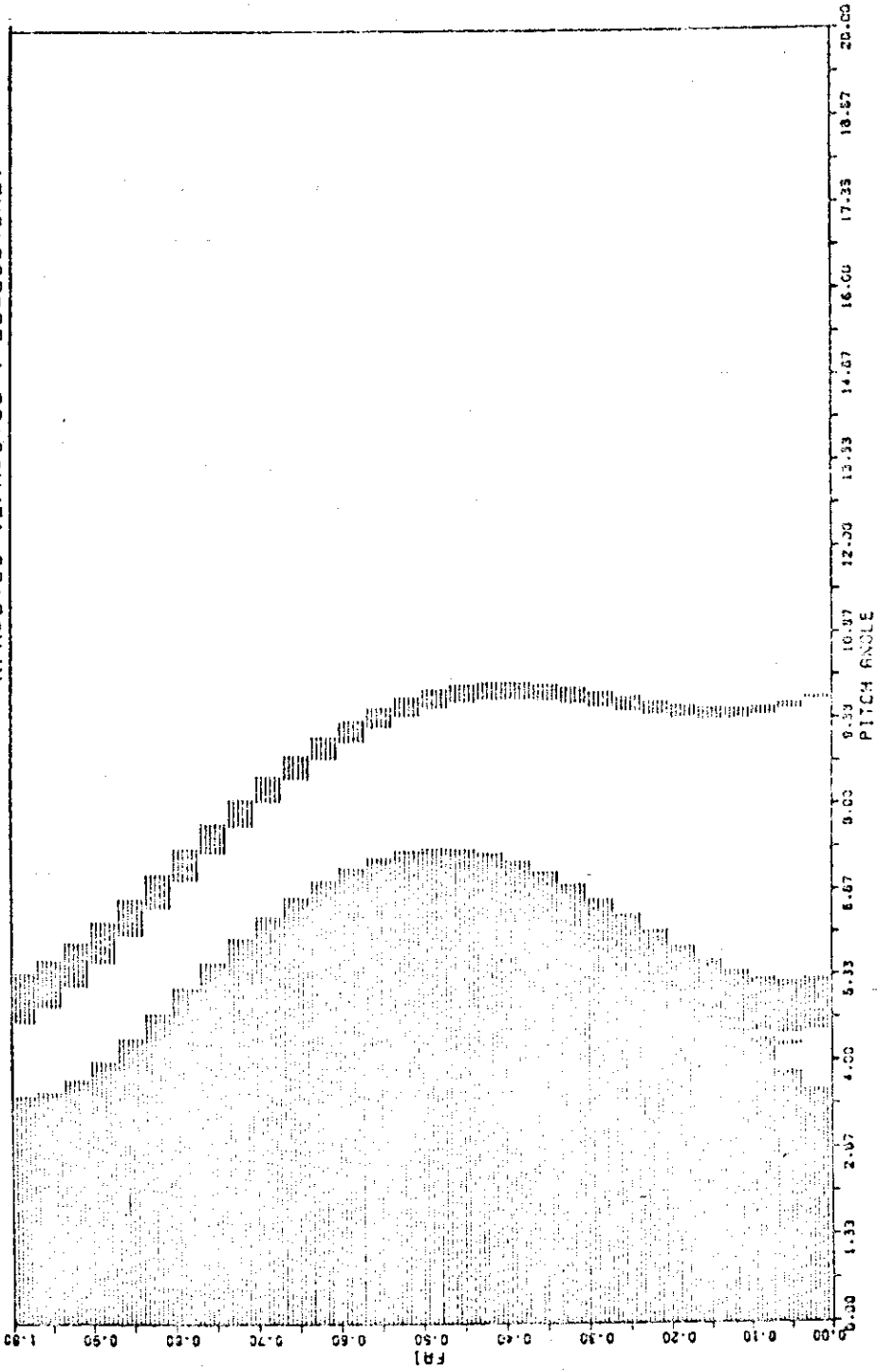


Fig. 3(a) Ripple trapping region in the space of the initial pitch angle and the toroidal angle ($\psi/(2\pi/N_T)$) of fast ions on the mid-plane for positive pitch-angles.

$\delta=0.75\%$, NT=12.
 RT=5.00M, R=1.20M, BT=5.00T, CA=2.50
 R/A=0.90, Z/A=0.00, EB=200.0KEV

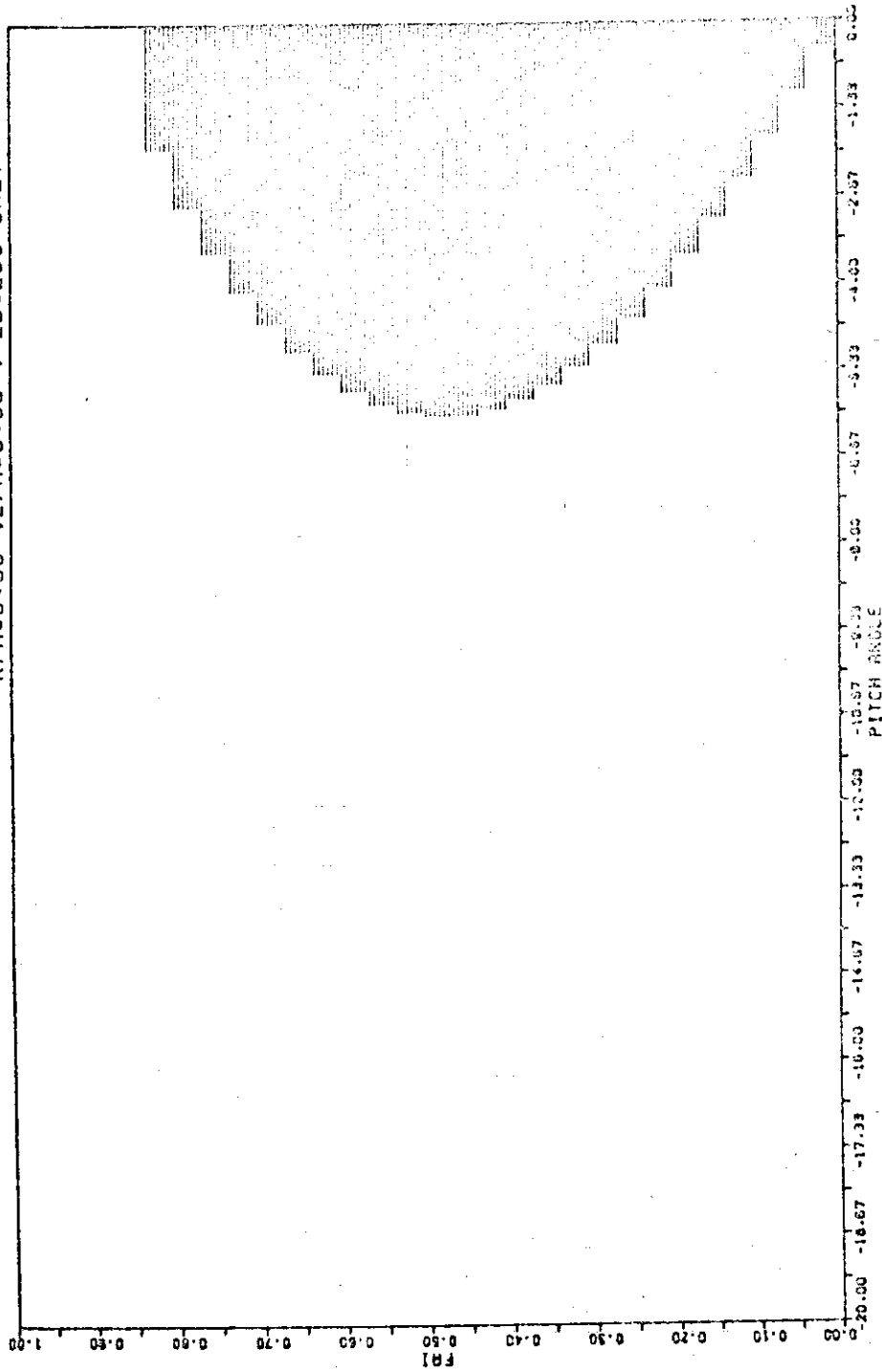


Fig. 3(b) Ripple trapping region for negative pitch angles.

$\epsilon = 0.75\%$, $NT = 12$,
 $RT = 5.00M$, $A = 1.20M$, $BT = 5.00T$, $QA = 2.50$
 $R/A = 0.90$, $Z/A = 0.00$, $EB = 200.0KEV$

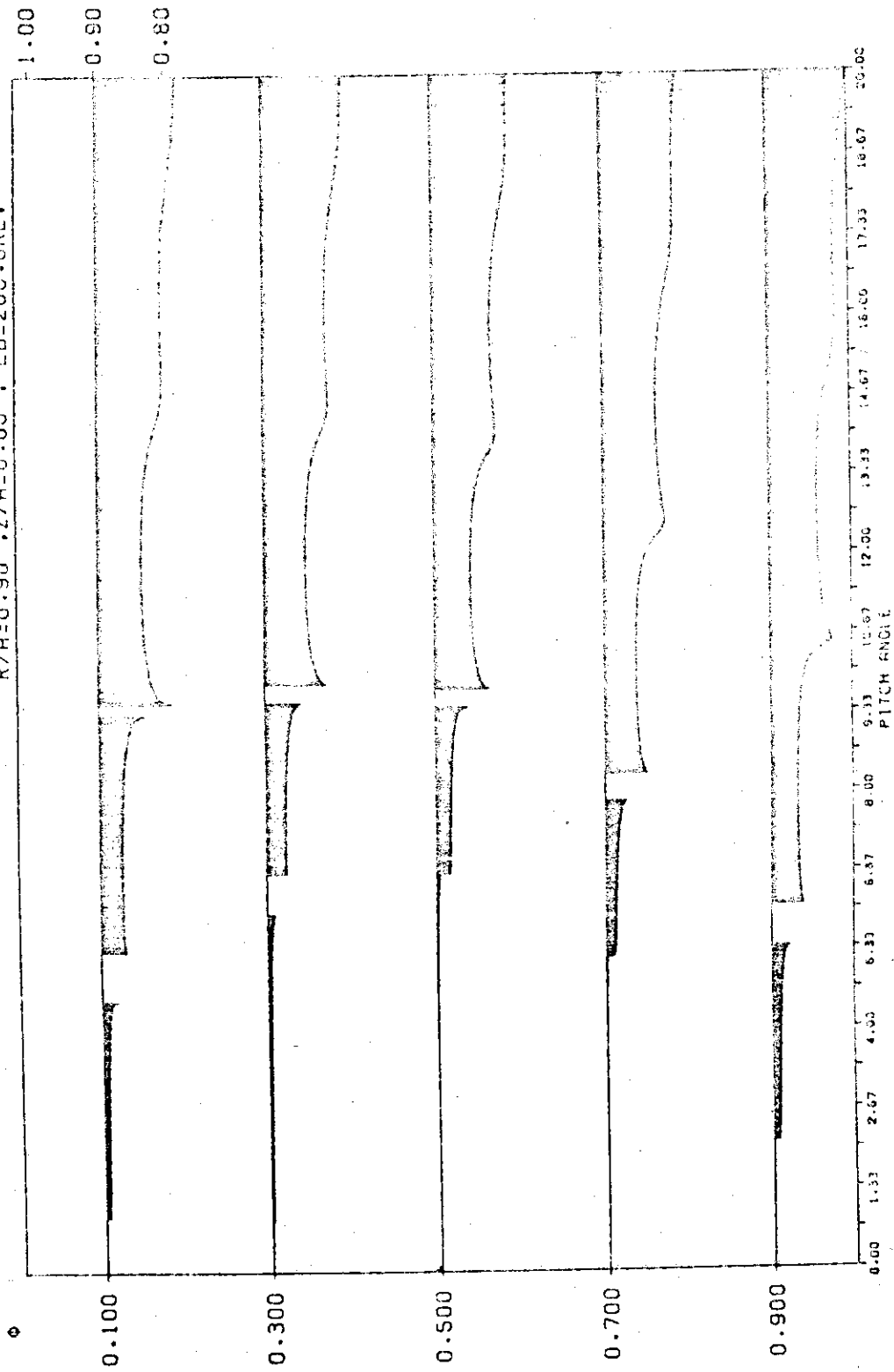


Fig. 4(a) Banana size as functions of the initial pitch angle (positive)
 for $\psi/(2\pi/N_F) = 0.1, 0.3, 0.5, 0.7$ and 0.9 .

$\delta = 0.75\%$, $NI = 12$,
 $RT = 5.00M$, $R = 1.20M$, $SI = 5.00T$, $QA = 2.50$
 $R/A = 0.90$, $Z/A = 0.00$, $EB = 200.0KEV$

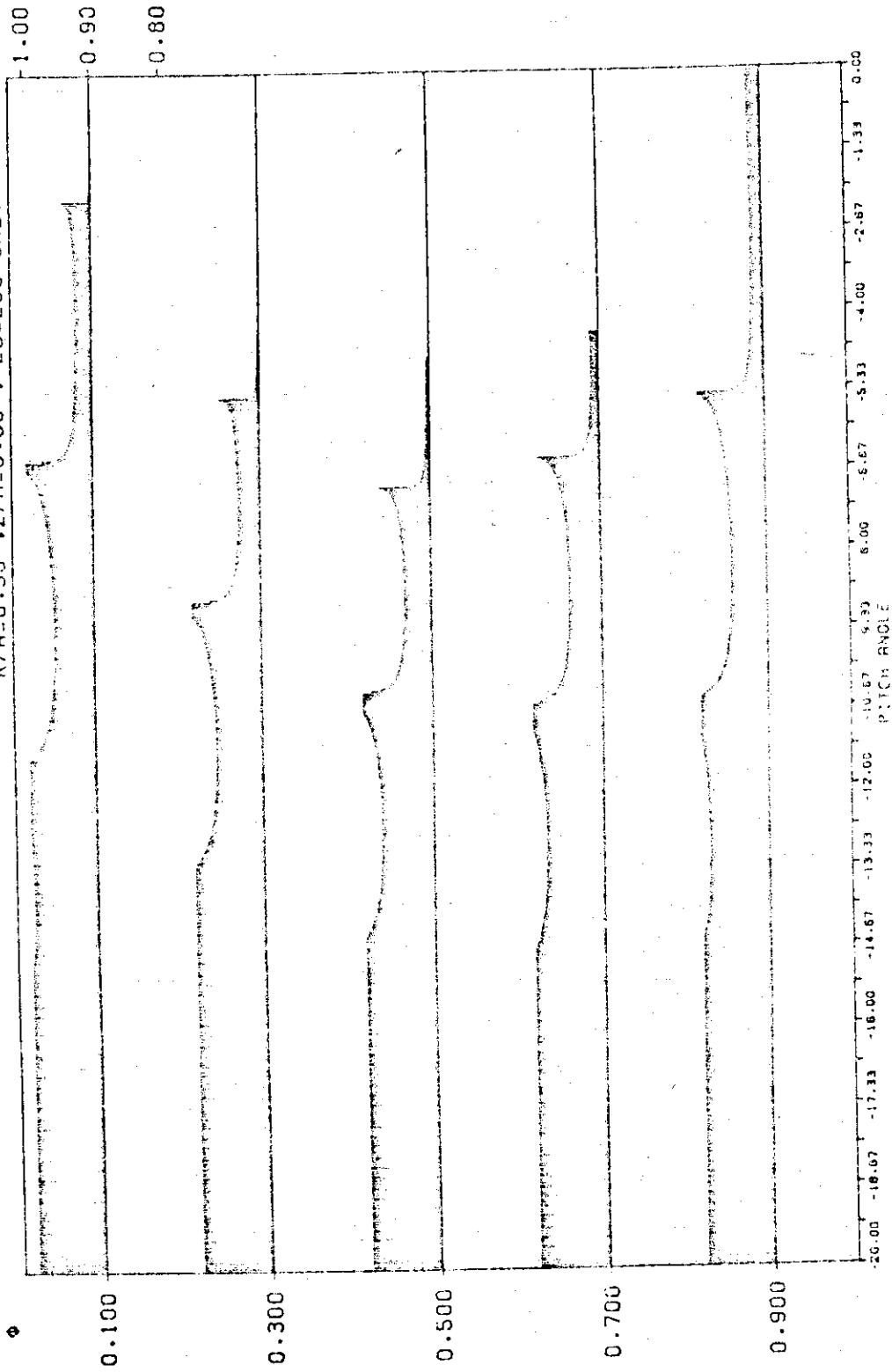


Fig. 4(b) Banana size as functions of the initial pitch angle (negative).

7. Confinement of Alpha Particles

7.1 Orbit Losses of 3.5 MeV Alpha Particles in an Axisymmetric Tokamak

The plasma current 4.7 MA in INTOR is sufficient to confine 3.5 MeV alpha particles. Detailed analysis is given in the following.

(1) Introduction

It is expected that alpha particles with energy 3.5 MeV, which are generated by D-T reaction, heat the plasma in a tokamak. However, the displacement Δ of an alpha-particle orbit from a magnetic surface, $\Delta/a \sim \sqrt{a/R_0}/I_p$ (a is the plasma minor radius, R_0 is the major radius, and the plasma current I_p is in MA), is large even in a large tokamak such as INTOR that alpha particles generated near the plasma surface are lost directly from the plasma (this loss is called the "orbit loss") and the efficiency of alpha-particle heating becomes low.

Heat load and damage of the limiter and wall due to 3.5 MeV alpha particles are also unnegligible.

In this section, we investigate numerically the "orbit losses" of 3.5 MeV alpha particles in an axisymmetric, elliptic cross-section tokamak. Parameter dependencies of the "orbit losses" are shown in detail.

(2) Model of numerical calculation

We use a cylindrical co-ordinate (R, ψ, Z) , and solve numerically equations of guiding-center motion, in which effects of electric fields are neglected, by using the predictor-corrector method. Magnetic axis of a tokamak lies at $(R_0, \psi, 0)$, and a magnetic surface is considered to be an ellipse expressed as follows (see Fig. 1):

$$\frac{b}{a} (R-R_0)^2 + \frac{a}{b} Z^2 = ab\rho^2 \quad 0 \leq \rho \leq 1 \quad (2.1)$$

where a is the plasma minor radius in the R direction and b is the radius in the Z direction. Shift of magnetic axis and variation of ellipticity are not taken into account, for simplicity. The magnetic field $\vec{B} = (B_R, B_\psi, B_Z)$ is then given by

$$B_R = -\frac{a}{b} \frac{Z}{\sqrt{ab}} \frac{R_0}{R} \tilde{B}(\rho) \quad (2.2)$$

$$B_\psi = \frac{R_0}{R} B_0 \quad (2.3)$$

$$B_Z = \frac{b}{a} \frac{R-R_0}{\sqrt{ab}} \frac{R_0}{R} \tilde{B}(\rho) \quad (2.4)$$

Effects of diamagnetism or paramagnetism of a plasma are neglected in Eq.(2.3). Quantity $\tilde{B}(\rho)$ is a function of ρ and is considered to be expressed as

$$\tilde{B}(\rho) = \tilde{B}(1) \frac{1+\gamma}{1+\gamma\rho^m} \quad (2.5)$$

where $\tilde{B}(1) = \mu_0 I_p / 2\pi r_{\text{eff}}$ with $r_{\text{eff}} = (R_0^2 / \sqrt{ab}) [1 - (1 - a^2/R_0^2)^{1/2} + (b^2/a^2) \{(1 - a^2/R_0^2)^{-1/2} - 1\}] \approx (a^2 + b^2) / 2\sqrt{ab}$. Since the toroidal current density is nearly zero at $\rho=1$, the relation $m = \{(b/a) + (a/b)\}(1+\gamma)/\gamma$ is obtained. The coefficient γ is related to the safety factor $q(\rho)$ approximately as $1+\gamma \approx q(1)/q(0)$.

We trace the orbit of an alpha particle with energy 3.5 MeV, and investigate whether it is confined or lost, whose start point is located at (ρ_s, θ_s) or (R_s, Z_s) ,

$$R_s = R_0 + ab(b^2 \cos^2 \theta_s + a^2 \sin^2 \theta_s)^{-1/2} \rho_s \cos \theta_s \quad (2.6)$$

$$Z_s = ab(b^2 \cos^2 \theta_s + a^2 \sin^2 \theta_s)^{-1/2} \rho_s \sin \theta_s \quad (2.7)$$

and pitch angle $\phi = \sin^{-1}(v_\parallel/v)$ is ϕ_s at the start point. In an axisymmetric tokamak, loss region in ϕ space lies in $\phi_{L1}(R_s, Z_s) \geq \phi_s \geq \phi_{L2}(R_s, Z_s)$. If the pitch angles of alpha particles generated by D-T reaction are isotropic, then $g(R_s, Z_s)$, the confinement ratio of alpha particles generated at the position (R_s, Z_s) , can be given as

$$g(R_s, Z_s) = 1 - \frac{1}{2} (\sin \phi_{L1} - \sin \phi_{L2}) \quad (2.8)$$

Probability of generation of alpha particles is considered to be equal at each point on a magnetic surface. Therefore, $G(\rho_s)$, the confinement ratio of alpha particles generated on a magnetic surface $\rho=\rho_s$, can be obtained by averaging over angle θ_s , where the surface area is taken into account for the weight.

(3) Results of calculations

Now we show the results of numerical calculations. Figure 2 demonstrates a typical banana orbit of a 3.5 MeV alpha particle, where $R_0=5$ m, $A=1.2$ m, $b=1.8$ m, $B_0=5$ T, and $I_p=4.7$ MA. Loss regions

in (θ_s, ϕ_s) plane are shown in Fig. 3, where parameters are the same as in Fig. 2. One can see that particles with banana orbits displaced outward are lost even from inner region ($\rho=0.7, 0.8$), and that both trapped and transit particles, which are generated near the surface ($\rho=0.9$), are lost.

(a) dependence of loss on plasma current

The "orbit loss" mainly depends on the toroidal plasma current I_p and the aspect ratio R_o/a , because the displacement of an orbit from a magnetic surface is of the order of $\Delta/a \sim \sqrt{a/R_o}/I_p$. In Fig. 4(a), the confinement ratio G for various I_p is shown as a function of ρ , where $R_o=5$ m, $a=1.2$ m, $b=1.8$ m, $B_o=5$ T, and $\gamma=0.6$. Dependence of the loss ratio $1-G$ on I_p is shown in Fig. 4(b). The bend of a $\rho=\text{const.}$ curve (e.g. near $I_p=3.3$ MA on a $\rho=0.8$ curve) is caused by the fact that only trapped particles are lost for large plasma current and both trapped and transit particles are lost for small current. The value of I_p near the bend is approximately proportional to $\sqrt{a/R_o}/(1-\rho)$.

(b) dependence of loss on aspect ratio

In Fig. 5(a), $G(\rho)$ is shown for various a/R_o , where $R_o=5$ m, $b/a=1.5$, $B_o=5$ T, $I_p=4.7$ MA, and $\gamma=0.6$. Dependence of $1-G$ on a/R_o is shown in Fig. 5(b). Dots refer to the results obtained by changing a ($R_o=5$ m and $b/a=1.5$), and open circles are obtained by changing R_o ($a=1.2$ m and $b=1.8$ m). The bend of a curve (e.g. near $a/R_o=0.24$ on a $\rho=0.85$ curve) is caused by the fact that only trapped particles are lost for small a/R_o . The value of a/R_o near the bend is approximately proportional to $(1-\rho)^2 I_p^2$. On the other hand, crosses (broken curves) in Fig. 5(b) refer to the results obtained by changing b/a (\sqrt{ab} and R_o are constant): $b/a=1$ for $a/R_o=0.294$, $b/a=1.25$ for $a/R_o=0.263$, $b/a=1.5$ for $a/R_o=0.24$, and $b/a=1.75$ for $a/R_o=0.222$. One can see that the "Orbit loss" in an elliptic tokamak is larger than that in a circular tokamak when values of a/R_o are the same (the volume of an elliptic tokamak is larger than that of a circular tokamak). But, one can also see from broken curves that the loss in an elliptic tokamak is small compared with that in a circular tokamak with the same volume.

(c) dependence of loss on current density profile

Next, dependence of the loss on the current density profile is investigated. Current density profiles at $\theta=\pi/2$ and q profiles are illustrated in Fig. 6, where $R_0=5$ m, $a=1.2$ m, $b=1.8$ m, $B_0=5$ T, $I_p=4.7$ MA, and γ is chosen as a parameter: (a) $\gamma=0.1$, (b) $\gamma=0.6$, (c) $\gamma=1.3$, and (d) $\gamma=2.0$. Figure 7 shows G for various current profiles. Peaked current density profile gives a good confinement compared with flat one.

(d) dependence of loss on toroidal field

Dependence on the toroidal field B_0 is very small: e.g., in the case of $R_0=5$ m, $a=1.2$ m, $b=1.8$ m, $I_p=4.7$ MA, and $\gamma=0.6$. $G(0.8)$ is equal to 0.834 for $B_0=3$ T, and $G(0.8)=0.833$ for $B_0=7$ T.

(e) dependence of loss on plasma size

Dependence on the plasma size is also very small: e.g., in the case of $a/R_0=0.24$, $a/b=1.5$, $B_0=5$ T, $I_p=4.7$ MA, and $\gamma=0.6$, $G(0.8)$ is 0.838 for $R_0=3$ m, and $G(0.8)=0.833$ for $R_0=7$ m.

(4) Orbit Losses of 3.5 MeV Alpha Particles in INTOR

Orbit losses of 3.5 MeV alpha particles in INTOR are numerically studied. Plasma parameters are considered to be as follows:

$$n \propto (1 - \rho^2) \text{ and } T_i = 20 \times (1 - \rho^2) \text{ keV,}$$

where ρ is related to a magnetic surface, $(R-R_0)^2/a^2 + Z^2/b^2 = \rho^2$ ($0 \leq \rho \leq 1$).

The birth profile of 3.5 MeV alpha particles ($\propto n^2 \langle \sigma v \rangle$) is shown in Fig. 8. It is approximately proportional to $(1 - \rho^2)^{3.8}$, because $\langle \sigma v \rangle \sim T_i^{1.8}$ ($10 \text{ keV} < T_i < 20 \text{ keV}$). Sizes of the device are $R_0=4.8$ m and $a_{\text{eff}} \equiv \sqrt{ab} = 1.5$ m, and plasma current I_p is 3.8 MA.

Four cases are investigated;

- (c - i) circular cross section with flat current density distribution,
- (c - ii) circular cross section with peaked current density distribution,
- (e - i) elliptic cross section ($b/a = 1.5$) with flat one,
- (e - ii) elliptic cross section with peaked one.

Current density profiles are illustrated in Fig. 9.

In Fig. 9, the loss rate is shown as a function of ρ . One can easily see that (1) particles are better confined in an

elliptic cross-section tokamak than in a circular cross-section tokamak, and that (2) peaked current density distribution gives a better confinement than flat one. Total orbit-loss fractions are (c - i) 4.7 %, (c - ii) 1.7 %, (e - i) 3.1 %, and (e - ii) 1.2 %.

(4) Conclusions

We summarize the results of numerical calculations of the "orbit losses" of 3.5 MeV alpha particles in an axisymmetric, elliptic cross-section tokamak.

- (1) The "orbit loss" mainly depends on I_p and a/R_o , because $\Delta/a \sim \sqrt{a/R_o}/I_p$ (I_p is in MA).
- (2) Peaked current density profile gives a good confinement compared with flat one.
- (3) The loss in an elliptic tokamak is smaller than that in a circular tokamak with the same volume.

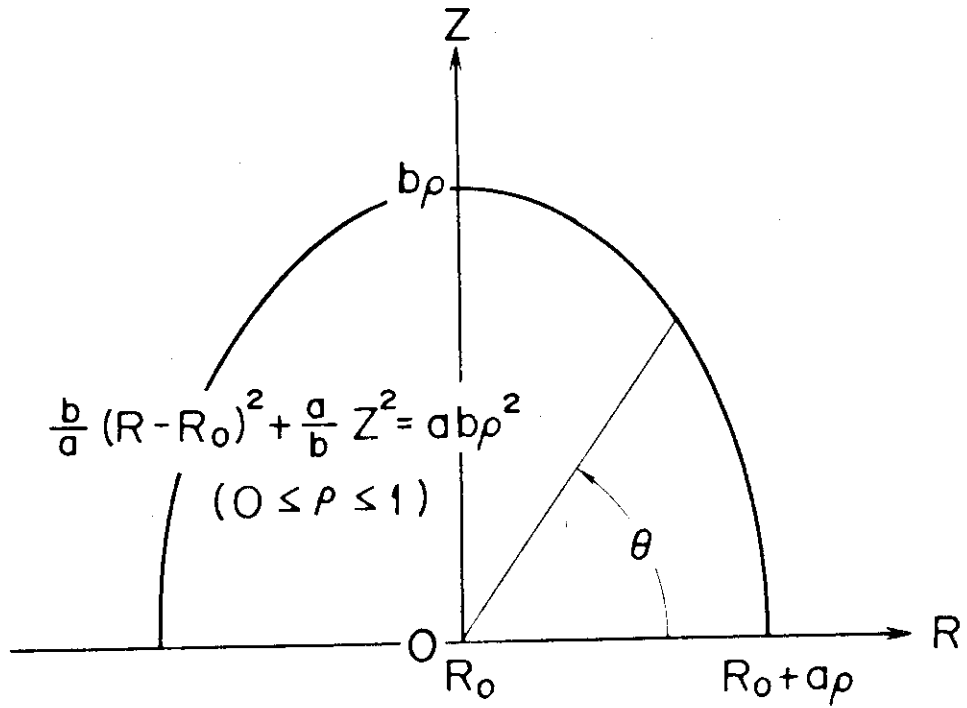


Fig. 1 Magnetic surface of an elliptic tokamak.

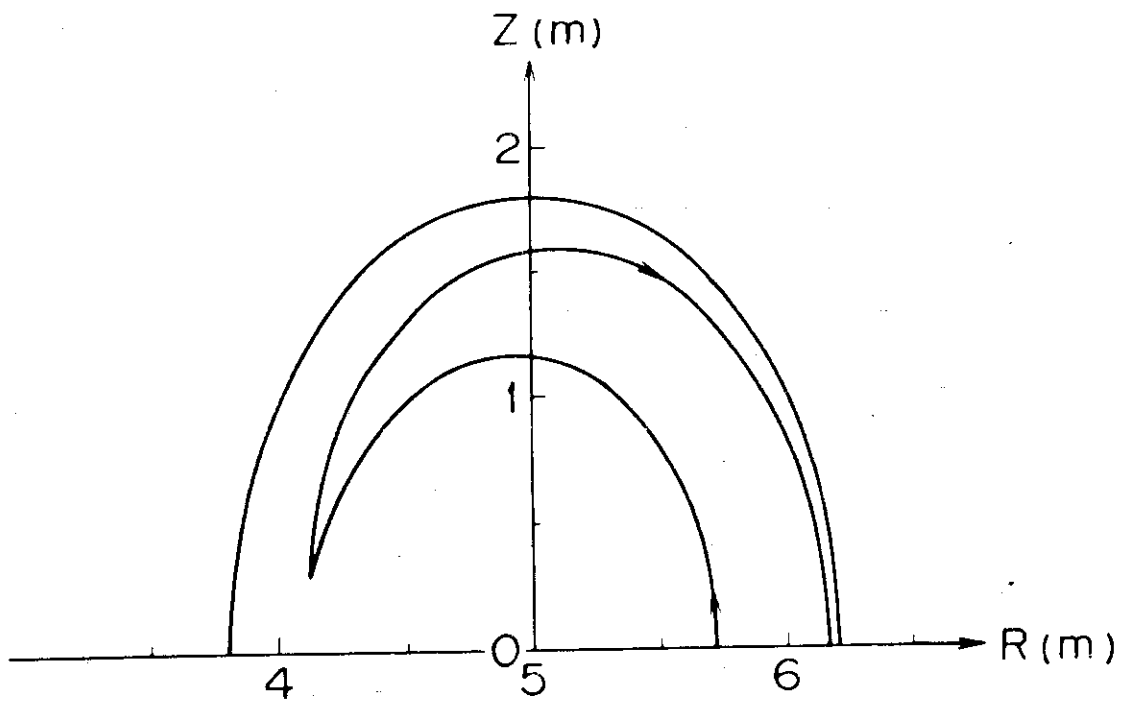


Fig. 2 Typical banana orbit of a 3.5 MeV alpha particle, where $R_0 = 5$ m, $a = 1.2$ m, $b = 1.8$ m, and $I_p = 4.7$ MA.

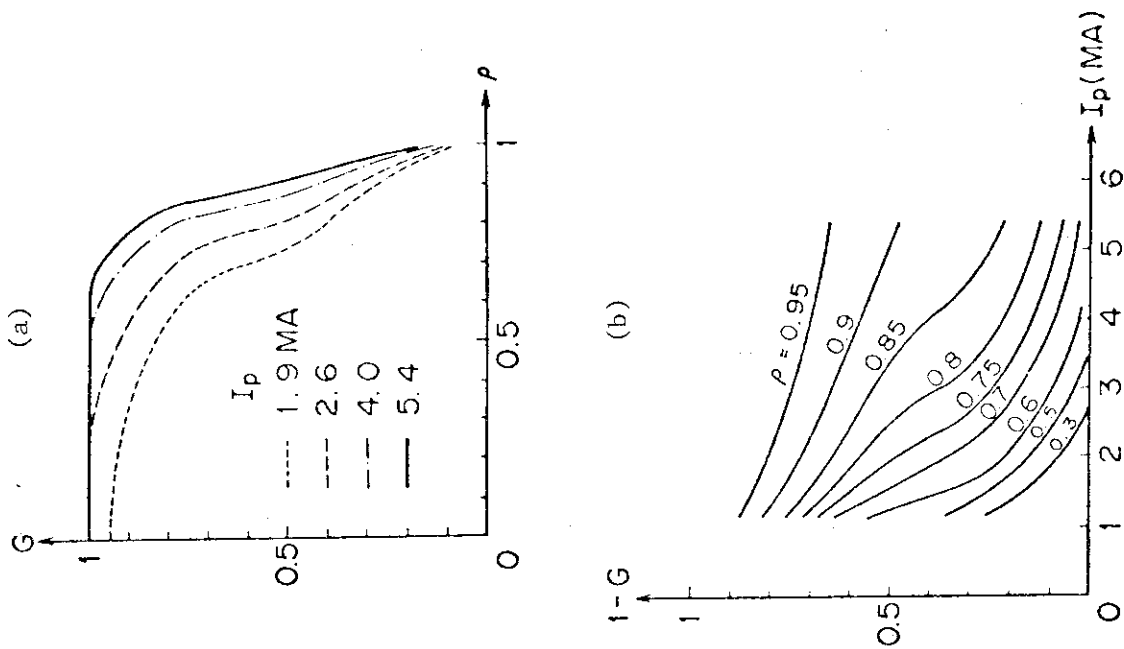


Fig. 4 (a) Confinement ratio G vs ρ for various I_p ,
 (b) dependence of the loss ratio $1-G$ on I_p .

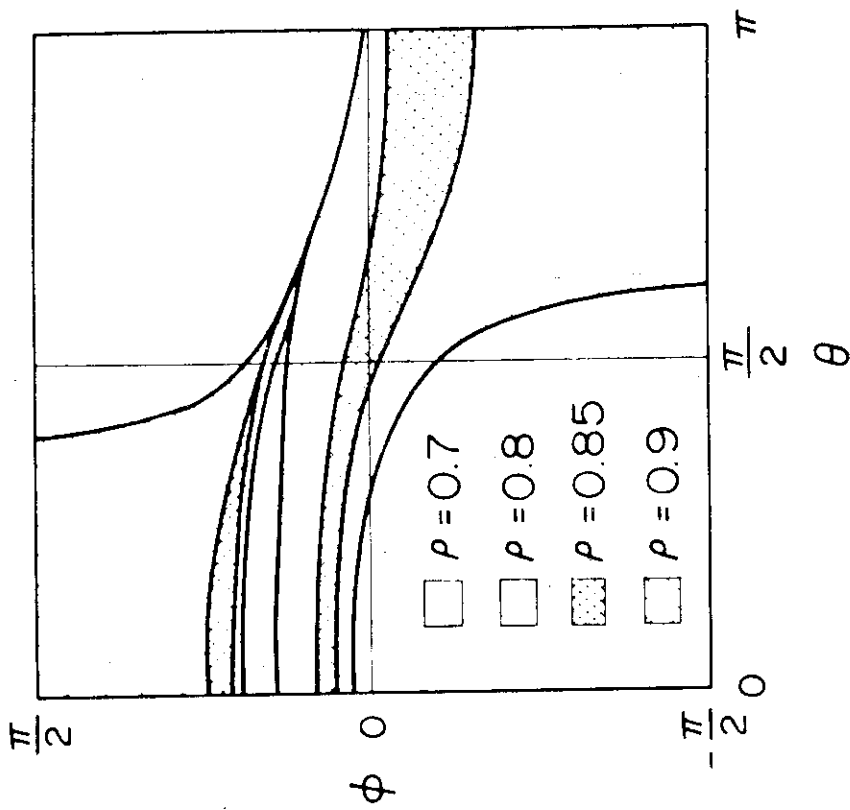


Fig. 3 Loss regions in (θ, ϕ) plane. The angle θ denotes the poloidal angle and $\phi = \sin^{-1}(v/v)$.

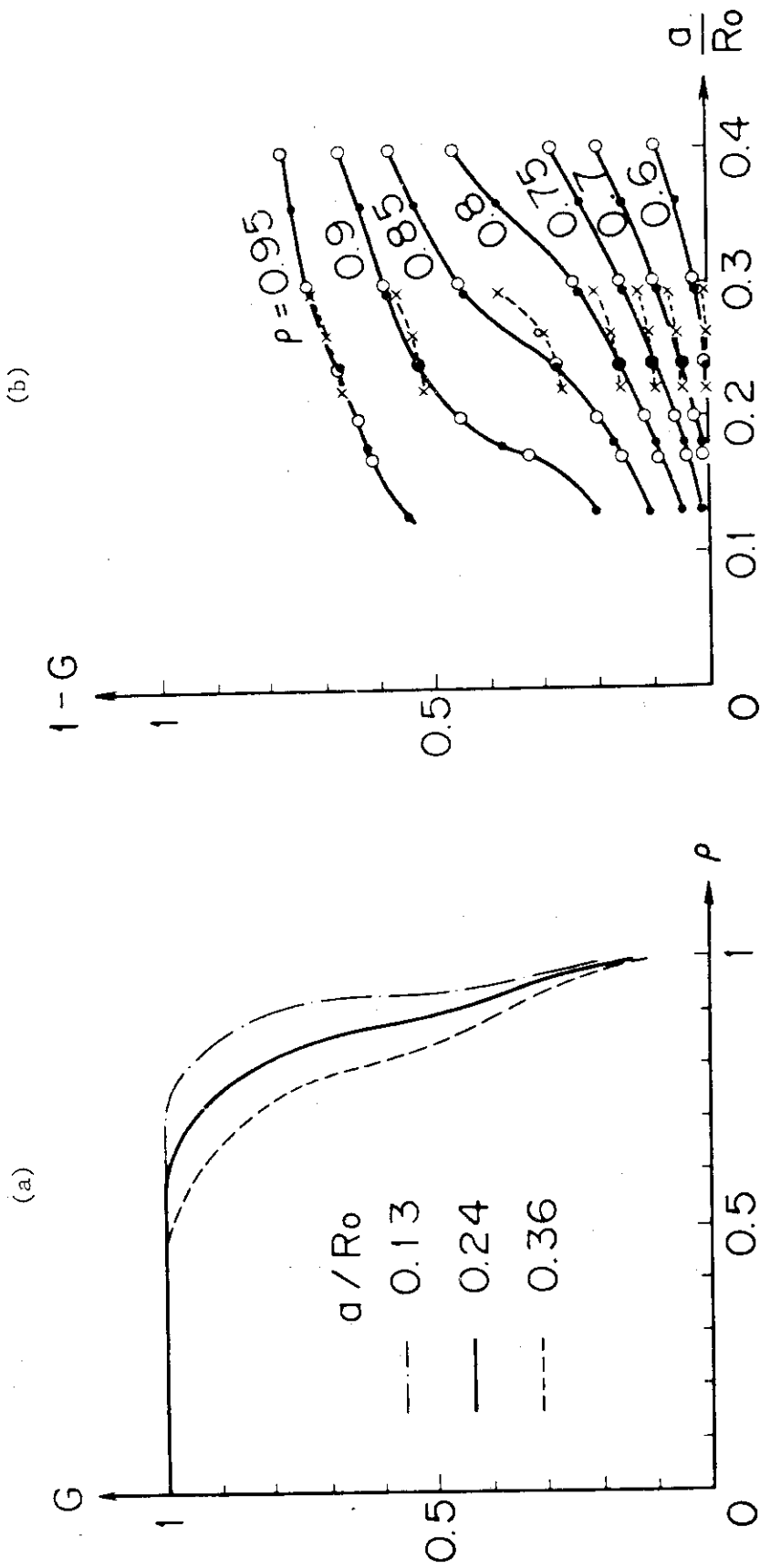


Fig. 5 (a) Confinement ratio G vs ρ for various a/R_0 .
 (b) The loss ratio $1-G$ depends on a/R_0 , where dots and open circles are obtained by changing the minor radius and major radius respectively. Crosses (broken curves) are given by changing b/A with constant volume.

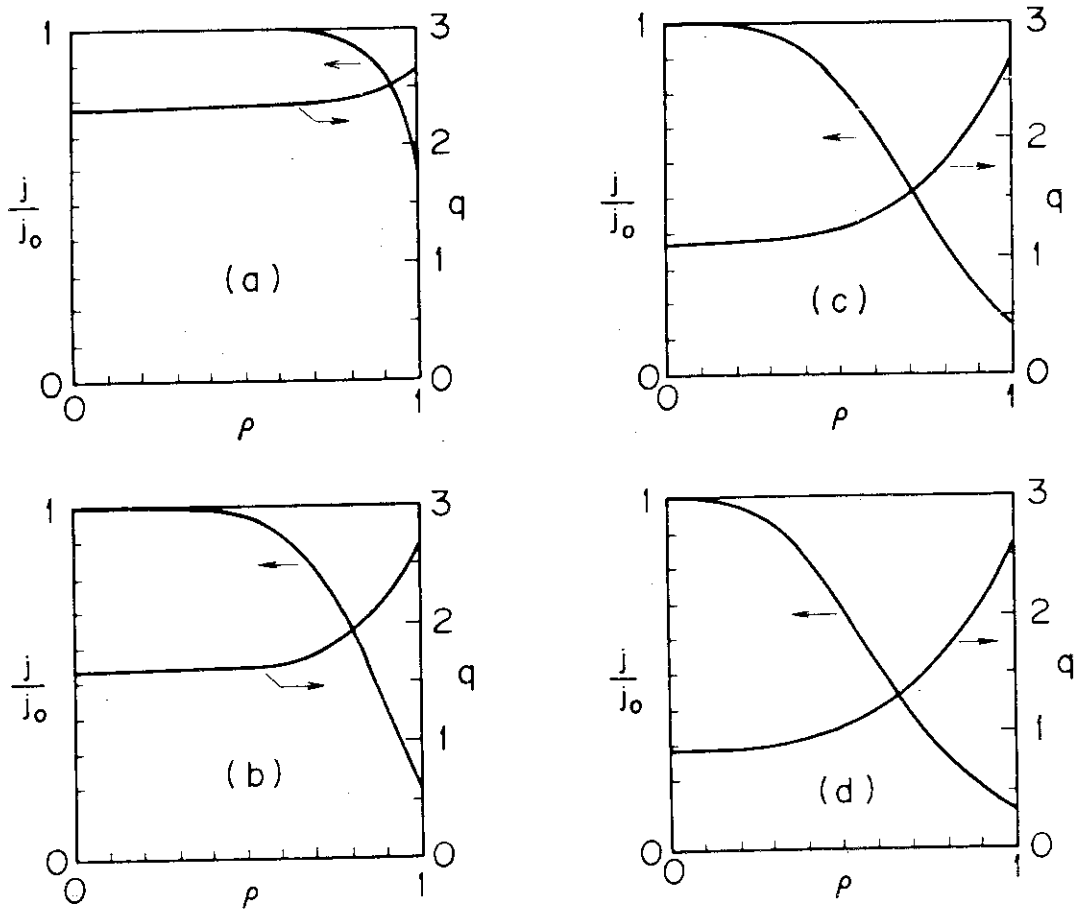


Fig. 6 Current density profiles at $\theta=\pi/2$ and q profiles.

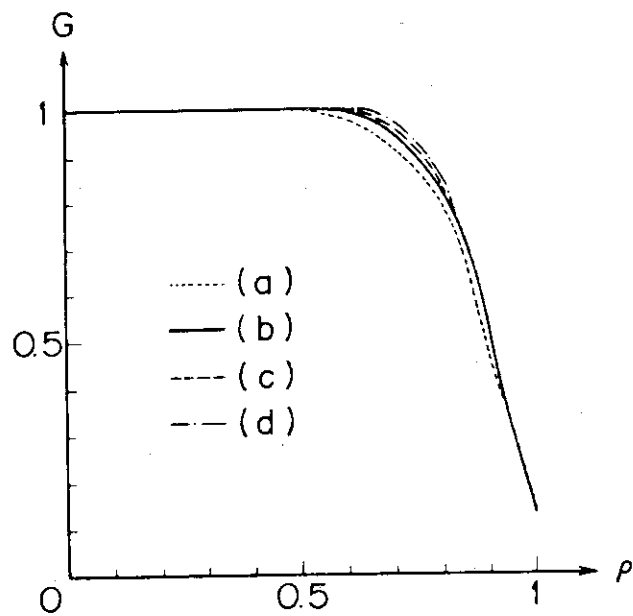


Fig. 7 Confinement ratio G vs ρ for various current density profiles as shown in Fig. 6.

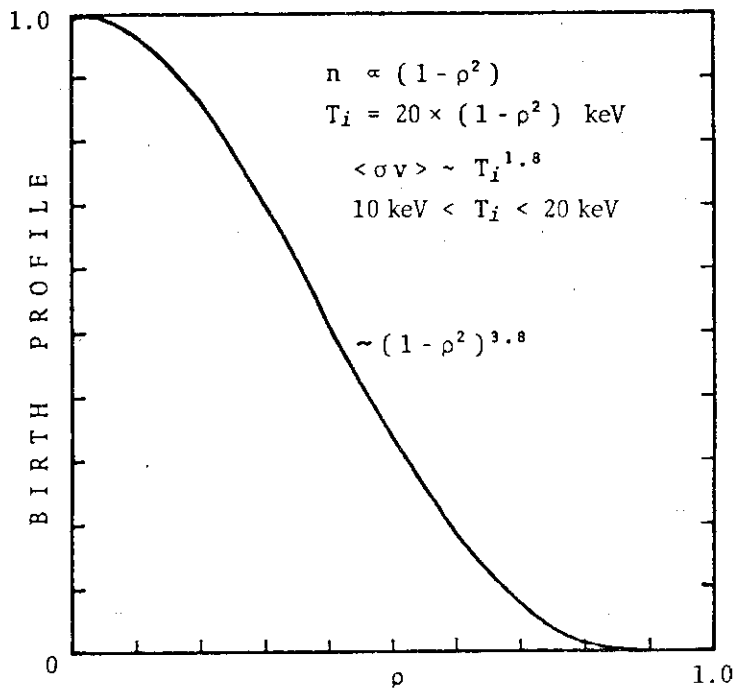


Fig. 8 The birth profile of 3.5 MeV alpha particles ($\propto n^2 \langle \sigma v \rangle$).

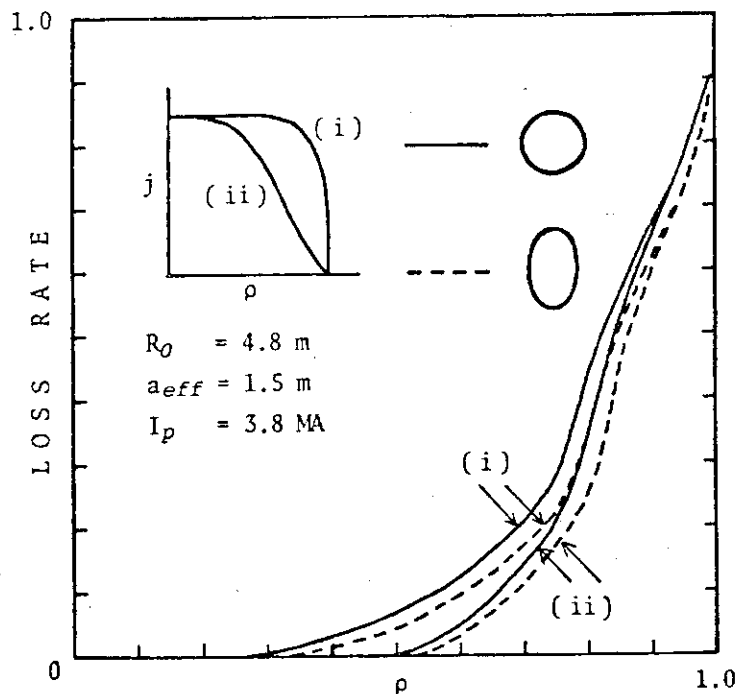


Fig. 9 Loss rates in a circular plasma and in an elliptic one. They are also calculated for cases of (i) flat current density profile and of (ii) peaked one.

7.2 Alpha Heating Profile During Slowing Down Process

It is shown that the alpha heating profile is almost the same as the birth profile.

(1) Analytical model and assumptions

- (i) Concentric circular cross-section for magnetic surface,
 - (ii) no radial electric field, (iii) flat current distribution.
- The magnetic field is, then, given by

$$B = \frac{\mu_0 jr}{2} \left(\frac{R_0}{R}\right) \vec{e}_\theta + B_{\phi 0} \left(\frac{R_0}{R}\right) \vec{e}_\phi \quad (1)$$

where μ_0 = permeability of free space, j = current density, R_0 = major radius, $B_{\phi 0}$ = toroidal magnetic field at the plasma axis. The radial profile of plasma density and temperature is assumed to be parabolic type as follows;

$$n(r), T(r) \propto 1 - \left(\frac{r}{a}\right)^2 \quad (2)$$

(2) Coulomb collisions

It is assumed that alpha particles slow down only through Coulomb interactions with the field plasma having a Maxwellian distribution. The rate of the mean deviation of the longitudinal velocity is given by¹⁾

$$\langle \Delta v_{\parallel} \rangle = - \sum_{j=e,i,I} q_{\alpha} \left(1 + \frac{m_{\alpha}}{m_j}\right) \frac{n_j \mu(v_j^2)}{m_{\alpha} v_{\alpha}^2} \quad (\text{m/s}^2) \quad (3)$$

The rates of change of the mean square deviations of the longitudinal and perpendicular velocities are given by

$$\langle (\Delta v_{\parallel})^2 \rangle = \sum_{j=e,i,I} \frac{K}{v_j} \frac{\mu(v_j^2)}{2v_j} \quad (\text{m}^2/\text{s}^3), \quad (4)$$

and

$$\langle (\Delta v_{\perp})^2 \rangle = \sum_{j=e,i,I} \frac{K}{v_j} \left(\mu(v_j^2) + \mu'(v_j^2) - \frac{\mu(v_j^2)}{2v_j} \right) \quad (\text{m}^2/\text{s}^3), \quad (5)$$

$$v_j = v_{\alpha}^2 / v_j^2,$$

$$q_{\alpha} = 1.015 \times 10^{21} e_{\alpha}^2 e_j^2 \ln \Lambda / m_{\alpha} \quad (\text{kgm}^6/\text{s}^4),$$

$$K = 2.030 \times 10^{21} n_j e_{\alpha}^2 e_j^2 \ln \Lambda / v_j m_{\alpha}^2 \quad (\text{m}^2/\text{s}^3).$$

where $\mu(x)$; error function, $\ln \Lambda$; Coulomb logarithm (the value is

assumed 20).

(3) Drift orbit and velocity

Three constants which characterize the motion of the alpha particles, i.e.

Magnetic moment;
$$\mu_{\alpha} = \frac{1}{2} m_{\alpha} v_{\perp}^2 / B \quad (6)$$

Canonical angular momentum;
$$P_{\phi} = e_{\alpha} R A_{\phi} + m_{\alpha} v_{\parallel} R \quad (7)$$

Kinetic energy;
$$E_{\alpha} = \frac{1}{2} m_{\alpha} (v_{\parallel}^2 + v_{\perp}^2) \quad (8)$$

are conserved within a period that is much shorter than the relaxation time due to Coulomb collisions. The equation of motion for the guiding center is derived from Eqs. (6)~(8) as follows²⁾.

$$e_{\alpha} \left(\frac{\mu_{\alpha} j R_0}{4} \right) r^2 + \epsilon m_{\alpha} v_{\parallel} R = P_{\phi} \quad , \quad \epsilon = \begin{cases} +1 & \frac{\vec{v} \cdot \vec{j}}{V \cdot J} < 0 \\ -1 & \frac{\vec{v} \cdot \vec{j}}{V \cdot J} > 0 \end{cases} \quad (9)$$

where P_{ϕ} ; an integration constant.

(4) Slowing down motions

Assuming the field particles have Maxwellian distributions, we can use the normal distribution for the changes in longitudinal and perpendicular velocities due to Coulomb collisions during the time Δt . Mean values and variances are given as follows;

$$m_{\parallel} = \langle \Delta v_{\parallel} \rangle \Delta t \quad , \quad m_{\perp} = 0 \quad ,$$

and

$$\sigma_{\parallel}^2 = \langle (\Delta v_{\parallel})^2 \rangle \Delta t \quad , \quad \sigma_{\perp}^2 = \langle (\Delta v_{\perp})^2 \rangle \Delta t \quad .$$

(5) Monte-Carlo calculation^{3),4)}

The changes in velocities due to Coulomb collisions are determined by sampling normal random numbers. The collision point on the orbit is determined by random numbers with a collision probability density $P_c \propto n/V_d$. By using these velocity changes and collision point, the orbit between successive collisions is obtained. The heating profile is calculated by integrating the energy deposition due to Coulomb collisions.

(6) Numerical results

Figure 1 shows the birth profile of alpha particles and the relative power density deposited by alpha particles until their energy decreases down to 350 keV. The alpha heating profile becomes slightly smaller and flatter than the birth profile because of the particle loss and the drift motion of alpha particles.

References

- 1) B. Trubnikov, Rev. Plasma Phys., ed. M.A. Lioyovich (Consultants Bureau, New York, 1965) Vol. 1, p.105.
- 2) D. McAlees, JRNL-TM-466.
- 3) M. Ohnishi, N. Ao, J. Wasabayashi, Nuclear Fusion 18 (1978) 859.
- 4) M. Azumi, private communication (1976).

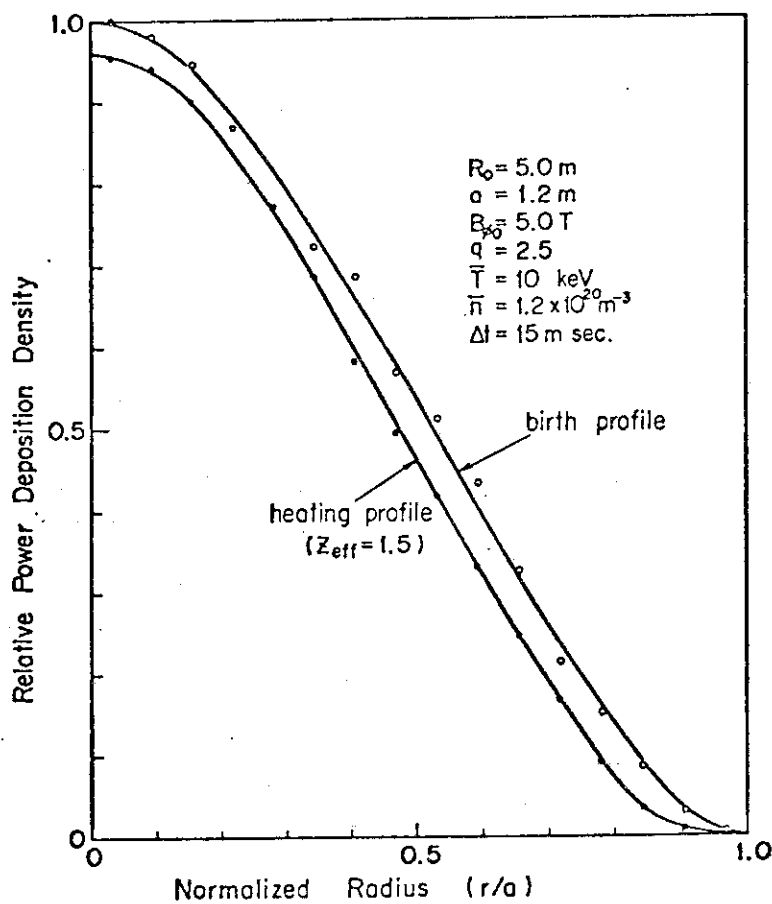


Fig. 1 Relative power density deposited by alpha particles using Monte-Carlo method. Birth particle numbers: 13000, loss of 3.5 MeV alpha particle: 12.1 %, total loss during slowing down to 350 keV: 18.1 %.

7.3 Loss of α -Particles by Ripple During Slowing DownModel

The computational model is the same as that described in Section 5-3). Parameters for the calculations are summarized in Table 1. The birth profile of α -particles is shown in Section 6-1) Fig. 1.

Results

The banana drift loss G_{r0} of α -particles is shown in Fig. 1 as a function of the amplitude of the toroidal ripple δ_0 . The ripple trapped loss is much less than 1 %. The banana drift loss in an axisymmetric field G_{s0} is also shown in Fig. 1. The difference $G_{r0} - G_{s0}$ implies that the enhanced banana drift is caused from the toroidal ripple.

The α -particle loss is less than 2.3 % when $\delta_0 < 2.5$ %.

Table 1 Plasma parameters

major radius	$R = 4.8$ (m)
minor radius	$a = 1.5$ (m)
toroidal field	$B_t = 5.0$ (T)
temperatures	$T_e(r) = T_i(r) = 2.0 \times 10^4 (1 - (r/a)^2)$ (eV) $(T_D(r) = T_T(r) = T_i(r))$
plasma density	$n_e(r) = 2.0 \times 10^{20} (1 - (r/a)^2)$ (m ⁻³) $(n_e(r) = n_T(r) = n_i(r))$
plasma current	$j_p(r) = j_0 (1 - (r/a)^2)$
safety factor	$q_a = 3.1$
effective Z	$Z_{eff} = 1.5$ (uniform)
charge number of impurity ion	$Z_{imp} = 8.0$ (oxygen)
toroidal field ripple	$\delta = \delta_0 \delta_1(r) \exp(-\beta \theta^2)$ $\delta_1(r) = (r/a)^2, \beta = 0.5,$
number of toroidal coils	$N_t = 12$

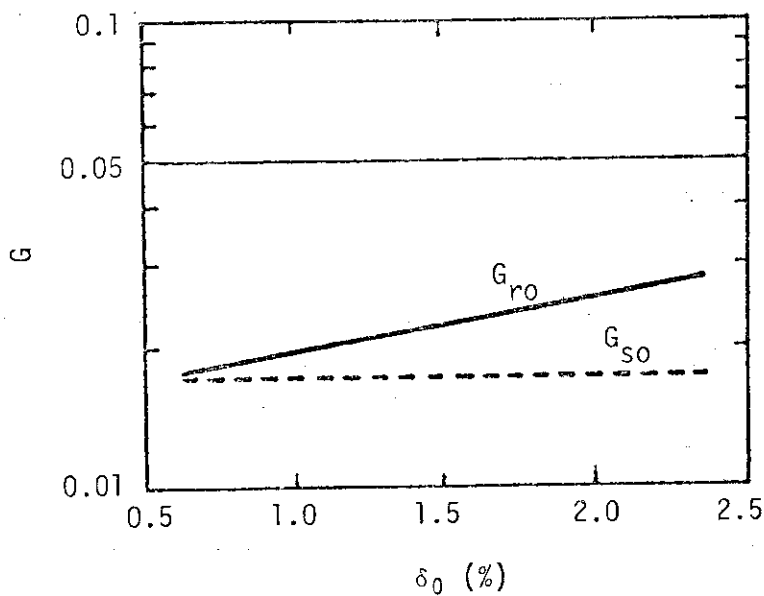


Fig. 1 Banana drift loss of α -particles as a function of the amplitude of the toroidal ripple.

8. Level of Synchrotron Radiation from INTOR Plasma

Wall reflectivity required for the INTOR parameters ($R=5$ m, $a=1.2$ m, $B_{t0}=5$ T, $T_e=T_i=10$ keV) is estimated on the basis of Rosenbluth-Trubnikov's theory. For reference we assume tentatively that the energy loss due to the synchrotron radiation should be less than 5 % of the α particle heating.

We find that no reflector is needed for the anticipated INTOR discharge of moderate β . For $\beta_e=0.01$, however, the reflection coefficient of the wall should be above 0.75. This assumes a Maxwellian velocity distribution of electrons, while most tokamak experiment indicates the presence of high energy tail in the electron distribution function, which enhances the synchrotron radiation loss. A rough estimate yields $r > 0.38$ for $\beta_e=0.02$ and $r > 0.96$ for $\beta_e=0.01$, r being the reflection coefficient, if we assume arbitrarily $n_{tail}/n=10^{-4}$, $T_{tail}/T_e=10$.

We may conclude there exists a fair margin in the INTOR except low density (low β) operations. If very high reflectivity becomes necessary, however, we have to pay close attention to the effective area, shape and conditions of the wall surface (presence of observation port, honeycomb structure, coating of low Z materials etc) as well as the accuracy of the radiation flux estimation.

It should be stressed also that the synchrotron radiation may deposit its energy at a place out of the direct sight from the plasma. In fact, in JT-60, the synchrotron radiation accounts for a significant portion of the heat deposit on cryopanel in the NBI beam line.

Error in the above estimate of the radiation flux may be about 50 %. More accurate evaluation requires detailed computation. A computer program for the absorption coefficient and emissivity of the radiation is just completed on the basis of Trubnikov's expression for the dielectric tensor with an approximation of $\omega=ck$.

Appendix

Some Consideration of INTOR Parameters

It is very difficult to fix the INTOR parameters at this time because each parameter is not independent from the others and compatibility has not been investigated in detail. In this appendix, we try to discuss some of the INTOR guiding parameters and to obtain a few reasonable sets of some important parameters.

a) b/a (see Figs. 1 and 2)

$$b/a = 1.6$$

Unstable with a reasonable breeding blanket.

$$b/a = 1.3 - 1.5$$

Stable with a distant shell. It is not necessary to change the fusion output, toroidal coils, NBI systems and so on.

b) Size

$$a \approx 1.2 \text{ m}$$

The radius seems small (Fig. 3).

A careful impurity control system, e.g. a divertor with a low- z wall, is required.

$$a > 1.2 \text{ m}$$

The impurity problems can be mitigated and a simple impurity control system, e.g. a cold plasma blanket without the divertor, can be applied.

RF heating as well as NBI heating are required.

c) Heating

NBI

NBI system requires a complex isotope separation system for refreshing the fuel gas (see Fig. 4).

NBI system can be applied only for a rather small line density plasma with $z_{\text{eff}} \approx 1$.

Profile control is difficult

The total heating efficiency is low.

RF

The isotope separation system is not required for refreshing the fuel.

No limitation for the line density of the plasma with $z_{\text{eff}} > 1$.

The profile control is easy (see Fig. 5).

The total heating efficiency is high (see Fig. 6).

d) Plasma control

Position

A distant shell with a slow feed back system with $b/a \approx 1.5$
and a close shell with a slow feed back system with $b/a = 1.6$.

Disruption

Profile control.

e) Impurity level

$z_{\text{eff}} \approx 1$ and 80 % heat flux to limiter

A careful impurity control system, e.g. the divertor with a low-z wall, is required.

Life time of the neutralizer plate is rather short or a long divertor throat with a large divertor chamber is required.

$z_{\text{eff}} > 1$

A simple impurity control system, e.g. a cold plasma blanket, can be applied.

The heat flux can be spread on the wide area of the first wall.

f) Impurity control and ash exhaust

The simple poloidal divertor

Reliable both for impurity control and ash exhaust.

Maintenance of the neutralizer plate is feasible but not easy.

It can be applied to a small machine with a low ripple field.

Bundle divertor

It requires a large divertor chamber, and small number of the toroidal coils or large toroidal coils.

Without divertor

A cold plasma boundary is required.

The system is simple but a rather large plasma is required.

The above discussion gives a few reasonable sets of parameters for INTOR and some of them are shown in the following table.

	Original small plasma		Improved small plasma	Improved large plasma
b/a	1.6		$\lesssim 1.5$	$\lesssim 1.5$
Heating	NBI		NBI+RF	NBI+RF
z_{eff}	~ 1		~ 1	$\gg 1$
Heat to limiter	$\sim 80\%$		$\sim 80\%$	$< 80\%$
Boundary plasma	hot		hot	cold
Wall erosion	serious		serious	mild
Impurity control	divertor		divertor	cold boundary
Position control	?	close shell + feed back	distant shell + feed back	distant shell + feed back
Disruption	?	$q_a < 2$ (close shell)	profile	profile
Section for tritium production	half	small	half	full
Isotope separation for refreshing fuel	necessary		unnecessary	unnecessary
Basic objectives	Demonstration of a reasonable fusion reaction with a high duty.			

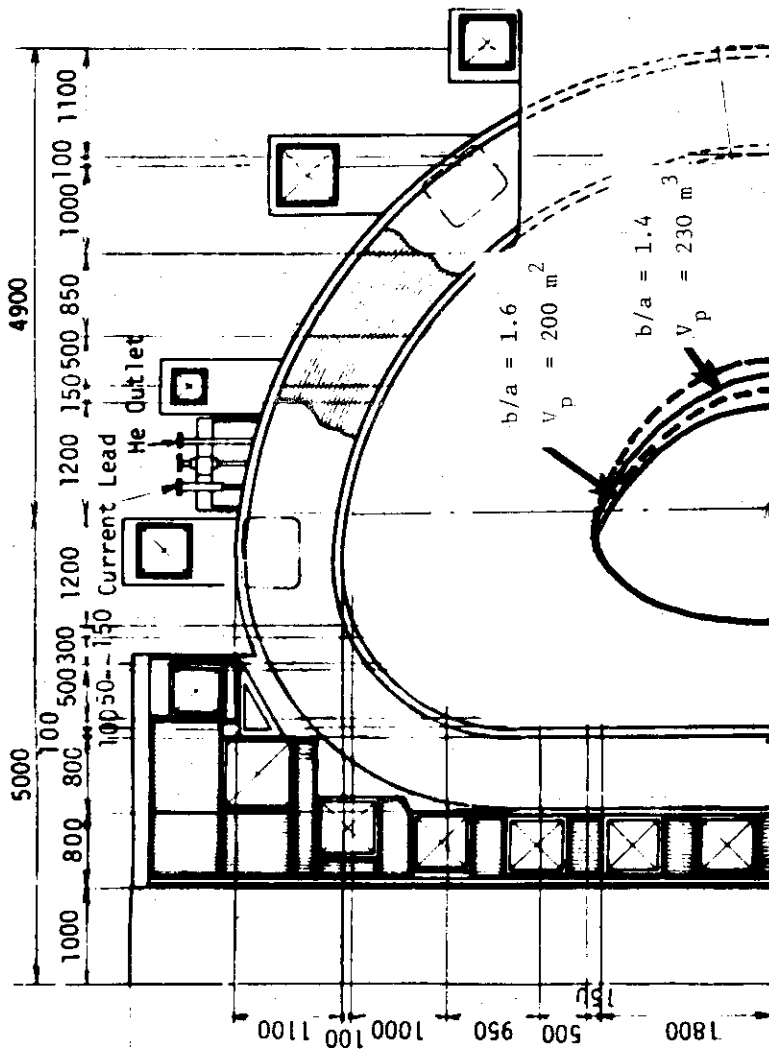


Fig. 2 Schematic cross-sectional view of plasma.

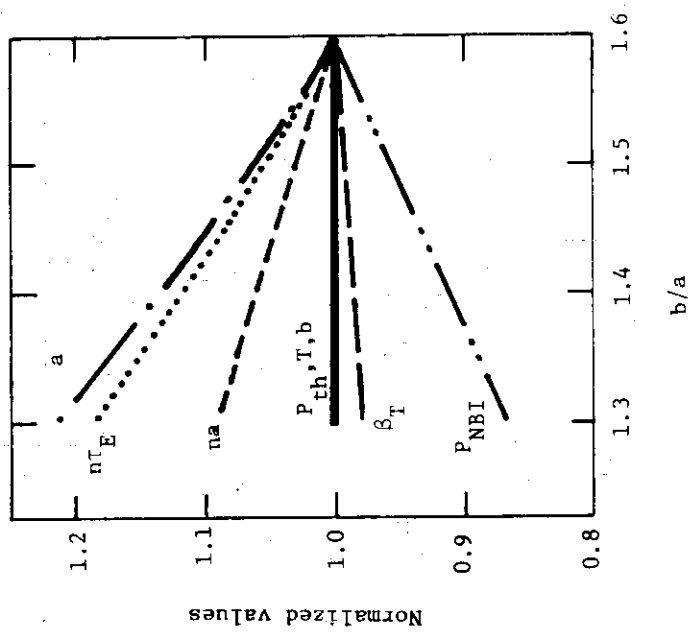


Fig. 1 Main parameters vs. b/a

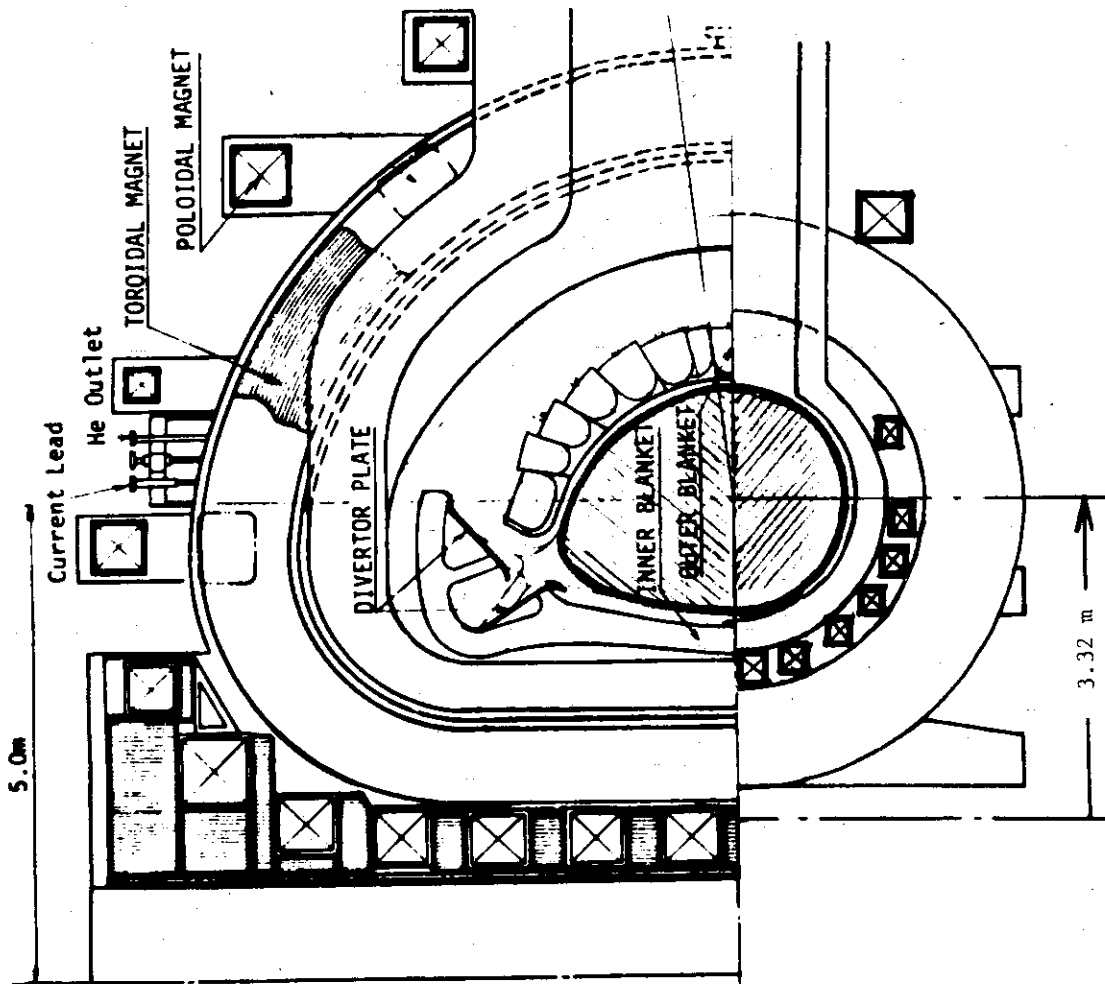


Fig. 3 INTOR-J and Possible variation of JT-60

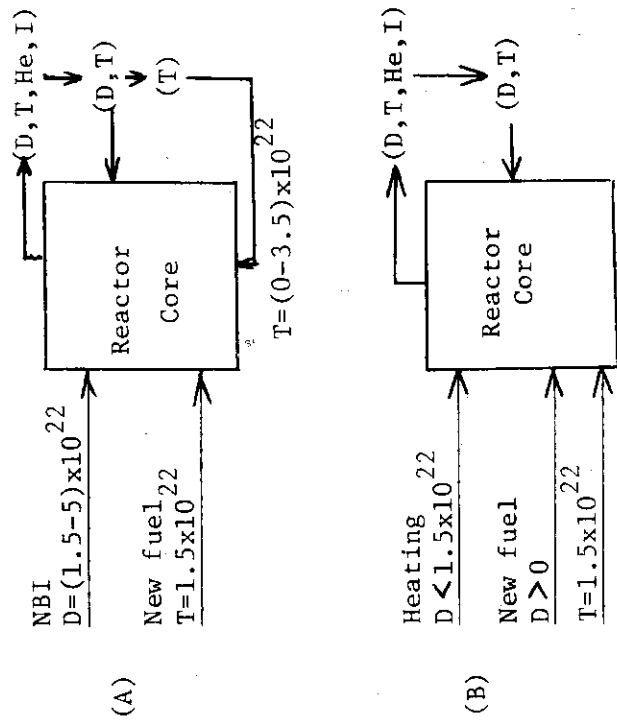


Fig. 4 Refueling and isotope separation

- (A) only NBI
- (B) NBI+RF

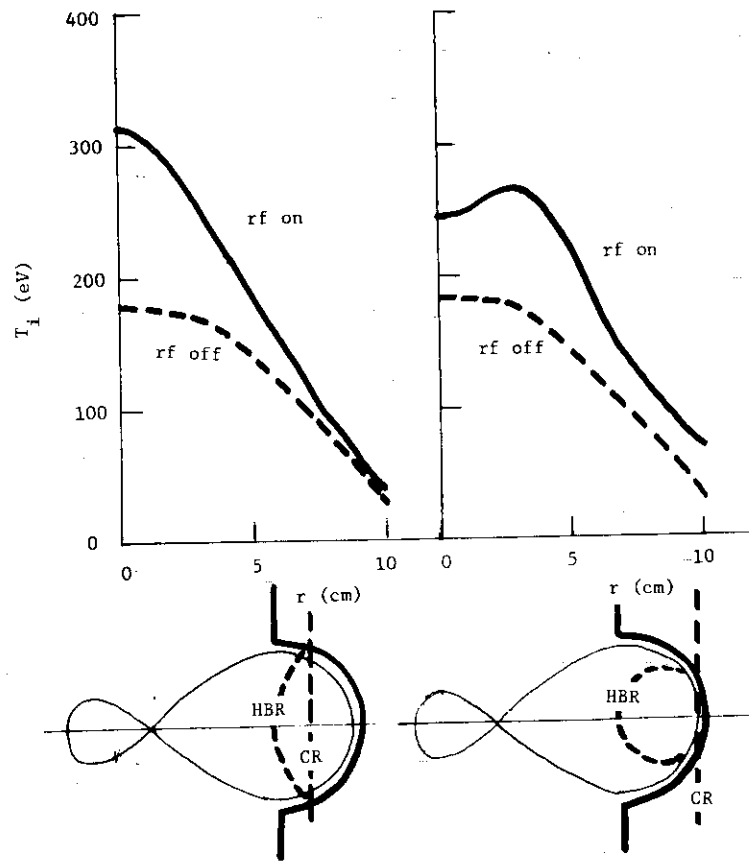


Fig. 5 Local heating by ICRF (in DIVA)
 HBR: hybrid resonance layer.
 CR : ion cyclotron resonance layer.

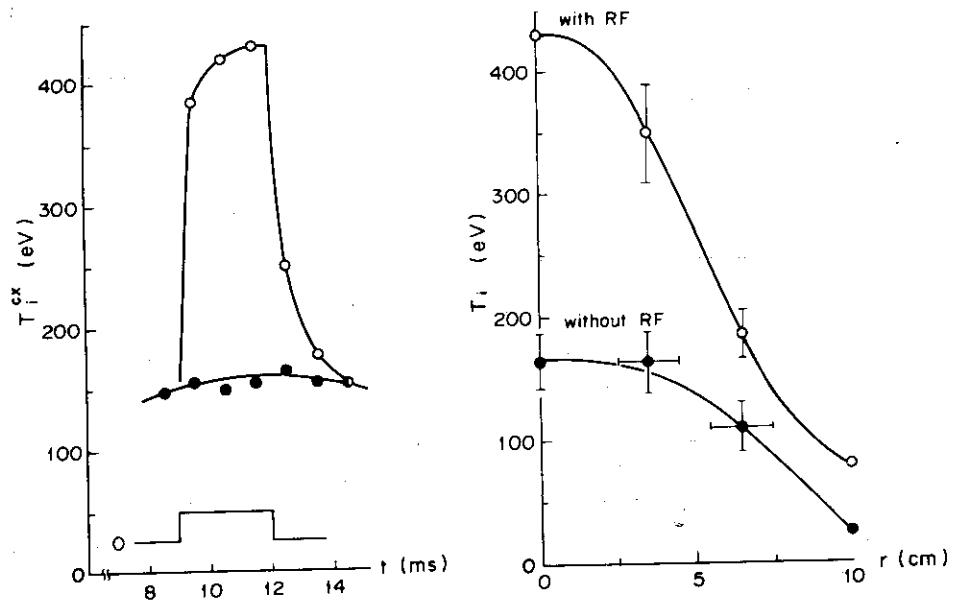


Fig. 6 High efficient ICRF heating (in DIVA).
 Heating efficiency is 70-100 % and the overall efficiency based on the primal electric power is 30-40 %.